Structural and Thermal Analysis of the ORCASat

João Pedro de Prata Neves Duarte

Thesis to obtain the Master of Science Degree in

Aerospace Engineering

Supervisor: Prof. Afzal Suleman

Examination Committee

Chairperson: Prof. Fernando José Parracho Lau
Supervisor: Prof. Afzal Suleman
Member of the Committee: Prof. Virgínia Isabel Monteiro Nabais Infante

January 2020

Dedicated to Ana Neves, Vitor Duarte, Mafalda Duarte and Maria Duarte.

Acknowledgments

Resumo

Análise estrutural e térmica do *Optical Reference Calibration Satellite* (ORCASat), um *CubeSat* de 2 unidades. O principal objetivo é demonstrar que o satélite cumpre os requisitos mecânicos e térmicos durante as fases de lançamento e órbita. A nível estrutural, é analisado se a frequência fundamental se mantém acima dos 90 Hz e se a estrutura principal suporta uma carga de 1200 N ao longo eixo longitudinal. O solver *Siemens NX Nastran* é utilizado para as análises de vibração e linear estática. Soluções são sugeridas sempre que os requisitos não são cumpridos. Os resultados numéricos são posteriormente comparados com resultados obtidos a partir de dois testes experimentais – um teste com mesa vibratória realizado na Universidade de Victoria e um teste de impacto realizado no *National Research Council*. Após um melhoramento relativo à densidade do Alumínio 6061, o modelo de elementos finitos que representa a estrutura externa é validado. A nível térmico, os ciclos de temperatura dos componentes são estudados para se verificar que o ORCASat, na órbita pré-definida, se encontra dentro do intervalo que permite a sua operabilidade. Nesta análise, o solver *Siemens NX Space Systems Thermal* é utilizado. As condições de fronteira são descritas e estabelecidas. De modo a acelerar as simulações, são sugeridas algumas simplificações. Dois casos opostos são analisados – caso quente e frio – sendo desenvolvido um sistema de controlo térmico passivo. É provado que o satélite mantém a sua integridade estrutural após o lançamento e sobrevive ao ambiente espacial, estando operacional durante o tempo esperado de vida.

Palavras-chave: CubeSat; Modelo de Elementos Finitos; Análise Estrutural; Frequência Fundamental; Análise Térmica; Sistema de Controlo Térmico

Abstract

Structural and thermal analysis of the Optical Reference Calibration Satellite (ORCASat), a 2U Cube-Sat. The goal is to demonstrate that the spacecraft fulfills the mechanical and thermal requirements during launch and orbital conditions. On the structural level, it is verified if the satellite's fundamental frequency remains above 90 Hz and if its main structure handles a load of 1200 N along the longitudinal axis. *Siemens NX Nastran* is used for both vibration and linear static analysis. Solutions are proposed when the requirements are not fulfilled. The numerical data is compared with the results obtained by two experimental tests - a shaker test performed at the University of Victoria and an impact test performed at the National Research Council. After an improvement involving the density of the material Aluminum 6061, the FEM model representing the spacecraft's external structure is validated. On the thermal level, the components' thermal cycles are studied to verify if the ORCASat operates between the safe temperature range in the defined orbit. The solver *Siemens NX Space Systems Thermal* is used in this analysis. Boundary conditions such as *Radiation Simulation Object*, *Heat Loads* and *Orbital Heating* are described and established. Simplifications in the solution details are suggested. Two opposite cases are analysed – hot and cold case – where a passive thermal control system is developed to maintain the ORCASat between its operational temperatures. It is proven that this satellite can maintain its structural integrity after launch and survive the space environment, being operational during its lifetime.

x

Contents

List of Tables

List of Figures

Nomenclature

Greek symbols

α Absorptivity

ε Emissivity

ζ Modal damp ratio

ν Poisson's Ratio

ρ Density

ρ' Reflectivity

σ Stefan-Boltzmann constant

τ Transmissivity

φ Phase angle

$\phi_{\mathbf{v}}$ Mode shape vector

χ Finite element dimensions

$\bar{\omega}$ Angular frequency

$\bar{\omega}_d$ Damped angular frequency

Ω Right ascension of the ascending node

Roman symbols

$\mathbf{0}$ Null vector

A Area

BA Earth's bond albedo

$\mathbf{C_p}$ Heat capacity matrix

$\mathbf{C}$ Damping Matrix

c_p Specific heat capacity

CTE Coefficient of thermal expansion

e   Unit vector

E Young's modulus

e Orbit's eccentricity

F   Force vector

f Frequency

F_i^j View factor from surface i to surface j

G Shear modulus

HL   Heat loads vector

h Thickness

I   Identity matrix

I Electrical current intensity

i Orbit's inclination

$\mathbf{K_t}$ Heat conduction matrix

$\mathbf{K}_e$ Stiffness matrix

k Thermal conductivity

L Distance between two entities

M   Mass matrix

m Mass

$\dot{q}$ Heat flux

$\dot{\mathbf{q}}$ Heat flux vector

R   Radiation exchange matrix

r Distance between the satellite and Earth's center

$R_{contact}$ Thermal contact resistance between two surfaces

$\dot{\mathbf{T}}$ Temperature change with time vector

T   Temperature vector

T Temperature

t Time

U Electrical potential difference

$\ddot{\mathbf{x}}$ Acceleration vector

$\dot{\mathbf{x}}$ Velocity vector

$\mathbf{x}$ Displacement vector

Subscripts

i, j Computational indexes or Iteration number

x, y, z Cartesian components

Superscripts

T Transpose

Glossary

1D One Dimensional

2D Two Dimensional

3D Three Dimensional

ABS Acrylonitrile Butadiene Styrene

ADCS Attitude Determination and Control System

ALTAIR Airborne Laser for Telescopic Atmospheric Interference Reduction

CAD Computer Aided Design

CCP Canadian CubeSat Project

CDR Critical Design Review

CfAR Centre for Aerospace Research

CHIME Canadian Hydrogen Intensity Mapping Experiment

COTS Commercial-Off-The-Shelf

CSA Canadian Space Agency

CSDC Canadian Satellite Design Challenge

CVCM Collected Volatile Condensable Material

ECOSat Enhanced Communications Satellite

EGSE Electrical Ground Support Equipment

EMA Experimental Modal Analysis

EPS Electrical Power System

ESO European Southern Observatory

FEA Finite Element Analysis

FEM Finite Element Method

FFT Fast Fourier Transform

FR Flame Retardant

FRF Frequency Response Function

GMT Greenwich Mean Time

GPS Global Positioning System

ISS International Space Station

LED Light Emitting Diodes

LEO Low-Earth-Orbit

LSST Large Syn-optic Survey Telescope

MAC Modal Assurance Criterion

NASA National Aeronautics and Space Administration

NRC National Research Council Canada

NRCSD NanoRacks CubeSat Deployer

OBC On-Board Computer

ORCASat Optical Reference Calibration Satellite

Pan-STARRS Panoramic Survey Telescope and Rapid Response System

PCB Printed Circuit Board

PDR Preliminary Design Review

P-POD Poly-Picosatellite Orbital Deployer

RBF Remove Before Flight

SFU Simon Fraser University

SSL Space Systems Loral

TCS Thermal Control System

TML Total Mass Loss

TT&C Tracking, Telemetry and Command

UBC University of British Columbia

UHF Ultra High Frequency

USA United States of America

USSR Union of Soviet Socialist Republics

UVic University of Victoria

Chapter 1

Introduction

1.1 Context

Satellites surround us and have an active role in our quotidian. The benefits of developing the space sector are not only for advancements in science. The technology also improves the quality of life [1]. Satellites serve different purposes like military or civilian and their number have been increasing exponentially.

To better understand the universe, more accurate instruments are needed. Orbital measurements done by satellites cover wider areas and show more precise results than the data obtained by ground-stations on Earth or even airborne observations because the atmosphere interference is lower or null.

1.1.1 CubeSats

Satellites can be as big as a truck or as small as a loaf of bread that is why they are divided in different categories depending on their mass. This thesis focuses on small satellites so, the characteristics of other satellites will not be shown. Small satellites are divided in three different groups from the lightest to the heaviest: picosatellites (0.1 to 1 kg), nanosatellites (1 to 10 kg) and microsatellites (10 to 100 kg) [2]. Lighter satellites are more affordable to be sent to space making it easier to obtain scientific answers. This happens because they can be launched as secondary payloads attached to primary and heavier payloads. Even if these satellites are the primary payload they can be put into orbit using smaller and cheaper launch vehicles due to their lower mass [1].

The first nanosatellite being launched was the *Vanguard 1* with a mass of 1.47 kg on March 1958 by the United States of America (USA) while the Union of Soviet Socialist Republics (USSR) was launching larger, heavier and more complex satellites (for example, *Sputnik 1* was launched on October 1957 and had a mass of 83.6 kg) since the mentality was *bigger is better* [3]. This idea was drastically changed over the years and, by analyzing figure 1.1, it is verified that the interest on sending smaller satellites to orbit has been increasing.

In 1999, the first called CubeSat was developed by the Stanford University's Space Systems Development Laboratory with the collaboration of the California Polytechnic State University [5]. Its purpose
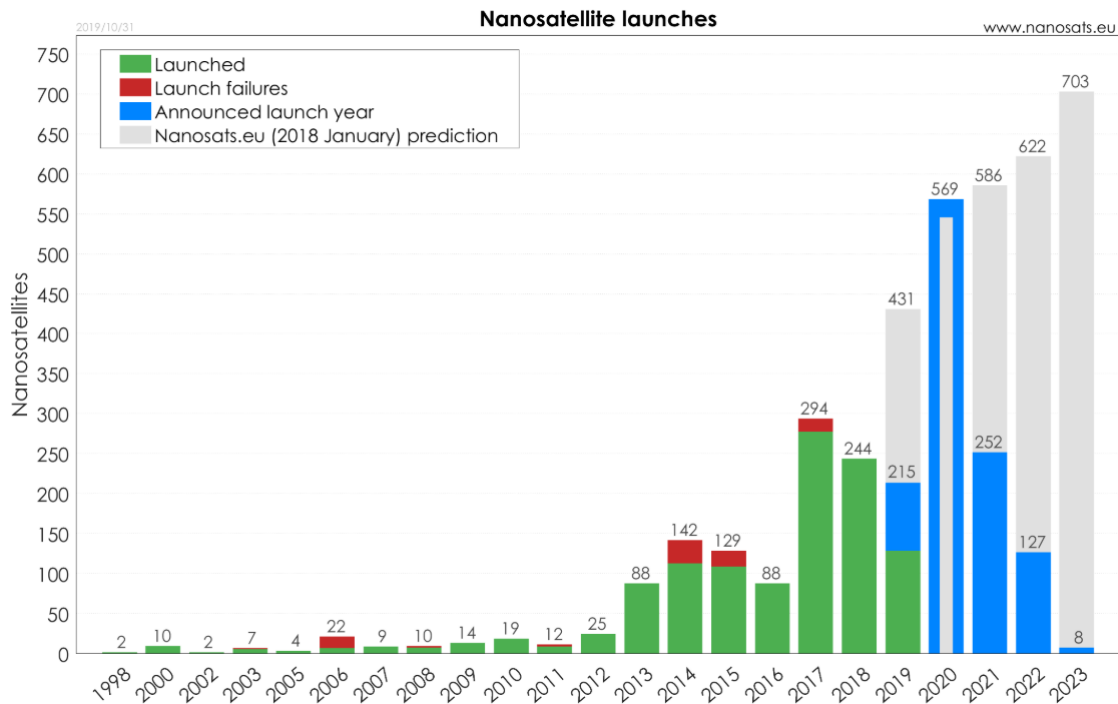
Figure 1.1: Number of nanosatellites launched over the years [4]

was to provide a standard design for nanosatellites in order to reduce costs, decrease time for development and, this way, increase the accessibility to space [6]. CubeSats are measured in units, U's, which consists of a cubic volume with a 10 cm side and a mass up to 1.33 kg. These cubic shapes can be combined and form a 2, 3, 6 or 12 U satellites, respecting the mass constraint (Fig. 1.2).
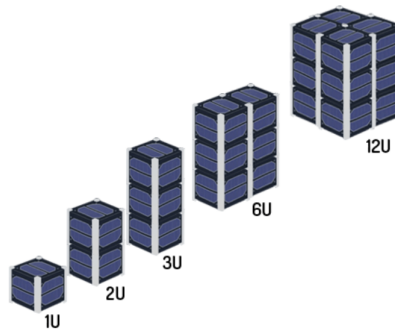
Figure 1.2: Cubesat configurations [7]

Besides developing a standard satellite, these universities showed a standard deployment system called Poly-Picosatellite Orbital Deployer (P-POD). Nowadays there are other deployers with different designs available to accommodate CubeSats that differ in the maximum satellite dimensions available to accommodate the spacecraft but their mechanisms are similar [1]. Being the interface between the satellite and the launch vehicle, they are designed to be versatile and as light as possible. It is guaranteed that, in the event of a CubeSat failure, the remaining payloads and launch vehicle stay intact and protected against any interference (mechanical, electrical or electromagnetic). During deployment, the CubeSats are also released with minimum spin and low probability of collision with the launch vehicle or other spacecrafts [8]. The ORCASat will be deployed by the NanoRacks CubeSat Deployer (NRCSD)
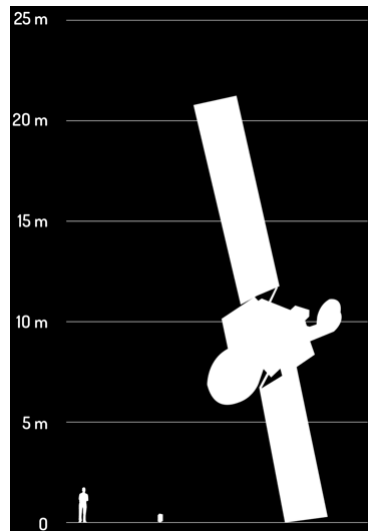
Figure 1.3: Scale between the CubeSat *LUME 1* and the satellite *HISPASAT 36 W-1* [7]

from NanoRacks.

CubeSats started as training projects where university students could test and train their skills in different engineering fields by solving real-life problems. With the development of new technologies and the possibility of fitting more complex instruments in less space, CubeSats started gaining importance since great science advances could be made with cheaper satellites [9]. Another aspect that makes these satellites so affordable is the ability of developing components off the shelf to fit into the structural requirements of the CubeSats designated by Commercial-Off-The-Shelf (COTS) [3].

Even with these advantages, CubeSats have several restrictions in terms of power, volume and mass that still limit more complex missions. Such limitations must be addressed throughout the entire project, for example, the orbit selection should concern several studies like the power generation and thermal impact [10]. Other technical challenges, hard to be controlled, can appear related to micrometeoroids, dust and radiation. CubeSats are usually protected by a thin shield made of aluminum and fiberglass epoxy and all the components are close to each other and to the surrounded environment which make them vulnerable to damage by dust and micrometeoroids. On the other hand, typical satellites offer more room to the electronics being distant from the protective shield. [11].

1.1.2 ORCASat

ORCASat stands for Optical Reference Calibration Satellite. Being developed with the collaboration of the Canadian Space Agency (CSA) and by representing the British Columbia province, this 2U CubeSat is part of a contest named Canadian CubeSat Project (CCP), which the main purpose is to increase student's interest in science, technology, engineering and mathematics, particularly in space domains by providing the opportunity to design, build, test and operate a CubeSat. With this *hands-on experience*, it is possible to get a new generation of highly qualified personnel to take care of Canada Space Exploration in the upcoming years. The satellite is being developed through a combined effort of

three western Canadian universities – University of Victoria (UVic), Simon Fraser University (SFU) and University of British Columbia (UBC). It also counts with support from other academic institutions and industry collaborators such as University of Lisbon, National Research Council Canada (NRC), Harvard University and Space Systems Loral (SSL) [12]. ORCASat should be launched from the International Space Station (ISS) in the final quarter of 2021.

The mission's problem-solution can be described as below [13]:

– **Problem:** Scientists want to know the expansion rate of the universe and how is changing over time. Distant supernovae can be used to identify this rate however, one must measure the brightness of the supernovae with extreme precision. When looking at a supernova through a telescope, the light is lost in the atmosphere making it appear less bright. Scientists can only measure how bright a supernova appears, rather than how bright the supernova actually is. There is not a precise-enough way to determine how much light from the supernova is lost along the way;

– **Solution:** In order to calibrate ground-based telescopes, one of the main techniques is photometric calibration using standard stars in the sky [14]. ORCASat is an artificial star with a precisely-known brightness and is above the atmosphere. Scientists can use a telescope to observe ORCASat and measure how bright it appears. The difference between how bright ORCASat is and how bright ORCASat appears, is the amount of light lost in the atmosphere and in the telescope optics. It is possible to incorporate that lost light back into the measurements and calibrate the telescopes to measure how bright the supernovae exactly are. Once ORCASat is launched, supernovae can be used to precisely measure the expansion rate of the universe. As the ORCASat is equipped with Light Emitting Diodes (LED's) and laser lights, which are monochromatic, individual wavelengths can be calibrated making it possible to have an entire calibrated spectrum [15].

The ORCASat can be separated into its primary and optional mission objectives [13].

– **Primary Mission:** on the scientific level, the spacecraft shall provide a reference light source in Low Earth Orbit (LEO) to test a novel methodology for calibrating ground-based optical telescopes. On the educational level, the ORCASat project shall provide a platform for training opportunities to develop marketable new skills in space science and technologies.

– **Optional Mission:** on the scientific level, supply the Canadian Hydrogen Intensity Mapping Experiment (CHIME) observatory with valuable data by calibrating its observation antenna and characterizing the CHIME antenna via a consistent radio source on board the satellite [10]. On the educational level, ORCASat shall provide a store and forward amateur radio repeater.

1.2 Objectives

With two years prior to launch this work was developed while the preparation for the Preliminary Design Review (PDR) presentation. The main purpose of this thesis is to characterize the behaviour of the ORCASat satellite structurally and thermally. Finite element analysis were performed in order to know

this behaviour and solutions were adopted every time it was verified that its integrity and components were not working on the safe range. This was possible using the CAD model developed by the *Mech & Thermals* team.

In the structural analysis three FEM models are developed from the simplest to the most complex and modal simulations are performed to check the fundamental frequency of the satellite and the respective mode shapes (Fig.1.4). In order to validate the finite element models used, these results are then compared with three different experimental tests - two experimental tests done to the simplest model and one to the most complex. If at any time the results do not meet the requirements adopted, a solution should be proposed. If the error between the experimental and numerical results is high, it is concluded that the numerical model needs to be optimized so that the team can rely more on numerical analysis (where faster results are obtained) and less on experimental results (whose preparation requires more time).

In the thermal analysis the most complex FEM model is studied and the satellite is simulated in an orbit with the same characteristics as the real one. Temperature peaks are the most important data for the development of this work and if any component reaches temperatures outside its safe range, solutions should be proposed as well.

Being the team in the PDR phase, this is an advantage but also a disadvantage for the analysis performed. The good side is that the CAD model is almost complete which approximates the numerical results with reality and if small modifications on the satellite design are needed, these can be done if the other subsystems are not affected since the development of the ORCASat is half away to be completed. The bad side is that if this modification affects other subsystems considerably, this cannot be performed due to the lack of time available until the Critical Design Review (CDR). Another downside is that the CAD model is constantly being updated especially when it comes to the satellite's structure so, by the end of this work, it is possible that some features will not be present. Having this said, the data and results obtained during this thesis should not be considered as final results but should help the team to know if the mission is going towards success. Also, this project is a way of learning and improving the skills related to finite element analysis using the program *Siemens NX*. The procedure should be seen as a guide for future analysis since there is a lack of documentation and tutorials available.

1.3 Thesis Outline

This thesis is organized as follows:

Chapter 2 presents the theoretical background that supports the modal and thermal analysis of this project.

Chapter 3 provides an overview of the ORCASat where both payloads are described as well as its requirements. The satellite's design and subsystems are characterized.

Chapter 4 explains the process for the dynamic and static analysis. The idealization and finite element models are described as well as the adaptations and solutions adopted. The experimental modal analysis and its results are compared to the numerical ones and the conclusions presented.

Chapter 5 explains the process for the thermal analysis. The finite element model and the simulations performed are described. The obtained temperature distributions are discussed and the applied thermal control systems explained.

Chapter 6 presents the main conclusions and achievements throughout the development of this project. It also presents some recommendations for future work.
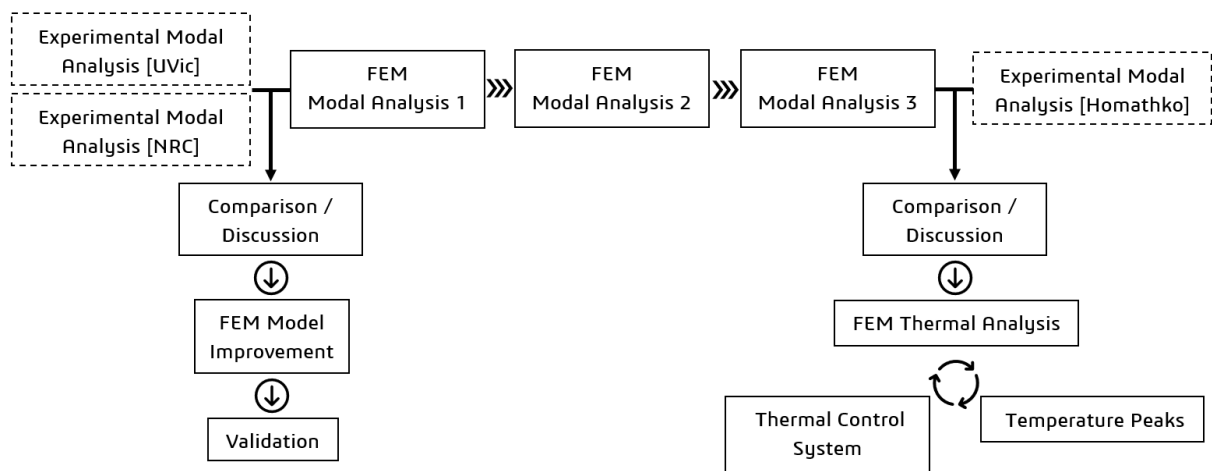
Figure 1.4: Thesis flowchart

Chapter 2

Theoretical Background

2.1 Dynamic Analysis

During launch and deployment, CubeSats are submitted to aggressive environments in terms of vibration and loads that can damage their structure. This makes a modal analysis extremely important during the development of a satellite since, if it is performed properly, it establishes the line between failure or success [10]. With a modal analysis it is possible to check if the structure needs some design modifications because the minimum frequency requirement is not satisfied or because failure occurs due to fatigue caused by excessive vibration, consequence of the structure's resonance [16].

2.1.1 Numerical Modal Analysis

The main purpose of a numerical modal analysis is to determine the modal frequencies and respective mode shapes of a system during a free (no loads) or free-free (no loads and constraints) vibration allowing to evaluate the linear dynamic characteristics of a system [16].

A natural mode of vibration is characterized by an harmonic motion of every point of the structure around a point of equilibrium which is passed by at the same instant for all the points. The frequency of this harmonic motion is called natural frequency [16].

The fundamental frequency is the first natural frequency and the most relevant for this thesis. Its value is influenced by a great number of factors being the most important related to the physical properties of the system and its boundary conditions, observed during the analysis developed where different criteria was considered to verify the changes on the satellite's behaviour. Other parameters are the magnitude and distribution of masses and inertia.

A multidegree-of-freedom system can have its equations of motion represented in a matrix form that depends on the mass matrix $\mathbf{M}$, the damping matrix $\mathbf{C}$, the stiffness matrix $\mathbf{K}_e$ and the force vector $\mathbf{F}$, being $\mathbf{x}$, $\dot{\mathbf{x}}$ and $\ddot{\mathbf{x}}$ the displacement, velocity and acceleration, respectively [17].

$$\mathbf{M}\ddot{\mathbf{x}} + \mathbf{C}\dot{\mathbf{x}} + \mathbf{K}_e\mathbf{x} = \mathbf{F} \tag{2.1}$$

7

To determine the natural modes of vibration the force is zero, as the system is subjected to a free vibration case, and the damping coefficient is not considered, as natural frequencies correspond to the undamped case. The equation is simplified corresponding to the undamped free vibration of the system.

$$\mathbf{M}\ddot{\mathbf{x}} + \mathbf{K_e}\mathbf{x} = 0 \tag{2.2}$$

Assuming that,

$$\mathbf{x} = \phi_{\mathbf{v}}sin(\bar{\omega}t + \varphi) \tag{2.3}$$

which corresponds to an harmonic solution. $\phi_{\mathbf{v}}$ is the mode shape vector, $\bar{\omega}$ is the angular frequency and φ is the phase angle. Replacing in the Eq.2.2, the following is obtained,

$$(\mathbf{K}_e - \bar{\omega}^2\mathbf{M})\phi_{\mathbf{v}} = 0 \tag{2.4}$$

where $\bar{\omega}^2$ defines the eigenvalues and $\phi_{\mathbf{v}}$ defines the eigenvectors allowing to obtain the natural frequencies and natural mode shapes, respectively. A non-trivial solution of the mode shapes is obtained,

$$\det(\mathbf{K}_e - \bar{\omega}^2\mathbf{M})\phi_{\mathbf{v}} = 0 \tag{2.5}$$

By expanding Eq.2.5, the characteristic equation can be obtained and, by solving it for $\bar{\omega}$, the natural frequencies, in Hz, can be calculated from,

$$f_i = \frac{\bar{\omega}_i}{2\pi} \tag{2.6}$$

All the other components of the mode shape can be computed by choosing an arbitrary value for one of the components of the corresponding mode shape. The mode shape is intended to give information about the shape of vibration in each natural frequency, not its amplitude, that is why it is possible to do it [17].

Usually, the modes of shape are normalized in relation to the mass matrix by using the following equation,

$$\phi_{v_{i_n}}^T \mathbf{M}\phi_{v_{i_n}} = \mathbf{I} \tag{2.7}$$

The number of degrees of freedom of the system defines the number of natural frequencies and corresponding mode shapes. When a linear elastic structure is in free or forced vibration, its vibration shape can be given by a linear combination of all its natural mode shapes [17].

When the mass and stiffness matrices are symmetric and real, the mode shapes are orthogonal which means that each mode shape is unique and cannot be obtained by linear combination of the other modes. This property can be represented in the following way,

$$\phi_{v_i}^T \mathbf{M}\phi_{v_j} = 0 , \quad i \neq j \tag{2.8a}$$

$$\phi_{v_j}^T \mathbf{K}_e\phi_{v_i} = 0 , \quad i \neq j \tag{2.8b}$$

8

The natural frequencies are higher when the system has less mass or higher stiffness or can be lower when the system has higher mass and less stiffness. The equation that demonstrates this behavior is the Rayleigh's equation and can be obtained by doing the ratio between the stiffness and mass.

$$\bar{\omega}_i^2 = \frac{\phi_{v_i}^T \mathbf{K}_e \phi_{v_i}}{\phi_{v_i}^T \mathbf{M} \phi_{v_i}} \tag{2.9}$$

In cases where the system presents damping, each frequency of damped vibration can be calculated by considering the following solution in each equation represented by Eq.(2.1) [1],

$$x_i = C_i e^{s_i t} \tag{2.10}$$

where C_i represents the amplitude of x_i and s_i represents a complex number.

By substituting the previous solution in each equation of the system, which represents each degree of freedom, the frequency of damped vibration, given by $\bar{\omega}_d$, can be obtained from,

$$\bar{\omega}_{d_i} = \bar{\omega}_i \sqrt{1 - \zeta_i^2} \tag{2.11}$$

where ζ defines the modal damping ratio and can be obtained by the quotient between the damping term c_i and twice the product of the mass term m_i with the natural frequencies,

$$\zeta_i = \frac{c_i}{2 m_i \bar{\omega}_i} \tag{2.12}$$

By looking at Eq.(2.11) an oscillatory motion only results if $\zeta < 1$, which corresponds to the underdamped case. In this case, the frequency of the damped vibration is always lower than the natural frequency [1].

The *NX Nastran* user's guide reports that the software has several numerical methods to calculate the fundamental frequencies and mode shapes since none of the existed methods are perfect for solving every structural problems although they can be used for the majority of the problems. Usually the method is chosen based on its efficiency [18].

The methods for eigenvalue extraction can be classified as transformation and tracking methods - in the first one, the eigenequation is transformed in a form from which the eigenvalues can be easily extracted; in the second one, the eigenvalues are extracted by an iterative procedure. The best method combines the advantages of both tracking and transformation.

NX Nastran allows the user to choose between *Lanczos* or *Householder* methods. The *Householder* method is a transformation method and is better applied to small matrices, having a low cost in computing modes but higher cost if the matrices are large. The *Lanczos* method is a combination of the advantages of transformation and tracking methods and is better applied to medium and large matrices but maintains a medium cost in computing modes in both small and large matrices [18]. That way, the latter method has a performance advantage and it was chosen to perform this numerical study.

2.1.2 Experimental Modal Analysis (EMA)

One of the purposes of doing a numerical analysis using a finite element method is being able to compare the data and validate the model with the results obtained by experimental tests. Shaker and impact testing can be performed to obtain this information [19]. These tests were done in this thesis and information related to the setup, problems faced while performing them and the type of data obtained can be found on chapter 4.

– **Shaker test:** It consists of placing and attaching the structure on a shaker table that will input a force in a certain frequency range. According to [20], shakers are usually provided with load cells to control the input force and sensors, as accelerometers, are placed in specific points on the structure to measure the output values (as displacement, velocity or acceleration) in the desired directions. This test is more adequate for structures with larger dimensions or higher masses where low frequencies need to be measure. When the structure needs to be excited at low frequencies, the period should be long enough to detect these values;

– **Impact test:** Is the most popular method to determine natural frequencies and mode shapes. An hammer is used as an input force and there is a cell load attached to its head that measures the applied force while sensors measure the output on a desired direction. The input frequency range is controlled by the hardness of the hammer's head i.e. the harder its tip, the wider the frequency range [10]. It is advised to choose different impact locations to reduce the possibility of not exciting a particular mode of vibration. At the same time, this location must also consider the local flexibility of the structure and the possibility of double impact [1]. One disadvantage of this method is that the structure may not be able to be excited uniformly by the hammer.

While performing the mentioned tests, the data is obtained as Frequency Response Functions (FRFs) which is a ratio of the structure's behavior (output) due to the applied force (input), transformed from the time domain to the frequency domain using Fast Fourier Transform (FFT) algorithms. The resonance frequencies are identified as the peaks of the amplitude diagrams.

2.2 Thermal Analysis

Thermal analysis are of extreme importance as they allow for a better understanding of the system's behaviour when it is submitted to different environmental conditions. This analysis simulates the space environment and, by defining the various parameters of the satellite's orbit, it is possible to know the variations of temperature that occur on the spacecraft as well as if its components stay between their operational range. This information helps developing a thermal control system which purpose is to protect the satellite's internal components from the extreme conditions of space [10].

Thermal analysis can be performed with stationary or transient conditions. For satellites, the boundary conditions are time varying and even the heat transfer processes change while the spacecraft is in orbit so, in order to obtain results that can simulate the reality i.e. to correctly predict the systems's

response, the transient analysis was chosen. The different types of heat sources can be found below.

2.2.1 Heat Sources

Radiation

Radiation does not require matter to propagate. It results from the loss of internal energy in order to achieve thermal equilibrium with the surrounding environment [10]. Every surface/body irradiates so, in the case of a satellite, the main sources are the radiation from the Sun, Earth and all the surfaces/subsystems of the spacecraft; and the Earth's albedo.

Solar radiation According to [21], a black body is an idealized physical body that absorbs all incident electromagnetic radiation, regardless its frequency or angle of incidence. By considering the Sun as a black body and by using the Stefan-Boltzmann Law, it is possible to estimate the total emissive power of this star and calculate the solar flux,

$$\dot{q}_{solar} = \sigma T_s^4 \tag{2.13}$$

where σ is the Stefan-Boltzmann constant ($\sigma = 5.6697 \times 10^{-8} Wm^{-2}K^{-4}$) and T_s represents the Sun's effective temperature i.e. is the temperature of a black body that would allow to emit the same total amount of electromagnetic radiation [21].

Considering the star as a perfect sphere ($r_s = 6.957 \times 10^8 \ m$) and multiplying the spherical surface area by the heat flux, the total heat transfer rate emitted by the Sun is obtained,

$$\dot{Q}_{solar} = \dot{q}_{solar} \times 4\pi r_s^2 \tag{2.14}$$

The solar flux that reaches the satellite changes over the year being its highest on the December Solistice and the lowest on the June Solistice. This happens because the heat is spread over a wider area as the distance to the Sun increases. Using Eq.(2.15) and dividing the heat rate emitted by the Sun by a surface area of a sphere which the radius is now the distance from the Sun to Earth (represented by r_θ), the heat flux that reaches the Earth can be estimated as well as the maximum and minimum values.

$$\dot{q}_{solar_{Earth}} = \frac{\dot{Q}_{solar}}{4\pi r_\theta^2} \tag{2.15}$$

The variation of the solar flux for one year in LEO is represented (Fig. 2.1). The point where the Earth is closest to the Sun is designated Perihelion and the point where the Earth is farthest is designated Aphelion (Fig. 2.2).

The materials used on the satellite components play an important rule on the amount of power that is absorbed, transmitted and reflected by the spacecraft. This happens because that power depends on the material's absorptivity, transmissivity and reflectivity and, also, on the component's area viewed by the Sun. The solar radiation absorbed by the satellite can be estimated by the equation below where α_{solar} is the absorptivity of a component, F_i^j is the view factor from surface i to surface j, A_{sun} is the

11
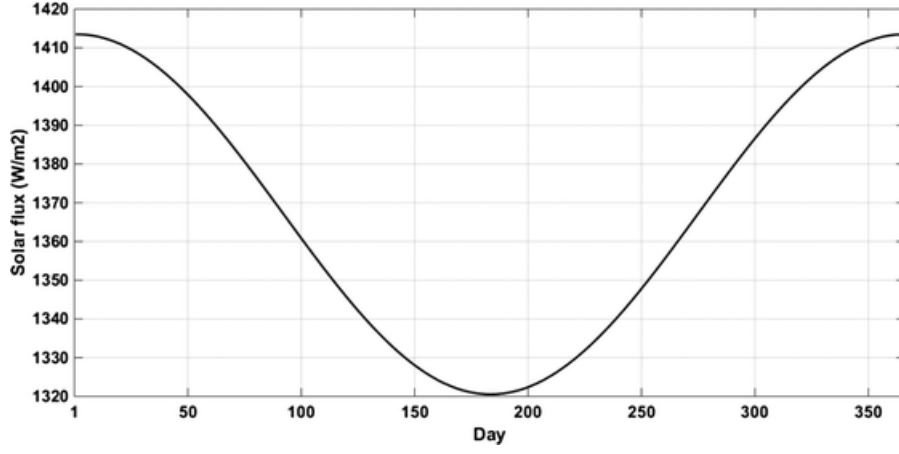
Figure 2.1: Solar Flux variation in one year [22]
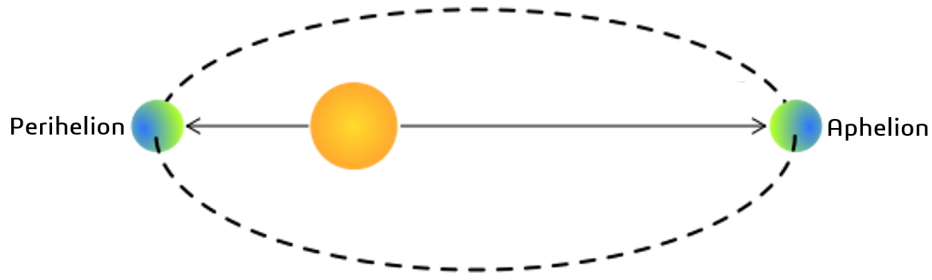
Figure 2.2: Perihelion and Aphelion [23]

area of the Sun and $\dot{q}_{solar}$ is the solar flux, as previously stated.

$$\dot{Q}_{solar\ absorbed} = \alpha_{solar} F_{Sun}^{component} A_{sun} \dot{q}_{solar} \qquad (2.16)$$

where,

$$F_i^j = \frac{1}{A_i} \int_{A_i} \int_{A_j} \frac{\cos\theta_i \cos\theta_j}{\pi R^2} dA_i dA_j \qquad (2.17)$$
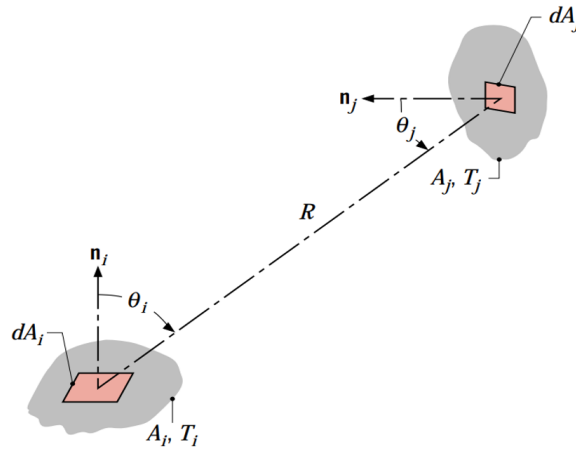
Figure 2.3: View factors representation [21]

In Eq.(2.17) θ_i and θ_j are the angles between the line that connects both surfaces and the normal

12

vector to surface i and j respectively [21]. This equation can be simplified to,

$$F_{Sun}^{component} = \int_{A_{component}} \frac{\cos \theta_{component}}{\pi R^2} dA_{component} \qquad (2.18)$$

as Sun's dimensions are too big compared to the satellite's and the solar radiation is not diffuse, which is an assumption.

For the same material and wavelength [1],

$$\alpha + \tau + \rho' = 1 \qquad (2.19)$$

For an opaque material, the radiation is not transmitted so, $\tau = 0$.

Albedo When the Sun's radiation reaches the Earth, a small part of this radiation never penetrates the atmosphere and hits the surface. This small amount is reflected directly back to space. Albedo is the fraction of incident sunlight that is reflected by a celestial body back to space and is highly variable [24]. Using other words, it is the integrated product of incident solar radiation spectral composition and the spectral reflectivity of the object [25].

As mentioned previously, the amount of radiation that is reflected, absorbed or transmitted by a body depends on its thermo-optical properties. As the Earth and other celestial bodies are a cluster of different materials and have a very complex composition this makes albedo hard to compute as it varies every second from each part of the planet (Table 2.1 and Fig. 2.4).

Table 2.1: Typical albedo values from different surfaces [26] [27] [28] [29]

Surface	Ocean Ice	Open Ocean	Bare Soil	Green Grass	Forest	Desert Sand
Typical Albedo	0.50 to 0.70	0.06	0.17	0.25	0.08 to 0.15	0.40

Having this said, the fraction of solar radiation reflected by the Earth is estimated to be $BA = 0.306$ [31]. With this value is possible to compute the reflected heat flux,

$$\dot{Q}_{solar\ reflected\ by\ Earth} = BAF_{Sun}^{Earth} A_{Sun} \dot{q}_{solar} \qquad (2.20)$$

The heat flux that reaches the satellite after the radiation from the Sun had been reflected by the Earth is given by,

$$\dot{Q}_{albedo\ absorbed} = \alpha_{solar} F_{Earth_{sunlit}}^{component} \dot{Q}_{solar\ reflected\ by\ Earth} \qquad (2.21)$$

If Eq. 2.20 is not represented, $\dot{Q}_{albedo\ absorbed}$ can be written as,

$$\dot{Q}_{albedo\ absorbed} = \alpha_{solar} F_{Earth_{sunlit}}^{component} A_{Earth} \dot{q}_{albedo} \qquad (2.22)$$
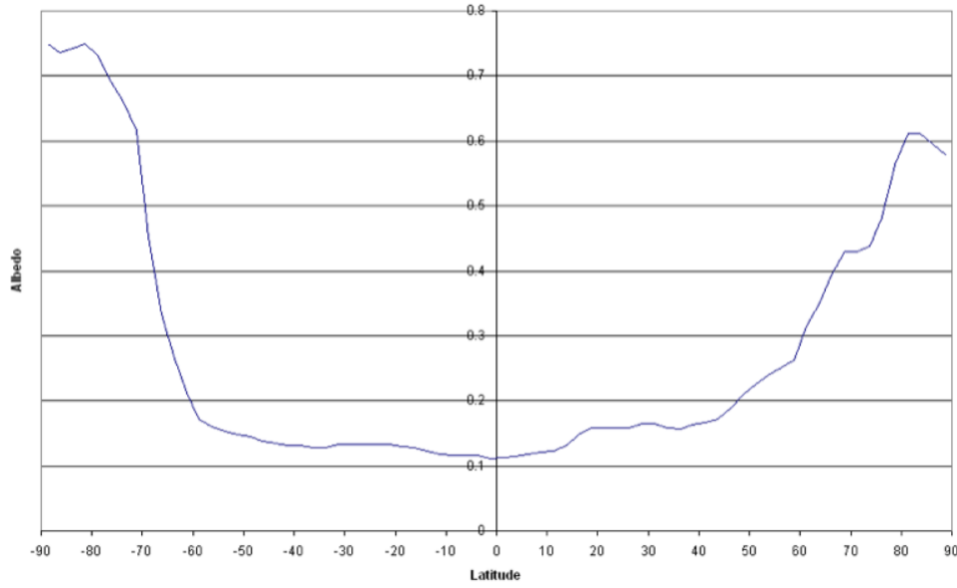
Figure 2.4: Earth's average albedo by latitude [30]

being,

$$\dot{q}_{albedo} = BAF_{Earth}^{Sun}\dot{q}_{solar} \tag{2.23}$$

These Eqs. 2.21 and 2.22 when equated, demonstrate the reciprocity relation of the view factors,

$$F_{Sun}^{Earth}A_{sun} = F_{Earth}^{Sun}A_{Earth} \tag{2.24}$$

Contrary to the previous section, Eqs. 2.21 and 2.22 cannot undergo the same simplification for the view factors calculation since the reflected radiation is diffuse so, it reaches the satellite with any direction.

Earth's Infrared Radiation All incident sunlight not reflected as albedo is absorbed by Earth and eventually re-emitted as IR energy [24]. The satellite receives this energy but, as Earth's temperature is much lower than the Sun's, the radiation emitted is located primarily in the infrared zone of the electromagnetic spectrum [32].

Once again, it is possible to use the same equations present in the solar radiation calculation if the Earth is assumed to be a black body. According to [33], it is first assumed that the Earth behaves as an opaque body i.e. the heat flux that reaches it is either reflected to space or absorbed and the heat rate emitted by the Sun and absorbed by the Earth is calculated, considering the Earth's bond albedo and the solar radiative flux that reaches it,

$$\dot{Q}_{solar\ absorbed\ by\ Earth} = \alpha_{solar}F_{Sun}^{Earth}A_{Sun}\dot{q}_{solar} \tag{2.25}$$

where,

$$\alpha_{solar} = 1 - BA \tag{2.26}$$

Considering a thermal equilibrium where the heat rate emitted by the Sun and absorbed by the Earth is

14

equal to the infrared heat rate emitted by the Earth, it is possible to obtain,

$$\dot{Q}_{infrared} = \dot{Q}_{solar\ absorbed\ by\ Earth} \tag{2.27}$$

By solving the expression, the following is obtained where $\alpha_{infrared}$ represents the component's absorptivity of infrared radiation,

$$\dot{Q}_{infrared\ absorbed} = \alpha_{infrared} F_{Earth}^{component} A_{Earth} \dot{q}_{infrared} \tag{2.28}$$

where,

$$\dot{q}_{infrared} = \alpha_{solar} F_{Earth}^{Sun} \dot{q}_{solar} \tag{2.29}$$

To conclude, since the planet Earth is provided with a significant atmosphere, it is considered that this infrared radiation is uniform for the whole Earth area i.e. the sunlit and dark sides of the Earth are considered to emit the same infrared radiation [32].

Radiation to Space As the satellite's components also emit radiation to the surrounding environment and cannot be considered as black bodies, to compute their heat flux it is necessary to modify the Stefan-Boltzmann Law and consider their emissivity,

$$\dot{Q}_{emitted} = \sigma A_{component} \varepsilon_{component} T_{component}^4 \tag{2.30}$$

Radiation from the surroundings If there is radiation being emitted by the components there is also radiation being absorbed from the surroundings. This radiation can be considered exclusively from the infrared zone of the electromagnetic spectrum, due to low temperature of the components [1]. Being i the surrounding body, $\dot{Q}_{surroundings\ absorbed}$ is given by,

$$\dot{Q}_{surroundings\ absorbed} = \alpha_{infrared} \sum_i F_i^{component} A_i \dot{q}_i \tag{2.31}$$

where,

$$\dot{q}_i = \sigma \varepsilon_i T_i^4 \tag{2.32}$$

Conduction

When the heat is transferred through a material because of the shock of its particles due to atomic and molecular activity that is called conduction. As an equilibrium state needs to be reached, the energy is always transferred from the most energetic particles to the less ones i.e. along the direction of the negative temperature gradient (from higher to lower temperatures) [21].

Considering a satellite orbiting in LEO, conduction will only occur between its components. The heat

flux resultant of heat conduction is a vector quantity and follows the Fourier's Law [21],

$$\dot{\mathbf{q}}_{conduction} = -(k_x \frac{\delta T}{\delta x}\mathbf{e}_x + k_y \frac{\delta T}{\delta y}\mathbf{e}_y + k_z \frac{\delta T}{\delta z}\mathbf{e}_z) \qquad (2.33)$$

By taking the scalar value and considering that two components of the satellite can be made of different materials, the heat rate can be given by the expression below where k represents the thermal conductivity and $R_{contact}$ is the contact resistance consequence of the imperfect contact between the two surfaces.

$$\dot{Q}_{conduction} = -\sum_i \frac{T_{component} - T_i}{\frac{L_i}{k_i A} + R_{contact} + \frac{L_{component}}{k_{component} A}} \qquad (2.34)$$

The values are assumed positive if the heat is being transferred from the surroundings to the i-th component and is negative if it is being transferred in the opposite sense.

Convection This type of heat transfer also needs matter to propagate and occurs in gases or liquids. It can be defined as an energy transfer between a surface and a moving fluid over the surface [21]. For instance, convection can be observed when the water is being boiled (Fig. 2.5). The hot water (at the base of the pot) is less dense than the cold water (on the surface). The mass of hot water will flow to the surface and the cold water will be pushed down to the base. This successive movement creates what is called convection current.

In space and with the characteristics of the ORCASat's LEO orbit, the atmosphere rarefaction is significant. The convection can be neglected.
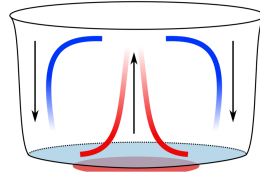
Figure 2.5: Convection currents [34]

Internal Heat Generation The electrical components of the satellite always dissipate energy due to their internal electric resistance U. Since they are not perfect electric current conductors, electrical energy is converted into thermal energy. By multiplying the electric resistance U by the current I it is possible to obtain the heat generation [10],

$$\dot{Q}_{internal} = UI \qquad (2.35)$$

2.2.2 Heat Balance

After having all the heat sources defined it is possible to establish a heat balance. For each component, the net heat rate is computed by solving the following differential equation [10],

$$\dot{Q}_{net} = \dot{Q}_{in} - \dot{Q}_{out} + \dot{Q}_{generation} \qquad (2.36)$$

It is possible to obtain the final expression that defines the heat balance,

$$mc_p \frac{\delta T}{\delta t} = \dot{Q}_{solar\ absorbed} + \dot{Q}_{albedo\ absorbed} + \dot{Q}_{infrared\ absorbed} - \dot{Q}_{emitted}$$
$$+ \dot{Q}_{surroundings\ absorbed} + \dot{Q}_{conduction} + \dot{Q}_{internal}$$

(2.37)

Where m represents the component's mass, c_p is the thermal capacity and $\delta T/\delta t$ is the temperature variation. All the heat exchange mechanisms are positive but the heat emitted by the different components is negative.

2.2.3 Transient Thermal Analysis Simulation

The thermal analysis was performed considering a transient state instead of a stationary one being possible to obtain better results as the conditions applied are similar to reality. For a transient thermal analysis, performed using *Siemens NX Space Systems Thermal*, the general equation to be solved is written as [35],

$$\mathbf{C_p}\dot{\mathbf{T}} + \mathbf{K_t}\mathbf{T} + \mathbf{R}\mathbf{T}^4 = \mathbf{HL}(t) + \mathbf{HL}(T)$$

(2.38)

$\mathbf{C_p}$ represents the heat capacity matrix, $\mathbf{K_t}$ is the heat conduction matrix, $\mathbf{R}$ is the radiation exchange matrix, $\mathbf{HL}(t)$ is a vector of applied heat loads that are constant / functions of time but not functions of temperature and $\mathbf{HL}(T)$ is a vector of nonlinear heat loads that depend on temperature. Eq.(2.38) can be solved using the *Newmark's* method. As the solution progresses, the time steps are adjusted automatically by an adaptive time stepping scheme described in [35]. It is up to the user to specify a reasonable initial time step size (as well as other initial conditions like temperatures, solution time and convergence criteria). A conservative estimate can be determined as in Eq.(2.39), where χ_{min} is the smallest element dimension in the model and α_{max} is the largest thermal diffusivity given by Eq.(2.40),

$$\Delta t_0 = \frac{\chi_{min}^2}{10\alpha_{max}}$$

(2.39)

$$\alpha = \frac{k}{\rho c_p}$$

(2.40)

Chapter 3

ORCASat

This chapter intends to show the main characteristics of the ORCASat. The payloads are described as well as the requirements that must be fulfilled in order to put the spacecraft into orbit successfully. Then, information regarding the mechanical and electrical subsystems is presented.

3.1 Payloads

The ORCASat is composed by two different payloads - Airborne Laser for Telescopic Atmospheric Interference Reduction (ALTAIR) and the Canadian Hydrogen Intensity Mapping Experiment (CHIME) - responsible for optical and radio calibration, respectively.

ALTAIR is responsible for the European Southern Observatory (ESO), the Large Syn-optic Survey Telescope (LSST), the Panoramic Survey Telescope and Rapid Response System (Pan-STARRS) and the University of Victoria (UVic) ground station calibration. The second payload is responsible for the CHIME observatory calibration [13].

3.1.1 ALTAIR

This payload will be a precision light source in orbit using an integrating sphere. According to [25], this payload provides a viable means to reduce atmospheric and instrumental extinction, which are the dominant uncertainties in measurements of dark energy and it also provides calibration opportunities to other spectrum ranges.

The structure of the integrating sphere (Fig.3.1) is divided in three different parts (sphere-front **(1)**, sphere-back **(2)** and gasket **(3)**) all made of polished aluminum 6061. Regarding the electrical components, the adopted CAD model has three more parts attached to the integrating sphere being the photodiode-case **(4)**, made of black delrin, and the photodiode-caps **(5)**, made of brass. These were discarded during the third modal analysis in order to avoid possible errors (see chapter 4).

Looking at the payload design as a whole, it consists of three primary components - a laser light source, an integrating sphere and a photodetector. The light source generates light to be emitted from the satellite; the integrating sphere ensures that the light being emitted has uniform irradiance and

18
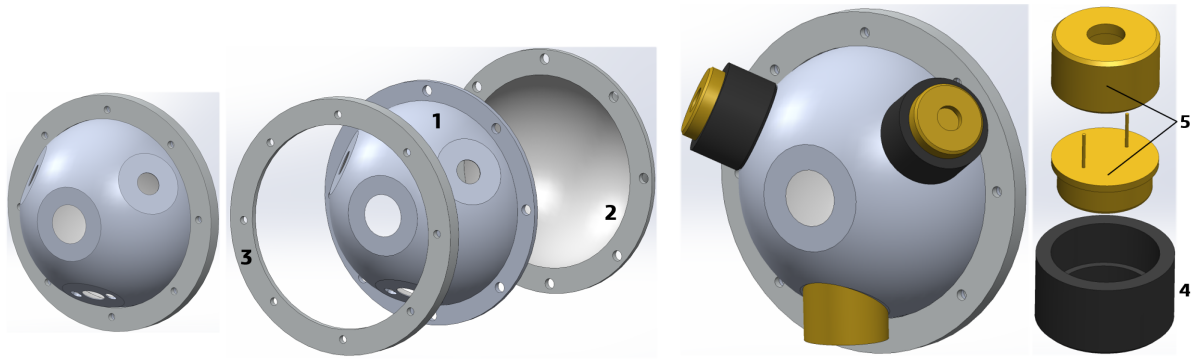
Figure 3.1: Integrating sphere structure (left) and attached electrical components (right)

maintains the output intensity and wavelength; and the photodetector measures the power of the light inside the sphere.

Although polished aluminum 6061 is used to increase the reflectivity of the sphere, a spectralon coating will also be applied on the concave surface. Spectralon is a fluoropolymer that exhibits a high Lambertian behaviour which is a property that defines the ideal "mate" or diffusely reflecting surface. This way, the apparent brightness of a Lambertian surface to an observer is the same regardless of the observer's angle of view [36] [37] [38].

The operation of this payload is described as follows (Fig. 3.2) [13]:

1) Launch from the ISS into orbit at an altitude of, approximately, 400 km and a speed of around 27600 km/h. The ORCASat's orbital period is 92.6 minutes and the expected lifetime is 1.2 years;

2) The observatories request for calibration;

3) Once the ORCASat is over the target region, the payload will sequentially flash a red laser and LED's in the visible spectrum, while onboard sensors measure the real output of each pulse;

4) At the same time, the observatories record their own measurements of the satellite's emitted light;

5) Information about the intensity and wavelength of each pulse is transmitted to the ground observatory being calibrated;

6) By comparing these two measurements, localized attenuation due to atmospheric and instrumental interference can be determined;

7) Researchers can reduce the uncertainties associated with measuring the total luminous output of stellar objects.

3.1.2 CHIME / SFU Payload

Although the parts that characterize the Canadian Hydrogen Intensity Mapping Experiment (CHIME) payload are not physically present in the model, it is important to describe one of the pillars that support this mission.

By developing a small scale UHF band antenna that can support the research efforts, this payload can be described as an orbiting transponder broadcasting a predefined bit string on multiple frequencies within the operating range of the CHIME telescope (400-800 MHz) [13]. CHIME's purpose is to map the
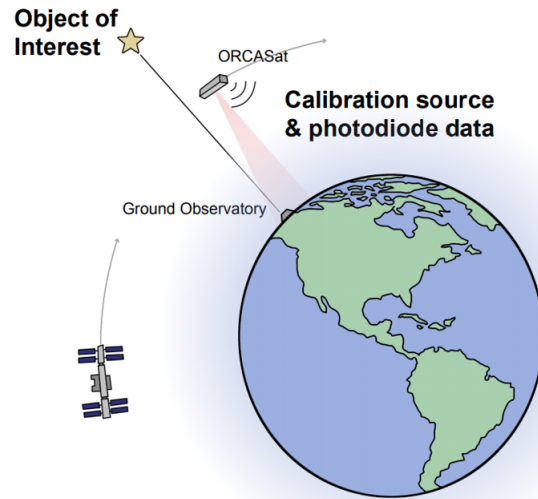
Figure 3.2: ORCASat's operation demonstration [13]

expansion history of the universe, specifically the distribution of hydrogen, with the goal of determining the dynamics of dark energy on the expansion rate of the universe [39].

CHIME requires a characterization of the telescope's complex gains, which is currently performed with natural astronomical sources sweeping the sky from east to west for the longitudinal axis however, it is difficult to use a similar source to make this characterization along the latitudinal axis. By having an artificial source in orbit with knowledge of signal characteristic moving with a longitudinal component relative to the telescope, it is possible to provide the additional information needed to fully characterize CHIME's performance [10].

Having this type of equipment in LEO is important as it has high access availability and allows for frequent calibration opportunities that translate into a higher accuracy reading for radio telescopes [12].

3.2 Requirements

The team was provided with several documents with all the requirements to send the ORCASat successfully to space. These can be from CubeSats in general, the payload carrier/deployer (NanoRacks) [40] or the program under which the CubeSat is being developed (Canadian CubeSat Project) [41]. Only those that are relevant for this project will be presented. The selected requirements can be divided in four groups - mechanical, launch environment, thermal environment and safety.

3.2.1 Mechanical Requirements (Interface deployer-satellite)

- The CubeSat shall be launched from NRCSD which can accommodate a combination of 1U, 2U and 3U up to 6U. The ORCASat dimensions shall be of a 2U ($10{\times}10{\times}22.7$ cm) with a mass less than 3.6 kg;

- ORCASat shall have XYZ coordinate system parallel to NRCSD XYZ coordinate system where $+Z$ is the direction of deployment, $+Y$ is in the direction of access panel and $+X$ forms the triad. This requirement has not been met. Figure 3.3 shows the coordinate system adopted. After discussing with

the CSA and Nanoracks, the team was authorized to use this orientation. From this point on, all the information related to the coordinate system will be relative to the ORCASat.
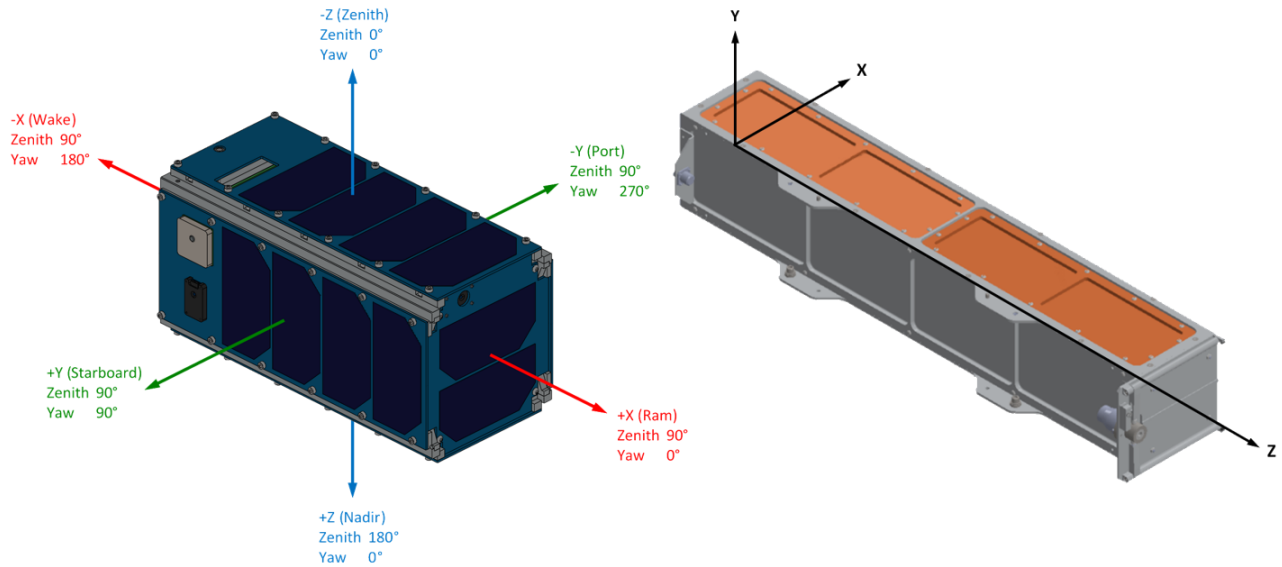
Figure 3.3: ORCASat and NRCSD coordinate systems [42]

- CubeSat's $+X$ face shall be inserted first into the deployer;

- The Cubesat shall have four rails along the X-axis which allow the satellite to slide along the rail interface of the NRCSD;

- The Cubesat rails shall be the only mechanical interface with the deployer in all axes;

- The Cubesat rail surfaces that contact the NRCSD guide rails shall have a hardness equal to or greater than hard-anodized aluminum. The most commonly material used is Aluminum alloy 6061-T6. Aluminum alloy 7075 with temper T7531 is an alternative;

- The CubeSat shall be capable of withstanding a force of 1200 N across all rail ends in the *X* axis.

3.2.2   Launch Environment Requirements

- The CubeSat's fundamental frequency shall be higher than 90 Hz during launch;

- CubeSats shall have a minimum of three mechanical deployment switches corresponding to inhibits in the main electrical system [10];

3.2.3   Thermal Environment Requirements

- The CubeSat shall be capable of withstanding the temperature range of –20ºC to 50ºC.

3.2.4   Safety Requirements

- The satellite shall comply with NASA guidelines for selecting all non-metallic materials based on available outgassing data;

- ORCASat shall not utilize any non-metallic materials with a Total Mass Loss (TML) greater than 1.0% and Collected Volatile Condensable Material (CVCM) greater than 0.1%;

By setting these constraints it is important that the decisions made anticipate that manufacturing, assembly and reliability will be simple, possible and guaranteed, respectively, keeping in mind that these will always affect the static, dynamic and thermal behaviour of the ORCASat.

3.3 Structure Subsystems

The structure accommodates most of the subsystems and payloads allowing the satellite's correct operation and, consequently, the mission. It also provides rigidity to the satellite. According to the requirements, the team has the possibility of choosing the shape of the structure and how it's machined, although there are some restrictions about its dimensions. The structure can be an assembly of various parts or it can be one physical part.

Aluminum 6061 was the material selected to compose the structure. It is present on the rail-panel, side-panel, top-cap, bottom-cap, PCB/payload brackets, magnetorquer/momentum-wheel bracket and integrating sphere. One of the advantages of this aluminum is its low density combined with good mechanical and thermal properties (Table 3.1). There are other alloys with a better strength-to-weight ratio, for example, the aluminum 7075 T6, but the 6061 is the least expensive and still presents good mechanical properties [43] [44]. The outer structural parts - rail-panel, side-panel, bottom-cap and top-cap - are anodized but the remaining are normal polished aluminum.

Table 3.1: Mechanical and Thermal Properties of Aluminum 6061 T6 [45]

Aluminum 6061 T6	
Mass Density [kg/m^3]	2711
Young Modulus (20ºC) [MPa]	68 980
Poisson Ratio	0.33
Yield Strength (20ºC) [MPa]	241.7
Ultimate Tensile Strength (20ºC) [MPa]	275.95
Thermal Expansion Coefficient (20ºC) [1/ºC]	2.24×10^{-5}
Thermal Conductivity (20ºC) [W/mK]	154.25
Specific Heat Capacity [J/kgK]	896

To facilitate the machining process, lower its price and produce less material waste, it was decided to divide the exterior structure in multiple aluminium parts. Once these are assembled, the PCB/payload brackets and integrating sphere can be coupled as well. This set defines the main structure of the spacecraft (Fig. 3.4). The modularity allows to incorporate different payloads into the volume between the brackets instead of redesigning the entire structure for every new payload. It is also possible to access the internal components of the satellite without the need of a complete disassembly [10]. Nevertheless, the modularity requires more fasteners which, consequently, increase the stress concentrations in the model and its mass.
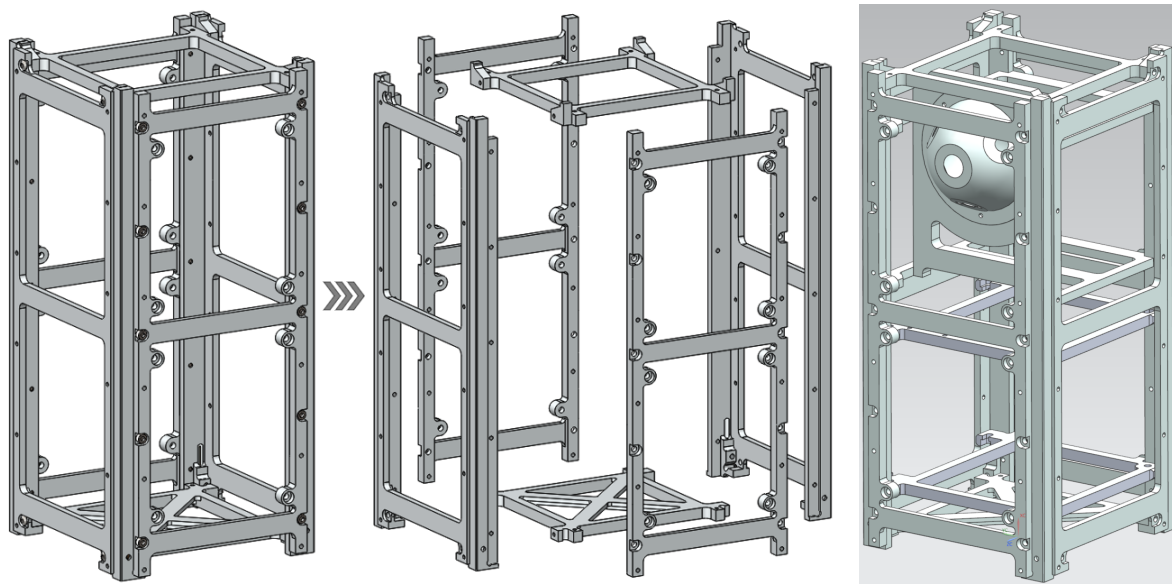
Figure 3.4: ORCASat's exterior structure (left) and ORCASat's main structure (right)

3.4 Electronic Subsystems

3.4.1 PCBs and Solar Panels

To guarantee that the satellite is able to perform its mission and remain operational, an electronic subsystem is being developed. This stack consists of a series of Printed Circuit Boards (PCBs) connected in parallel to a perpendicular backplane, forming a computer system. There are five different PCBs: ADCS, payload, OBC, TT&C and EPS, each one with its own purpose. These PCBs are placed in the respective module, between the 1U brackets, with a defined distance from each other. General information about each PCB and their location is presented (Fig. 3.5).

ADCS PCB (1) - Attitude Determination and Control System board is responsible for supporting the ADCS components such as the Z and Y magnetorquers **(7)**, momentum-wheel **(8)** and air-core **(9)** (for more information proceed to subsection 3.4.3);

Payload PCB (2) - controls the behaviour of the ALTAIR payload. It is responsible for the LEDs and laser lines of action while it converts from analog to digital the output of the measured light by the photodiodes [13];

OBC PCB (3) - OBC stands for On-Board Computer and this PCB maintains its correct operation;

TT&C PCB (4) - this board is responsible for the tracking, telemetry and command of the satellite. It is the PCB that allows the operation of the CHIME payload and the exchange of information between the ground component and the satellite;

EPS PCB (5) - EPS stands for Electrical Power System and this PCB provides physical support to the batteries **(10)** that store the power generated by the solar panels and distributes it by the subsystems that require electric energy (for more information proceed to subsection 3.4.2) [10];

Backplane (6) - connects all the printed circuit boards together to make up the complete computer

system. It is a group of electrical connectors in parallel with each other so that each pin of each connector is linked to the same relative pin of all the other connectors forming the computer bus [46].
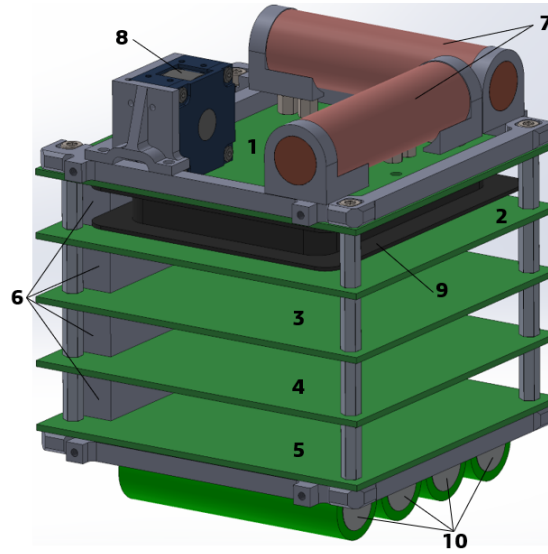
Figure 3.5: PCB stack

These circuit boards (as well as the solar panels) are made of FR-4 material and copper along the total thickness of 1.6 mm. There are four copper layers, with 35 μm of thickness each. The main purpose of the Flame Retardant (FR) is to be a non inflammable substance. The type 4 indicates that is a woven glass reinforced epoxy resin. In summary, FR-4 is a composite material made of fiberglass and epoxy resin. The properties shown in the table 3.2 are from the FR4-370HR material and were provided by the manufacturer. As an orthotropic material, its properties vary in the length direction and cross direction.

Table 3.2: Mechanical and Thermal Properties of FR4-370HR [47] [48]

FR4-370HR		
	Length Direction	Cross Direction
Mass Density [kg/m^3]	1950	
Young Modulus [MPa]	25 813.98	21 911.54
Poisson Ratio	0.177	0.171
Tensile Strength [MPa]	385.42	245.45
Thermal Expansion Coefficient [1/ºC]	5.50×10^{-5}	1.60×10^{-5}
Thermal Conductivity [W/mK]	34.56	0.3393
Specific Heat Capacity (25ºC) [J/kgK]	845	

The backplane is divided in different parts with a lot details and small features. During the structural and thermal analysis, the model was simplified and replaced by blocks with similar dimensions. These boards are composed by more than one material - ABS is the main one and copper is found on the small pins. The team decided that ABS would be the only one selected. ABS fills the outgassing requirement and it is available on the library of materials provided by *Siemens NX*. The table 3.3 presents the characteristics of this material.

Table 3.3: Mechanical and Thermal Properties of ABS [45]

Acrylonitrile Butadiene Styrene (ABS)	
Mass Density [kg/m^3]	1050
Young Modulus [MPa]	2000
Poisson Ratio	0.4
Yield Strength [MPa]	40
Thermal Expansion Coefficient [1/ºC]	7×10^{-5}
Thermal Conductivity [W/mK]	0.17
Specific Heat Capacity [J/kgK]	1800

3.4.2 Batteries

The model has room for four Lithium Ion NCR18650B 3350 *mAh* batteries from Panasonic (Fig. 3.6). The mechanical properties provided by the manufacturer were scarce (table 3.4). During the vibration and thermal analysis, some adaptations to the model had to be done (see chapter 4).

Table 3.4: Properties of each battery cell [49]

Batteries (Lithium Ion NCR18650B 3350mAh)	
Mass [g]	48.5
Height [mm]	65.3
Diameter [mm]	18.5
Nominal Voltage [V]	3.6
Thermal Conductivity [W/mK]	25
Specific Heat Capacity (25ºC) [J/kgK]	675
Charging Temperature Range [ºC]	0 to +45
Storage Temperature Range [ºC]	-20 to +50
Discharge Temperature [ºC]	-20 to +60

Figure 3.6: Panasonic Lithium Ion NCR18650B 3350 battery [50]

3.4.3 ADCS Components

The upper PCB provides physical support to the magnetorquers and momentum wheel which are actuators of the ADCS system. These components control the ORCASat in terms of orientation / position maintaining it, even when an external disturbance occurs. Some other sensors are also required, such as, a GPS receiver and sun sensors (table 3.5).

Table 3.5: Information regarding the GPS, Sun Sensors and Momentum Wheel

Component	Model	Quantity	Dimensions [mm]	Mass [g]
GPS	NovAtel OEM719 [51]	1	71×46×11	31
Sun Sensor	Hyperion SS200 [52]	4	24.66×15×3.50	3
Momentum Wheel	Hyperion RW210 [53]	1	25×25×15	21 / 32 / 48
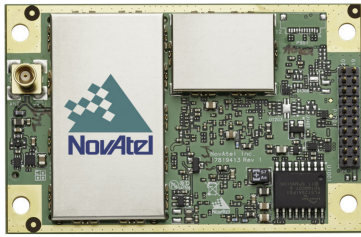
Figure 3.7: GPS receiver [51]

Figure 3.8: Sun sensor [52]
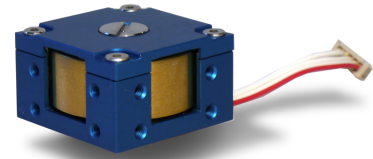
Figure 3.9: Momentum Wheel [53]

Apart from the bracket, the momentum wheel is an assembly of four parts. Aluminum 6061 was the material selected for the structural parts and brass was chosen for the wheel. Brass is available on the software and some of its properties are shown (table 3.6).

Table 3.6: Mechanical and Thermal Properties of Brass [45]

Brass	
Mass Density [kg/m^3]	8409
Young Modulus [MPa]	1.034×10^5
Poisson Ratio	0.35
Yield Strength [MPa]	440
Ultimate Tensile Strength [MPa]	1100
Thermal Expansion Coefficient [1/^{o}C]	2.124×10^{-5}
Thermal Conductivity [W/mK]	116
Specific Heat Capacity [J/kgK]	380

The magnetorquers are divided in three parts - the core and two brackets. The brackets are made of aluminum 6061 and the core is composed by copper. Both materials are provided by *Siemens NX* and the properties of copper are presented in the table below (table 3.7).

Finally, delrin was the selected material for the air core. Since it is not provided by the program, it was difficult to fill all the required fields for its mechanical and thermal properties. The main characteristics are presented (table 3.8).

Table 3.7: Mech. / Therm. Prop. of Copper [45]

Copper	
Mass Density [kg/m^3]	8920
Young Modulus [MPa]	1.14×10^5
Poisson Ratio	0.31
Yield Strength [MPa]	30
Ultimate Tensile Strength [MPa]	207
Thermal Expansion Coefficient [1/^{o}C]	1.17×10^{-5}
Thermal Conductivity [W/mK]	387
Specific Heat Capacity [J/kgK]	385

Table 3.8: Mech. / Therm. Prop. of Delrin [54] [55]

Delrin	
Mass Density [kg/m^3]	1419.98
Young Modulus [MPa]	2413.16
Poisson Ratio	0.35
Yield Strength [MPa]	62.05
Ultimate Tensile Strength [MPa]	69
Thermal Expansion Coefficient [1/^{o}C]	8.46×10^{-5}
Thermal Conductivity [W/mK]	0.3603
Specific Heat Capacity [J/kgK]	1465

3.4.4 Solar Cells

As most satellites, the ORCASat uses solar energy to generate electrical power. Thereby, 17 solar cells are distributed by the external surfaces that have direct contact with sunlight. There are six faces for the placement of the solar cells but only five are available since the nadir surface is occupied by the patch antenna and does not receive enough sunlight to implement solar cells. The selected solar cells are supplied by AZUR SPACE and are 30% Triple Junction GaAs Solar Cell Assembly with the type TJ Solar Cell Assembly 3G30A (Fig. 3.9)

The solar cells are made of a material composed by GaInP/GaAs/Ge on Ge substrate. Since most of the mechanical and thermal properties were not provided by the supplier, the information available was scarce. It was decided to use the same properties applied in previous studies performed at CfAR.

Table 3.9: Properties of the solar cells [56] [57] [10]

Solar Cells (AZUR SPACE Solar Power GMBH)	
Base Material	GaInP / GaAs / Ge on Ge substrate
Anti-Reflective Coating	TiOx / Al2O3
Dimensions [mm]	$40.15 \times 80.15 \pm 0.1$
Surface Area [cm^2]	30.18
Mass Density [kg/m^3]	4214.29
Mass [g]	3.56
Thickness and Coverglass Thickness [μm]	280 ± 25 / 100
Thermal Conductivity [W/mK]	57
Specific Heat Capacity [J/kgK]	325
Thermal Expansion Coefficient [1/^{o}C]	6.03×10^{-6}
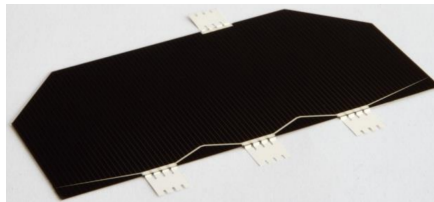
Figure 3.10: AZUR SPACE solar cells [56]

Chapter 4

Structural Analysis

Before being launched, the spacecraft is subjected to vibration loads from its transportation on the way to the launch site by aerial or land vehicles. Some vibrations can also be originated when the Cubesat is installed on its deployer.

During launch to orbit, the satellite is exposed to various external loads of higher amplitudes resulting from the vibroacoustic noise, propulsion system, stage separation, wind gust, aerodynamic flows, among others, being structurally more challenging [58]. This is a critical aspect of the mission since it must be assured that the spacecraft can handle all the induced disturbances during this phase.

Once in orbit, the satellite is mostly subjected to micro-vibrations, referred as low-level mechanical vibrations or disturbances in the microgravity environment [59]. Usually, they are ignored, for example, on typical telecommunication satellites, however, spacecrafts with optical instruments and cameras are generally the most affected by micro-vibration issues since the accuracy and stability required for these satellites instruments line of sight have increased over the years [60].

Considering the satellite as an isolated system due to the small environmental damping in space, the mechanical energy produced by the different moving instruments is dissipated into its system. These mechanical disturbances are characterised by forces and torques that appear at the interface between the equipment and the satellite and are propagated through the structure to the sighting instruments [61]. As they can persist for a long time, the working environment of on-board instruments is deteriorated, downgrading its precision [59]. Micro-vibrations can also be amplified by structural resonances thus making their prediction complicated [60]. Therefore, as they usually involve the flexible modes of the spacecraft structure rather than its rigid body motion, these disturbances can't be controlled or reduced by the ADCS system.

Micro-vibrations can emanate from various sources on a typical spacecraft, notably subsystems with moving parts such as reaction and momentum wheels assemblies, cooler and pointing mechanisms or switches. Besides that, micro-vibrations can also arise from non-moving systems such as electronics and sensors, the release of strain energy at structural interfaces (joints, latches, hinges) during "thermal snap" events and the bending of solar arrays and antennas due to sudden temperature change [60].

It is extremely important to do a dynamic and static analysis in order to predict how the structure behaves in the presence of loads but also what modal frequencies characterize it. The last mechanical requirement on section 3.2.1 and the first launch environment requirement on section 3.2.2 must be fulfilled in this chapter - from Nanoracks, *the Cubesat shall be capable of withstanding a force of 1200 N across all rail ends in the X axis*; and, from the CSDC, *the spacecraft shall have a fundamental frequency of at least 90 Hz in each axis*. The latter requirement is directly related to the vibration environment to which the satellite is subjected while it is being transported into orbit and to the lowest natural frequencies of the launch vehicle itself. This way, resonance originated from the coupling between the spacecraft and launch vehicle may be prevented. The requirement is not part of the Canadian Cubesat Project but will be used as a reference.

Using *Siemens NX 9.0*, a modal analysis is performed in order to verify the modal frequencies of the ORCASat and respective mode shapes. The goals of this chapter is to compare the obtained results with the experimental ones and, possibly, obtaining a validation of the method used and to verify if the main structure can handle a load of 1200 *N* along the rails.

During the study, if the satellite does not satisfy the requirements, a solution must be developed.

4.1 Finite Element Analysis (FEA)

A bottom-up approach was adopted to produce the final finite element model i.e. a simplified model is simulated, and it will progress to a more complex structure until the final model is reached.

To perform the simulations, three types of files (*.prt*, *.fem* and *.sim*) are required - the *.prt* file contains the CAD model; the *.fem* file is where the mesh is generated and all the materials are assigned to the different components; and, the *.sim* file is used to give constraints to the model, assign boundary conditions, establish connections between the different parts and, also, run the simulations and obtain results.

To import the model from *Solidworks* software to *Siemens NX* without ruining the model or the assembly contacts, the *Solidworks* file should be saved as *.IGES* and should be imported as is to *Siemens NX*. On *NX*, the *New* command should be used followed by the *assembly* one. Once the new file is open, by choosing the *import from IGES* command, the advanced options as *smooth B-surface*, *Automatic Sewing of Surfaces* and *Simplify* should be selected. The model must appear without any errors.

4.1.1 Idealization Process

Since various parts of the ORCASat are complex and very detailed, the model should be simplified to obtain a more uniform mesh. This way, the simulations will be less time consuming and mesh errors are most unlikely to occur. As stated in [1], the mesh generation process is simplified because it reduces the need of using large number of elements to properly mesh the small details and it also avoids abrupt transitions in mesh size near the small feature zones.

It must be proven that this idealization process does not affect the dynamic behavior of the structure otherwise, the simplifications will only be considered when there is no better solution to obtain data without errors.
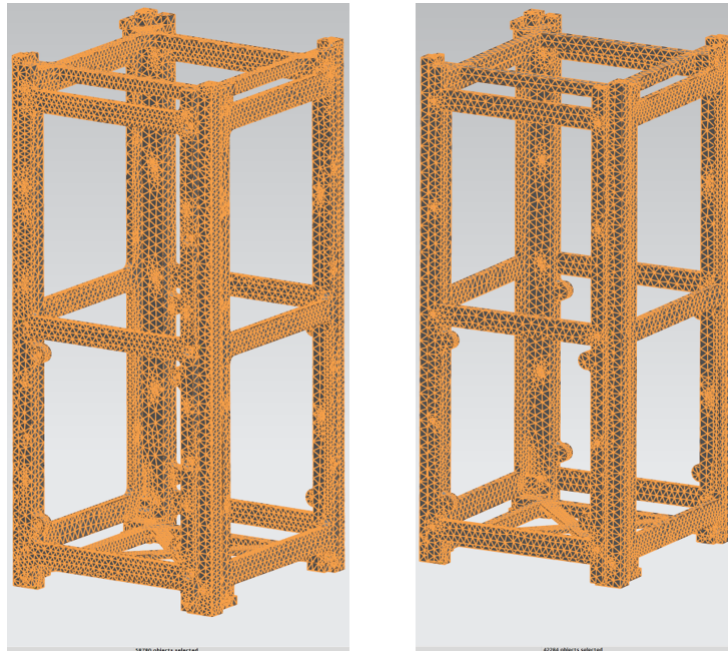
Figure 4.1: Number of elements before and after an idealization process. The mesh characteristics are the same with an element size of 4 mm. The non-idealized model presents 58 780 elements while the idealized model presents 42 284 elements

The main adopted simplifications are listed below. Some of these idealizations were different depending on the model used. For instance, on the first model, only the screw holes responsible for connecting the rail-panel, side-panel, top-cap and bottom-cap were considered. However, in the following models, all of them were already taken into account.

- **Top-cap:** fillet and chamfered edges removed;
- **Bottom-cap:** fillet and chamfered edges removed;
- **Side-panel:** fillet and chamfered edges removed;
- **Rail-panel:** fillet and chamfered edges removed;
- **1U bracket:** fillet and chamfered edges removed;
- **Batteries:** small design features removed;
- **Air core:** round surfaces and fillet edges removed;
- **Magnetorquer brackets:** small holes removed and one of the dimensions increased in order to touch the ADCS PCB. One of the four magnetorquer brackets was "floating", which would not happen on the real satellite. As the results related to the vibration test would be influenced, it was decided to increase its length;
- **Momentum wheel:** all the electronic components, small holes, fillet and chamfered edges removed. The model was provided by the manufacturer and it was a very detailed assembly with all the electronics presented on it (represented as small extruded boxes) but some of its features presented

errors. The best solution was to simplify this assembly at its maximum;

– **Momentum wheel bracket:** unnecessary screw holes removed. One of the surfaces was completely modified in order to avoid mesh errors;

– **PCB's (including solar panels):** rounded edges removed;

– **Sphere bracket:** fillet and chamfered edges removed;

– **Solar cells:** transformation to 2D surfaces;

– **Integrating sphere:** in the second model, the sphere-front part was transformed into a 2D surface because one of its features had a small thickness and the program was not letting the use of a 3D mesh even after redoing the model. This was due to the presence of the eletrical components as the photodiode-case and photodiode-caps attached to its surface. In the third model those components were removed and the 2D surface was not necessary;

– **Fasteners:** substitution by 1D beams because their length is larger than the other dimensions.

It was chosen not to include the small electronic components (like sensors, RBF switch, among others) in this study because they were not concluded. The PCB stack could be transformed into 2D surfaces, as the solar cells, due to their small thickness however, in order to approximate the results of both computational and real models, this idea was discarded.

After the idealization process it was verified if the original components and the idealized ones had the same structural behavior. All the changes were considered acceptable if the error between the modal frequencies was below 10%. The parts were individually considered and simulated with free-free vibration conditions (no loads and no constraints applied). The data obtained by this study for some components as the bottom-cap (tables 4.1, 4.2 and Fig. 4.2), rail-panel (tables 4.3, 4.4 and Fig. 4.3) and top-cap (tables 4.5, 4.6 and Fig. 4.4) is presented. The reader is advised to access the appendix A to visualize the results obtained for the other components.

Table 4.1: Bottom-cap idealization process

bottom-cap			
Modes	Real Freq. [Hz]	Idealized Freq. [Hz]	Error [%]
7	988.7	976.1	1.27
8	2133	2079	2.53
9	2530	2521	0.36
10	3490	3464	0.74
11	3793	3724	1.82
12	4048	3768	6.92
13	4733	4536	4.16
14	5680	5169	9.00
15	5743	5362	6.63
16	6178	5798	6.15
17	6202	5898	4.90
18	7045	6652	5.58
19	7403	6905	6.73
20	7566	7294	3.59

By analyzing the results, the idealized parts can be considered as fare representatives in estimating the natural frequencies of the original parts. For the components where the error was higher than 10%, the idealization was considered valid as well and justifications can be found below.

Table 4.2: Bottom-cap idealization convergence

bottom-cap					
Non-idealized			Idealized		
Element Size [mm]	Number of Nodes	Mode 7 [Hz]	Element Size [mm]	Number of Nodes	Mode 7 [Hz]
5	9742	1004	5	7778	1007
4	13174	998.1	4	10544	988.1
3	22786	993.9	3	14903	988
2	44892	991.2	2	27539	980.8
1	192181	988.8	1	142969	976.4
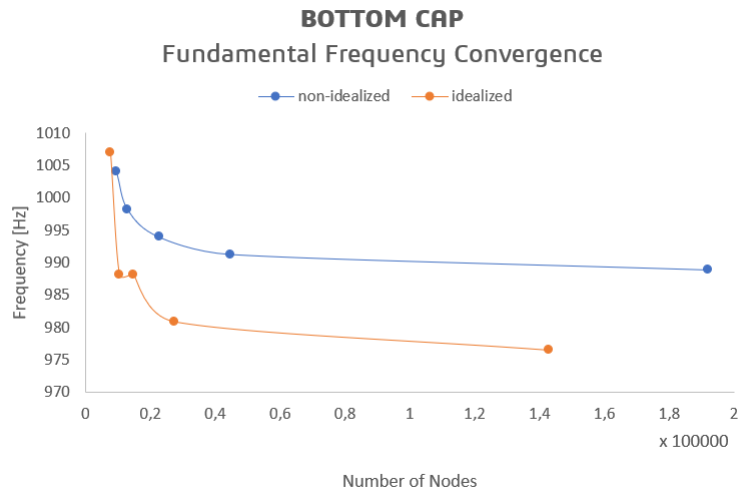
Figure 4.2: Bottom-cap idealization convergence

Table 4.3: Rail-panel idealization process

rail-panel			
Modes	Real Freq. [Hz]	Idealized Freq. [Hz]	Error [%]
7	276.5	274.4	0.76
8	801.4	799	0.30
9	1003	956.3	4.66
10	1078	1076	0.19
11	1115	1101	1.25
12	1337	1334	0.22
13	1640	1613	1.65
14	1985	1971	0.70
15	2199	2197	0.09
16	2335	2305	1.28
17	2776	2745	1.12
18	2876	2833	1.50
19	3367	3345	0.65
20	3428	3419	0.26

Table 4.4: Rail-panel idealization convergence

rail-panel					
Non-idealized			Idealized		
Element Size [mm]	Number of Nodes	Mode 7 [Hz]	Element Size [mm]	Number of Nodes	Mode 7 [Hz]
5	24886	282.3	5	22063	281.4
4	31332	281.5	4	25844	281.1
3	48401	279.1	3	36988	279
2	104766	277.5	2	81519	276.4
1	462071	276.1	1	426218	274.4
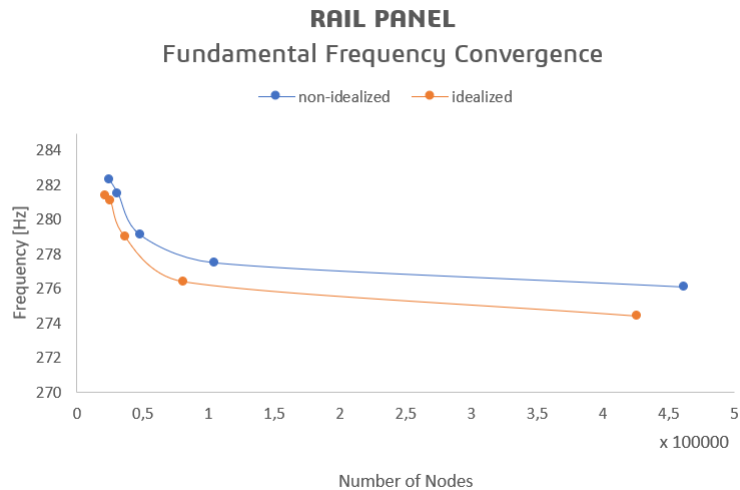
Figure 4.3: Rail-panel idealization convergence

Table 4.5: Top-cap idealization process

	top-cap		
Modes	Real Freq. [Hz]	Idealized Freq. [Hz]	Error [%]
7	660.8	653.4	1.12
8	1057	997.7	5.61
9	1961	1957	0.20
10	2130	2129	0.05
11	2369	2363	0.25
12	2643	2626	0.64
13	2860	2843	0.59
14	3395	3244	4.45
15	3589	3466	3.43
16	5337	4902	8.15
17	6576	6409	2.54
18	6709	6633	1.13
19	6722	6662	0.89
20	7138	7043	1.33

Table 4.6: Top-cap idealization convergence

	top-cap				
Non-idealized			Idealized		
Element Size [mm]	Number of Nodes	Mode 7 [Hz]	Element Size [mm]	Number of Nodes	Mode 7 [Hz]
5	8285	673.4	5	5274	690.6
4	9628	675.5	4	6417	684.6
3	16752	664.2	3	9293	666.5
2	35094	662.3	2	19345	657.5
1	137674	660.9	1	113866	653.6

– **Magnetorquer Bracket:** for the second idealization, with the changed dimension, it was expected that the error would increase. However, the dimension needed to be modified otherwise the analysis would be useless (Table A.3);

– **Momentum Wheel Bracket:** the errors are mostly above 10% as one of its surfaces was completely modified. This was done because the *SolidWorks* model revealed unrealistic shell-like surfaces that in future simulations would lead to errors (Table A.8);

– **Integrating Sphere (front):** it was expected that, by changing this part from a 3D surface to a

TOP CAP
Fundamental Frequency Convergence
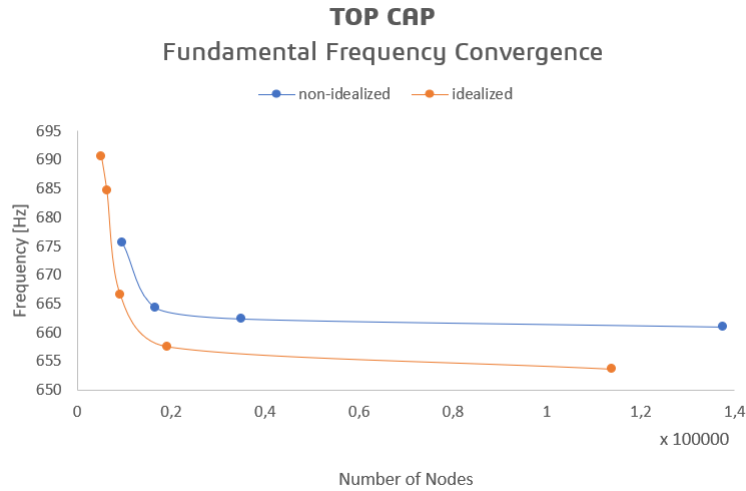
Figure 4.4: Top-cap idealization convergence

shell-like equivalent, the modal frequencies would suffer modifications. The errors obtained from mode 7 to 20 were always below 13% and this simplification was needed to avoid fatal errors related to mating different meshes (Table A.11).

4.1.2 Finite Element Method Models

With the idealization process concluded, the *.fem* file must be created which represents the actual satellite tested [1]. As stated before, a bottom-up approach was adopted because the satellite consists on a large number of parts assembled together that requires a great number of contacts and connections between them. Three finite element models were developed and depending on the model, there were small changes on the meshes because of trial and error methods.

FEM Model 1 consists on the external structure, including the rail-panels, side-panels, top-cap and bottom-cap;

FEM Model 2 consists on every component of the satellite except the solar panels, solar cells and boards. While this model was being analyzed, the boards were still under development that is why they were only added to the last model;

FEM Model 3 all the components are included. There were changes between the FEM 2 and FEM 3, explained later in this thesis.

The three models are composed by 1D, 2D and 3D elements.

1D elements are used to represent the screws. In FEM 3, the screw that connects the PCB stack, which is a multiple connected bolt segment with male and female standoffs, was modeled as a cylinder using 3D elements. Three main steps are necessary to create a 1D element - 1) access the command *1D connection*, type *Point to Edge*, select the source and target which will be the screw hole and, in the element properties, *RB2* should be selected. This method must be done twice, in order to connect the

34

nodes later; 2) access the command *1D connection*, type *Node to Node*, select one node at a time and, in the element properties, *CBAR* should be selected; 3) once the connection is created, the user should edit the CBAR connections by choosing the material and the diameter of the element;

2D elements are used for the solar cells. In FEM 2, the integrating sphere was transformed to a shell surface as well. To perform this transformation - 1) the user should open the *.prt* file and select the desired component; 2) use the command *Midsurface by Face Pairs*; 3) the various surfaces of the component must be selected and a 2D model should appear. It is important to mention that the program creates a shell in the mid distance between the upper and lower surface of the 3D component. In the third model, *Siemens NX* was also informing the author to create a midsurface in the back part of the integrating sphere which would lead to an unrealistic model and increase the errors regarding the idealization. To avoid this simplification, it was possible to represent both front and back sphere parts with 3D elements at the cost of removing the attached electrical components;

3D elements were used for the rest of the ORCASat components.

On tables 4.7, 4.8 and 4.9 it is listed all the information related to the mesh of the three finite element models. Some properties and mesh qualities were modified along the analysis because the ORCASat's CAD model is still under development by the *Mech & Thermals* team. Therefore, the main goal was always to follow the updates, being these discarded only when it was no longer possible. From FEM 2 to FEM 3 some 3D tetrahedral meshes (*CTETRA*) were replaced by 3D swept meshes (*CHEXA*) since, in the meantime, the viability of this command was discovered, it would give better results and decrease the simulation time.

Table 4.7: FEM model 1 mesh information

Component	Element Type	Material
side-panel / rail-panel / top-cap / bottom-cap	CTETRA(10)	aluminum 6061
screws	CBAR	steel
connections	RBE2	*not defined*

Table 4.8: FEM model 2 mesh information

Component	Element Type	Material	Thickness [mm]
side-panel / rail-panel / top-cap / bottom-cap	CTETRA(10)	aluminum 6061	-
PCB brackets	CTETRA(10)	aluminum 6061	-
batteries	CTETRA(10)	steel	-
PCB	CTETRA(10)	FR4	-
air-core	CTETRA(10)	delrin	-
magnetorquer brackets	CTETRA(10)	aluminum 6061	-
magnetorquers	CTETRA(10)	copper	-
momentum wheel bracket	CTETRA(10)	aluminum 6061	-
momentum wheel [front / back]	CTETRA(10)	aluminum 6061	-
momentum wheel [wheel]	CTETRA(10)	brass	-
integrating sphere [gasket / back]	CTETRA(10)	aluminum 6061	-
integrating sphere [front]	CQUAD8	aluminum 6061	1.5
integrating sphere [photodiode case]	CTETRA(10)	delrin	-
integrating sphere [photodiode cap]	CTETRA(10)	brass	-
screws	CBAR	steel	-
connections	RBE2	*not defined*	-

Table 4.9: FEM model 3 mesh information

Component	Element Type	Material	Thickness [mm]
side-panel / rail-panel / top-cap / bottom-cap	CTETRA(10)	aluminum 6061	-
PCB brackets	CTETRA(10)	aluminum 6061	-
batteries	CTETRA(10)	steel	-
PCB	CHEXA(8)	FR4	-
air-core	CTETRA(10)	delrin	-
magnetorquer brackets	CTETRA(10)	aluminum 6061	-
magnetorquers	CTETRA(10)	copper	-
momentum wheel bracket	CTETRA(10)	aluminum 6061	-
momentum wheel [front / back]	CTETRA(10)	aluminum 6061	-
momentum wheel [wheel]	CTETRA(10)	brass	-
integrating sphere [gasket / front / back]	CTETRA(10)	aluminum 6061	-
solar cells	CQUAD8	*defined previously*	0.28
solar panels	CHEXA(8)	FR4	-
boards	CHEXA(8)	ABS	-
multiple connected bolt segment	CHEXA(8)	steel	-
screws	CBAR	steel	-
connections	RBE2	*not defined*	-
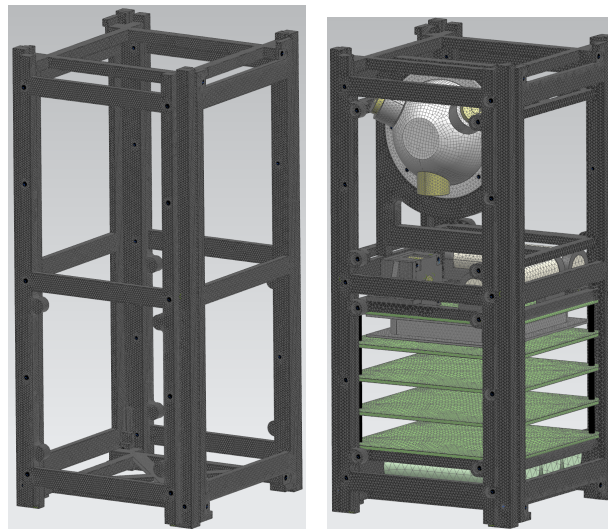
Figure 4.5: FEM model 1 (left) and FEM model 2 (right)
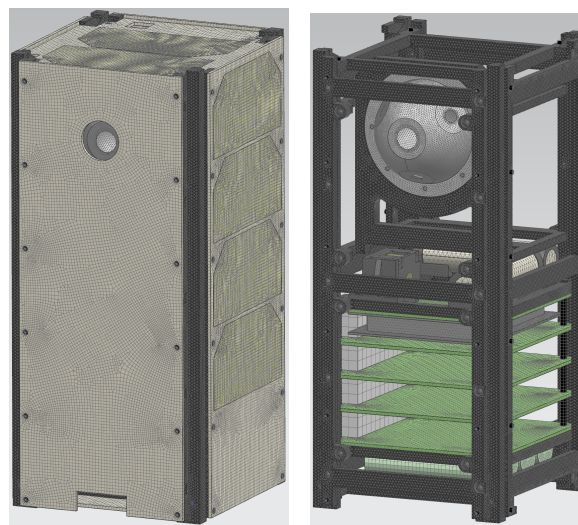
Figure 4.6: FEM model 3

The analysis is performed on the *.sim* file. To prepare the model, boundary conditions must be assigned as well as surface contacts and loads (not applied in the vibration analysis since the purpose is to know the natural frequencies and corresponding modes of vibration).

As the most significant source of vibrations is the launch vehicle, the modal analysis shall be done for a structure under its launch configuration, accommodated in the deployment system [10]. According to NanoRacks, the only parts of the satellite in contact with the deployer are the four outer rails (Fig. 4.7). Then, the constraints should be applied along the rails. The deployer fully constraints the satellite rails in the X direction, but it is allowed to move in Y and Z directions due to clearance. However, if the X direction is constrained tightly enough, the friction force created is enough to surpass the force generated by the induced accelerations. Because the provided documentation is not clear, this study will follow the same procedure as in [1] and both boundary conditions will be analysed: satellite with fixed bases and satellite with fixed rails.
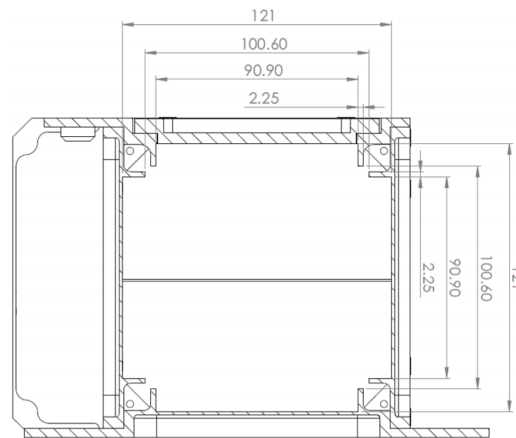
Figure 4.7: NanoRacks deployer mechanical interface (dimensions in mm) [40]

To know if the ORCASat is able to withstand a force of 1200 N in the X direction, two different environments were created. In the first one, the force was applied on top (-X direction) and the spacecraft was fixed at the bottom. In the second one, the force was applied at the bottom (X direction) and the spacecraft was fixed at the top. Both results are expected to be different since the structure is not symmetrical.

To establish the surface contacts the command *Simulation Object Type* should be selected followed by the *surface-to-surface contact* or *surface-to-surface gluing*. These conditions must be assigned otherwise, there is no way the program "understands" that several interconnected parts exist and the results would show components penetrating each other, giving incorrect data for the natural frequencies and mode shapes. The option *surface-to-surface contact* is used in surfaces that are connected by screws and the option *surface-to-surface gluing* is used in the other cases (for instance, the solar cells attached to the solar panels). These contacts can be assigned automatically or by hand. Initially, the contacts were done by hand but, in the last models, the *surface-to-surface contacts* were assigned automatically while the *surface-to-surface gluing* was done by hand since much better results were obtained as well as a better convergence and less warning errors.

The command *mesh mating*, on the *.fem* file, influences the contacts in the model as well. The user should be careful and select *mesh mating free coincident* and not *mesh mating glue coincident*, otherwise this condition will overwrite the *simulation object type*. Initially, *mesh mating free coincident* was used since it allowed the software to align the meshes on both source and target face without connecting them. These meshes would have the same element pattern by the existence of duplicate nodes at the interface between the source and target faces. However, in the most complex models, there were multiple components with different mesh sizes and the refinement of the mesh was compromised in the contact areas. Thus, the author decided not to use it.

As stated in [10], defining contacts is not straightforward, leading to a long process of trial and error where, in each trial, it is necessary to wait for an iterative method to resolve the contacts between the components before proceeding to the eigenvalue extraction. This process consumed weeks to be solved.

By establishing all the constraints above, the following solutions must be created:

– **Vibration Analysis:** *Static Subcase* before *Eigenvalue Method Subcase* of *Solution 103 – Real Eigenvalues*;

– **Linear Static Analysis:** *Solution 101 Linear Statics – Global Constraints*.

To evaluate the results from each finite element model correctly, a convergence analysis must be done. This study was performed by going from coarse meshes to refined ones.

In the next sections, the preparation of the mesh for each of the three models, the problems faced while preparing the model, the adaptations done in order to have better results and the commands used are explained.

First FEM Model

After assigning materials to the mesh it must be assured that the model's final mass is similar to real one to achieve a more accurate model since the mass affects the structure natural frequencies.FEM 1, all of its components had their mass compared since the rail-panels, side-panels, bottom-cap and top-cap were already machined (Fig. 4.8). Using the *Solid Properties Check* command and selecting all the elements (element size of 1.5 mm / 557 996 nodes), the mass is, approximately, 408.8 g while the real model has 414.3 g (36.5 g from the bottom-cap; 31.8 g from the top-cap; and 346.0 g from the two side-panels and two rail-panels) giving an error of 1.3% between the numerical and real model. The density of the Aluminum 6061 was changed from 2711 kg/m^3 to 2747.47 kg/m^3.

The fundamental frequency convergence study is presented (Fig. 4.9). The values vary between the intervals of [720-750] and [1230-1300] Hz for the cases where the bases and rails are fixed, respectively. The analysis was performed for both idealized and non-idealized models (Table 4.10) since the time needed for the simulations was low. The error in both cases is always below 10% proving that the idealization process is a good way to obtain similar results in less time.
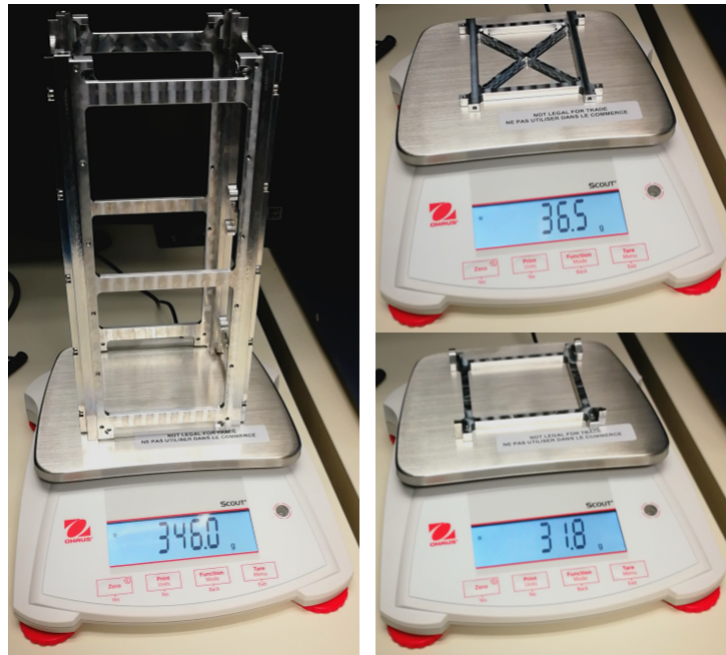
Figure 4.8: Mass of the real model
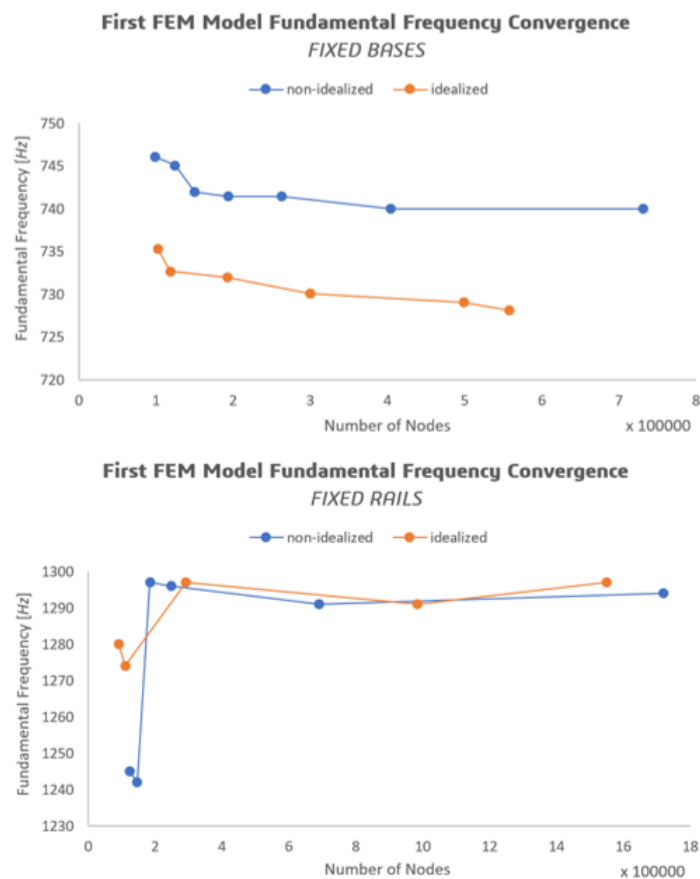
Figure 4.9: First FEM Fundamental Frequency Convergence

Regarding the linear static analysis, the integrating sphere and 1U brackets were added to FEM 1 representing the main structure. To run a simulation where screws are presented in the model, one must

Table 4.10: Error between modal frequencies in idealized and non-idealized FEM 1

	Fixed Bases			Fixed Rails		
Mode	Ideal. Freq. [Hz]	N-Ideal. Freq. [Hz]	Error [%]	Ideal. Freq. [Hz]	N-Ideal. Freq. [Hz]	Error [%]
1	728.1	740	1.61	1297	1294	0.23
2	787.5	809.2	2.68	1786	1798	0.67
3	884.1	892.2	0.91	2014	1913	5.28
4	1037	1039	0.19	2109	1930	9.27
5	1045	1063	1.69	2110	1980	6.56
6	1327	1343	1.19	2135	2040	4.66
7	1392	1397	0.36	2138	2043	4.65
8	1483	1492	0.60	2195	2112	3.93
9	1753	1752	0.06	2208	2161	2.17
10	1763	1765	0.11	2286	2162	5.73

apply a *bolt pre-load* value. As the value chosen could easily alter the results, one simplification adopted in this study was the removal of all screws and bonding all of its surfaces using the *surface-to-surface gluing* command. This can be considered as a safe representation since the main structure is going to be totally epoxied before launch. In this study the model was not idealized.

Applying the force on the top (Fig. 4.10) or bottom (Fig. 4.11) of the main structure showed different but approximated results (Fig. 4.12). It is concluded that the ORCASat's structure can handle the load perfectly. The values for the *stress elemental – Von Mises* are below 15 MPa which is under the stress required for the aluminum to start showing plastic deformations. The yield strength of aluminum 6061 is 241.7 MPa.
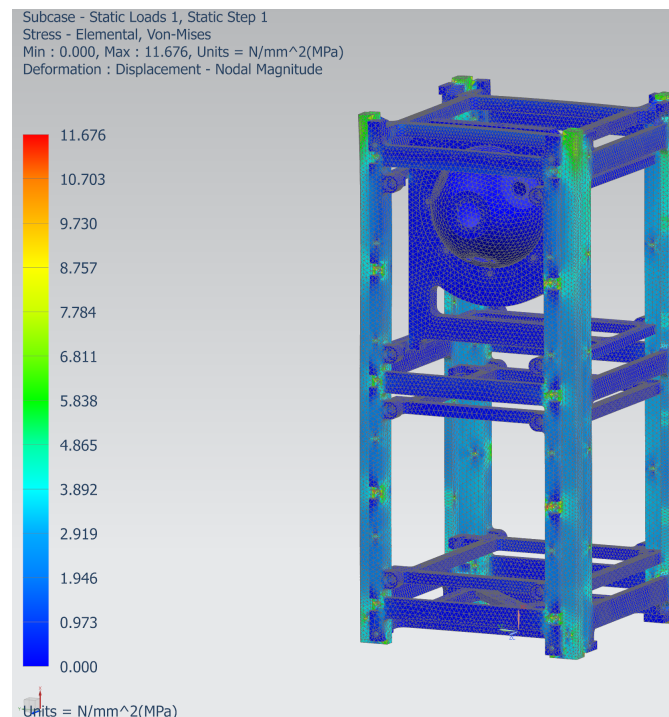
Figure 4.10: Stress analysis with force applied on the top
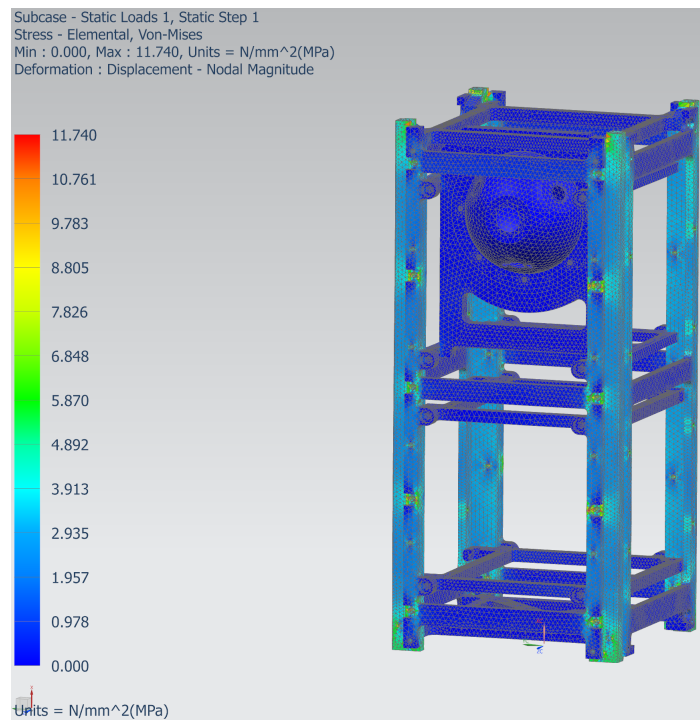
Figure 4.11: Stress analysis with force applied at the bottom
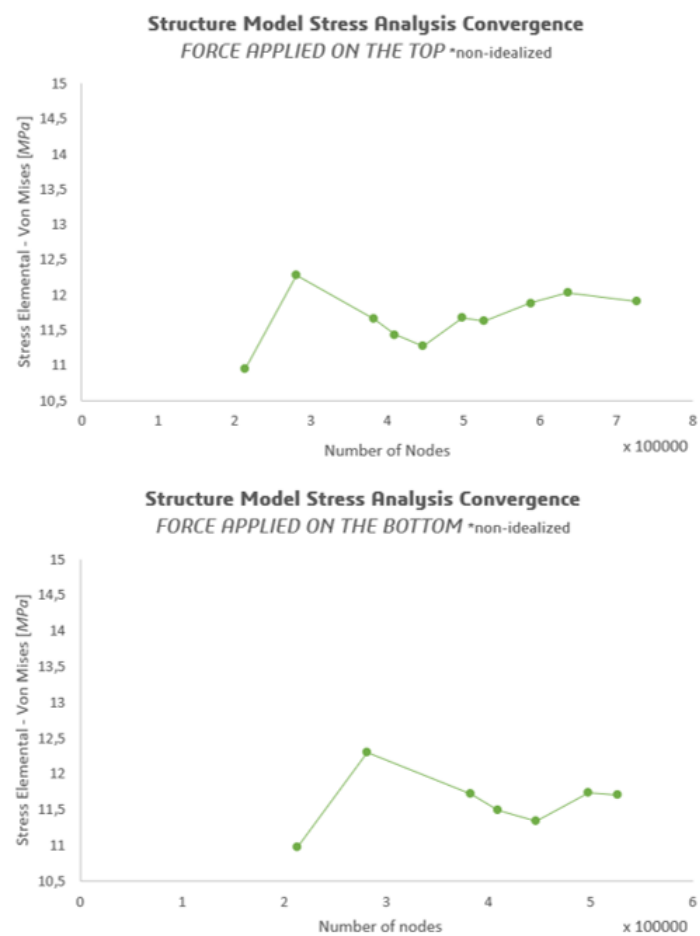
Figure 4.12: Main structure stress analysis convergence

Second FEM Model

Only a few components had their numerical mass compared to the real one. The rail-panels, side-panels, bottom-cap, top-cap and 1U brackets were already machined and could be weighted as in FEM 1. The batteries and momentum wheel mass information was provided by the suppliers so, it was possible to compare it. Regarding the PCB's, magnetorquers, air core and payload, no information was available. That way, the comparison could not be made.

To correctly replicate the mass of the batteries, two main different materials should be assigned being stainless steel for the capsule and lithium-ion for the inside material completing a mass of 0.194 kg in total (4 batteries). However, the CAD model provided by the *Mech & Thermals* team was representing the batteries as a single part. Steel was the material used for the total volume of the batteries and its density was changed from 7830 kg/m^3 to 2919.16 kg/m^3 in order to meet the mass requirement. This introduces a level of uncertainty in the model since a steel material with much less density is being used with all the usual properties of a normal steel.

The mass of the front sphere part was also affected since it was made of shell elements and, for the magnetorquer support with increased length, the mass was also higher than it would be in reality.

By applying the same boundary conditions and following the same procedure as in FEM 1, the convergence for the fundamental frequency was obtained (Fig. 4.13). The values for the model with fixed bases were always between [430-434] Hz and for the case where the rails were fixed were between [454-455] Hz. An approximation of the results in this model for both boundary conditions is also verified.

A non-idealized model in this finite element model was not used due to the longer simulation time.

Third FEM Model

Between the solar cells, solar panels and boards, only the first ones had information provided by the supplier. As the mass requirement was already fulfilled, the material density composing the solar cells remained the same. The solar panels and boards, could not be weighted experimentally and there was no information available so, no modifications were done.

Although the fundamental frequency can increase with the presence of higher tensions, it was expected that, with a higher mass, this model would show a lower fundamental frequency. Initially, the results for the FEM 3 showed a fundamental frequency higher than the previous model. As a consequence, hundreds of hours of simulations were needed to solve this problem as its cause could have been on the mesh, on the uncertainty of the materials used or in the surface-to-surface contacts assigned. From FEM 2 to FEM 3, the only components added to the model were the boards, solar panels and solar cells so, these were the first to be questioned. All the surfaces were glued and screws deleted to know the origin of the error. Another idea was to use only materials provided by *Siemens NX* to know which material was influencing the results. Then, every component, one by one, was removed from the model and the model's fundamental frequency analysed in order to know what component was affecting it. The last hypothesis was to replace the manual contacts by automatic contacts, maintaining the glue
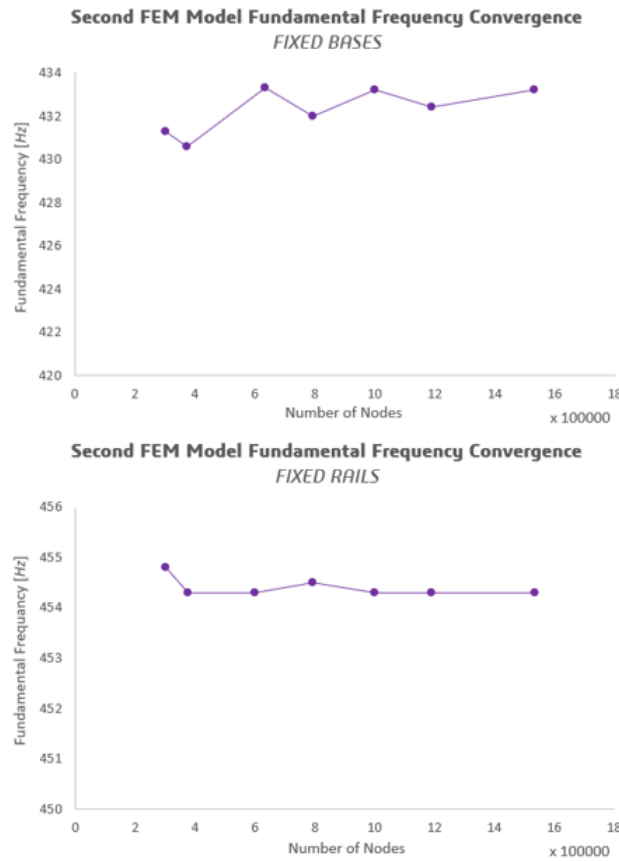
Figure 4.13: Second FEM Fundamental Frequency Convergence

constraints. After this solution, the results were finally viable to be used. In future work, it is advised the use of automatic contacts (and automatic glue).

The convergence for the fundamental frequency is presented (Fig. 4.14). The values obtained for both boundary conditions are the same which demonstrates that the rails do not have any contribution on the ORCASat's first mode of vibration. The data does not fully converge but, since meshes with element sizes below 1.5 mm increase the number of nodes exponentially, after 1 400 000 nodes, the simulation time was too long. Due to computational resources limitations further mesh refinement was not viable.

Numerically, it can be proven that the satellite fills the requirement of having a frequency above 90 Hz as the values are always between [246-249] Hz. It can also be concluded that the structure is very stiff. Similar to FEM 2, no comparison with a non-idealized model was performed.

4.1.3 Summary results and conclusions

The table 4.11 shows the fundamental frequency for each model as well as the correspondent number of the nodes. The selected values were based on the convergence study presented previously. The modes of vibration don't provide information about the amplitude of vibration [1], the shown deformation was chosen for an easy visualization of each mode (Fig. 4.15, 4.16 and 4.17).
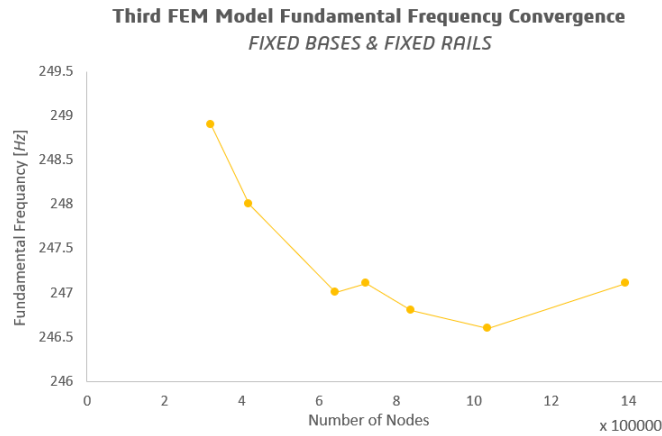
Figure 4.14: Third FEM Fundamental Frequency Convergence

Table 4.11: Fundamental Frequency of each Finite Element Model

	Fixed Bases		Fixed Rails	
	Frequency [Hz]	Number of Nodes	Frequency [Hz]	Number of Nodes
FEM 1	728.1	557 996	1297	292 342
FEM 2	433.3	633 968	454.3	633 968
FEM 3	246.8	839 325	246.8	839 325
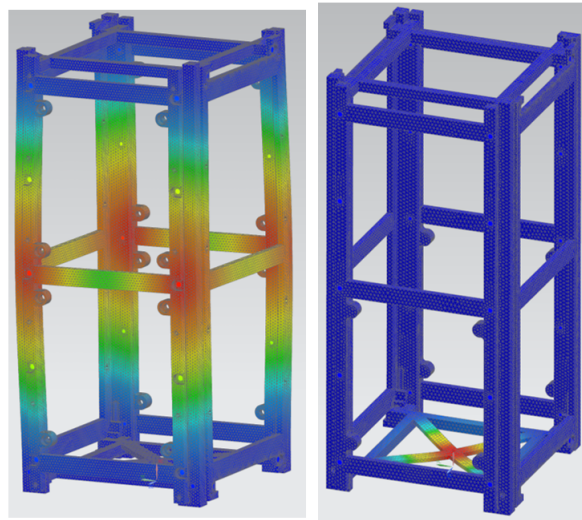
Figure 4.15: FEM 1 Results. Fixed bases (left) and fixed rails (right).

As the model becomes more complex, more components are added, which increases its mass. The frequency would decrease with an increased mass and, after solving the obstacles mentioned previously, that happens.

Due to errors, simplifications and assumptions associated to the modelling process, this result cannot be considered as proof that the satellite's fundamental frequency is, actually, 246.8 Hz. Besides, the electrical components and laser diode parts were removed from the model which would increase its mass even more and decrease the fundamental frequency. Nonetheless, the value is 273% higher than the required so, it can be predicted that the ORCASat's frequency will be above 90 Hz.
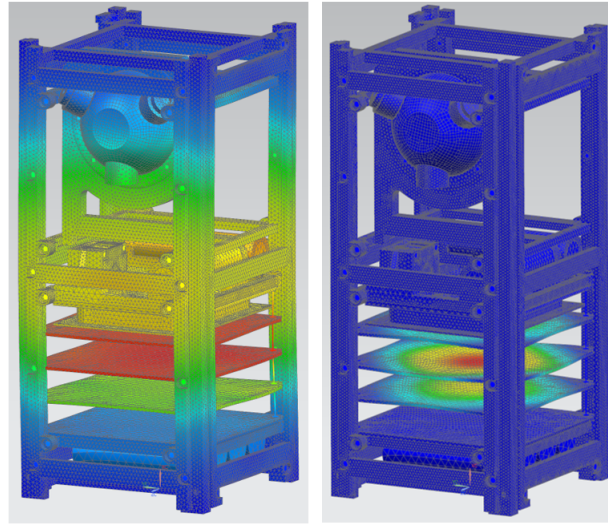
Figure 4.16: FEM 2 Results. Fixed bases (left) and fixed rails (right).
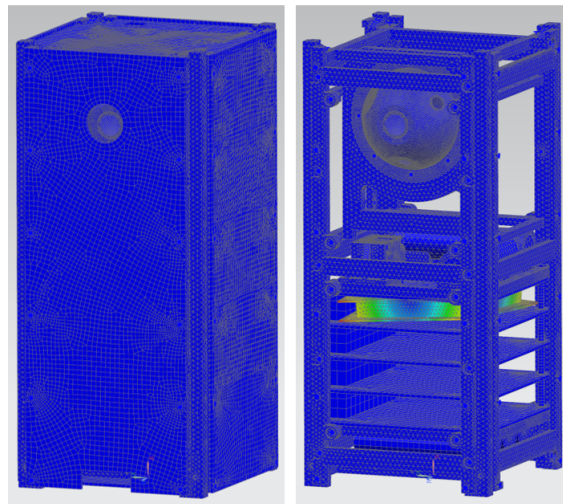
Figure 4.17: FEM 3 Results. Both boundary conditions had the same behaviour.

To have a validation of the numerical results or to improve the accuracy of the computational models, an experimental test must be done.

4.2 Experimental Modal Analysis (EMA)

4.2.1 Vibration Test Performed at UVic

The system is the ORCASat's outer structure composed by two rail-panels, two side-panels, one top-cap and one bottom-cap purely made of aluminum 6061 with stainless steel screws. The whole satellite could not be tested since these were the only components available and machined.

The shaker is basically a small cylinder with a small protrusion on top with a M8 hole. The author visited the lab before performing the test and it was concluded that, given the shaker characteristics, the satellite could not be attached to it without damaging its structure unless a plate was used to connect

the satellite and shaker (Fig. 4.18).
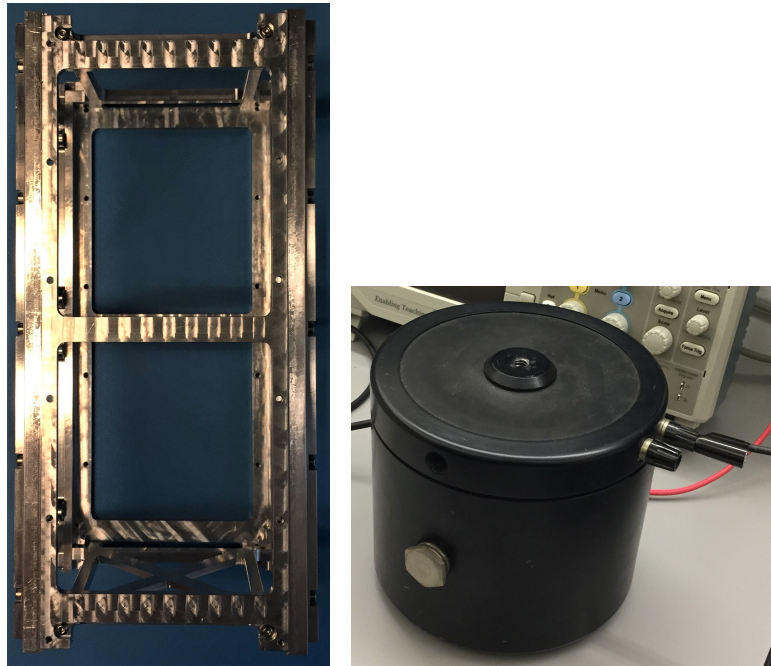
Figure 4.18: ORCASat's outer structure (left) and shaker (right)

After the support from the University of Victoria machine shop, the plate presented the dimensions of 101.6×101.6 mm, a mass of 171.4 g and 5 holes. The holes in the four corners are used to attach the ORCASat to the plate and the big centre hole is used to fix the plate to the shaker. It is important to highlight that the plate was heavy compared to the whole structure. The *Siemens NX* finite element model was adapted to these conditions as well.

Finite Element Model

By adding an extra part (and extra mass) to the system, the modes of the plate should be well separated from the structural modes to avoid the pollution of these latter modes. In order to approximate the numerical model with the real one, the idealization process was not considered and the density of the aluminium 6061 was increased since the real model had 599.4 g (Fig. 4.19) and the numerical model had 581.22 g. This difference relies on the fact that the real model included 32 screws while the numerical model had none because *surface-to-surface glue* was chosen for all the surfaces to avoid simulation errors related to the modal frequency calculation. The initial density was 2711 kg/m^3 and the final density 2796 kg/m^3. To replicate the real boundary conditions on *NX*, the plate was fixed.

Experimental Test: Procedure

On the day the experimental test was performed, more problems appeared.

- The plate was expected to be attached on the structure's bottom-cap however, the logistic of assembling everything to the shaker was impossible because of the bottom cap "X" beams. The structure
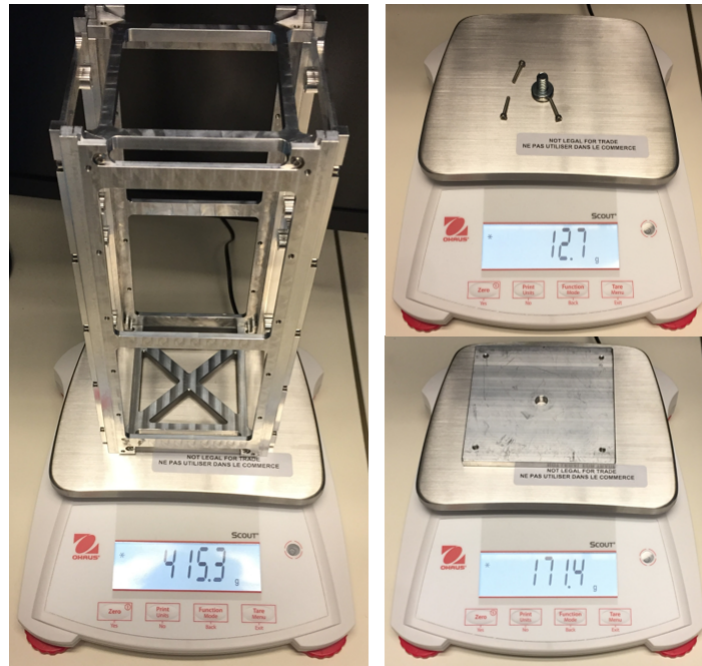
Figure 4.19: Mass of the components used during the vibration test

had to be analysed upside down and the plate was fixed on the top-cap (Fig. 4.20). The simulations on *Siemens NX* were also performed considering this option;

- The number of small screws to attach the plate to the structure was not enough as only 3 were available instead of 4. Although small, these bolts needed to be extremely long due to the gap between the plate and the structure. There were two solutions for this problem - the system could be analysed with 3 screws or the structure could be attached to the plate using wax. After discussing with one of the lab testers, it was concluded that the first option would be better since the wax would not be strong enough to keep the structure attached to the plate during the vibration test;

- The accelerometers measure the acceleration in the normal direction to the surface they are located. The team was advised to be extremely careful with the only accelerometer available otherwise its interior components could be damaged and the values read would not be accurate. While the lab tester was explaining how to attach the accelerometer, which is done by using wax (Fig. 4.21 (**1**)), the instrument was dropped. It is unlikely that the accelerometer was damaged due to the small altitude the falling occur, but it should be highlighted since it could influence the data obtained during the experimental test.

Five instruments were used to perform the test (Fig. 4.21): shaker (**2**), oscilloscope (**3**), accelerometer (**4**), function generator (**5**) and amplifier (**6**).

The team was told where to place the accelerometer in order to determine the system modal frequencies. By using the numerical modal analysis and visualizing the mode shapes, the area where the structure showed a bigger displacement should be the location to attach this instrument. Thus, the accelerometer was placed on the rail-panel and side-panel corners to read the accelerations on the Y and Z directions respectively, since the first five modal frequencies and mode shapes were not axial modes but bending modes.
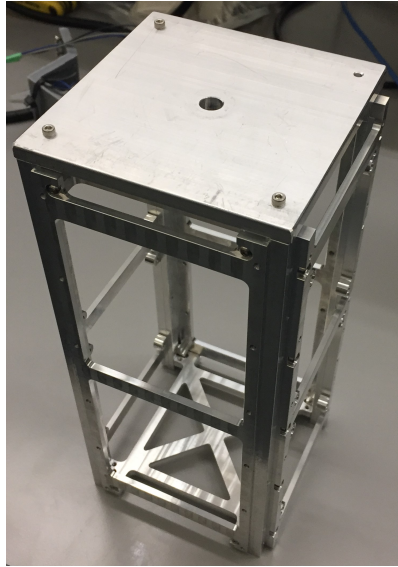
Figure 4.20: System tested
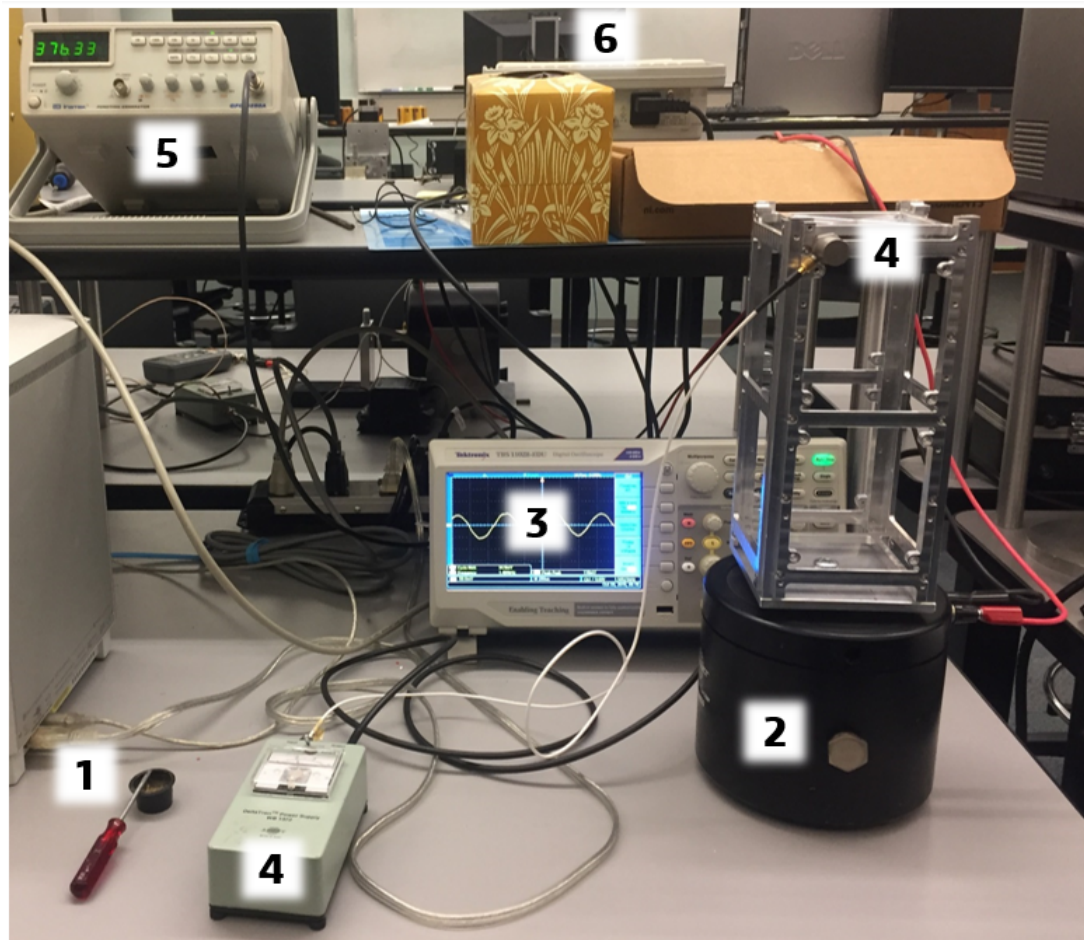
Figure 4.21: Setup

The procedure was based on starting at a low frequency (for example, 75 Hz) and increasing it slowly. When the graphics on the oscilloscope started giving higher response i.e. the response amplitude increased due to resonance, that should be identified as a modal frequency.

Experimental Test: Results

The following frequencies were obtained:

Side-panel accelerometer [Hz] 167.20 / 215.07 / 301.18 / 376.60 / 502.92

Rail-panel accelerometer [Hz] 485.22 / 590.01 / 1020.5

The fundamental frequency is 167.20 Hz. Comparing to the fundamental frequency given by *Siemens NX*, 218.1 Hz, an error of 30.4% is revealed (Fig. 4.22).

This error can be a consequence of everything mentioned above but also because of the subjectivity while detecting the modal frequencies. Another analysis was performed at the NRC installations by specialists and the discussion can be found in the next section.
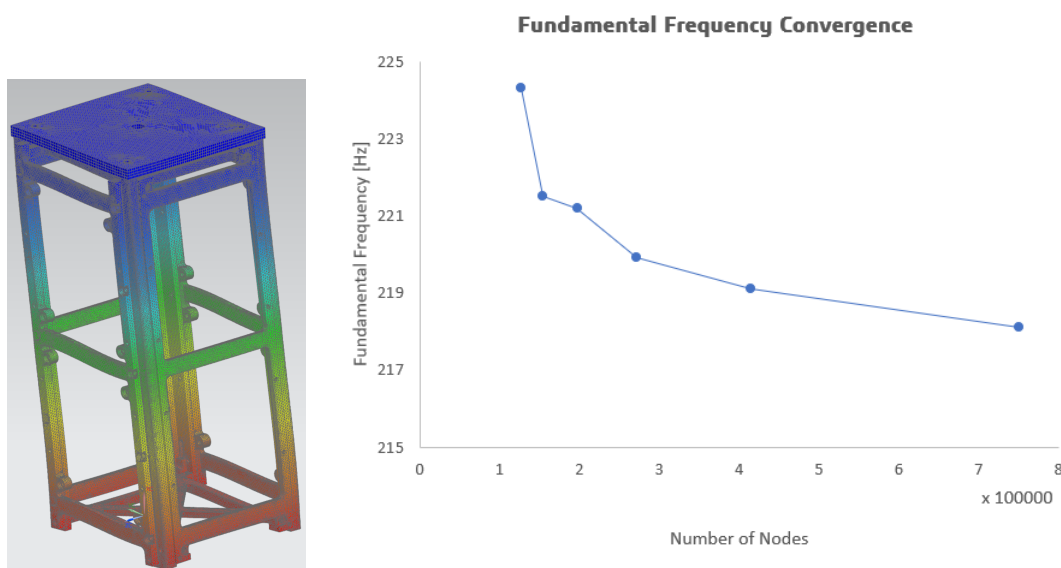
Figure 4.22: Fundamental frequency's mode shape (left) and fundamental frequency convergence study (right)

4.2.2 Vibration Test Performed at NRC

This experimental vibration test was performed at the National Research Council (NRC), in Ottawa. The system tested was composed by the ORCASat's outer structure - two rail-panels, two side-panels, one top-cap and one bottom-cap.

In September the team reunited with some NRC representatives and, in order to obtain the results before the end of October, it was initially established that a free-free vibration test (no loads being applied and no constraints) would probably be the best option. Nevertheless, due to the structural symmetry of the system and its structural complexity, there would be some challenges to perform an effective modal test for some modes. Throughout that month, the best and easiest way to perform the test was discussed.

Two preliminary numerical models were analyzed being one submitted to a free vibration analysis

(fixed at the bottom) and another to a free-free vibration analysis. It was observed that the first 10 modes ranged between 260 and 1600 Hz for the free vibration case and the first 17 modal frequencies ranged between 480 and 1950 Hz for the free-free vibration. After sending these preliminary results to NRC, it was concluded that both cases would require a similar input excitation energy of, at least, 2 kHz. A load hammer with a stiff head for excitation input would be used for the free-free vibration test and a modal shaker for the same excitation would be used for the free vibration test. From the setup implementation point of view, the free vibration test would require the system to be fixed on a larger base structure, similar to the vibration test performed at UVic and the free-free vibration test would require the structure to be hanged using a flexible bungee cord, to ensure that rigid body modes would be well separated from the structural modes, which is a relatively simpler setup.

The number of modes to be identified was also a discussed parameter. First, the frequency range must be known since more modes require more sensor channels to enable effective separation and identification of the target modes. Second, the existence of any axial modes besides bending modes must be verified. If there are any axial modes, the accelerations in all directions should be measured after the excitation. If there are only bending modes, the accelerations in Y and Z are the ones of interest to be measured after the excitation.

Considering the preliminary free-free vibration analysis on *Siemens NX*, it was observed that the modes 12 to 17 had localized beam bending modes (at around 1000 Hz) in the mid height of the structure, which would require extra sensors to be attached to the center of these four mid height beams. These modal shapes would greatly increase the setup complexity.

Having a very similar structure in Y and Z directions can also complicate the task due to the existence of "closely related modes". In order to differentiate these modes, multiple shaker inputs with uncorrelated input energy simultaneously would be needed otherwise they can be mixed and possibly mistakenly identified. In the preliminary free-free vibration analysis, modes 12 to 15 were "closely coupled modes".

As predicted during the meeting and regarding all the statements above, it was suggested a free-free vibration test and the use of an excitation hammer to identify the structure lower and first few modes. Due to its quasi-symmetric nature and complex design, it would be challenging to accurately identify modes above 1 kHz for this structure.

Besides determining the modal frequencies, NRC wanted to characterize the modal shapes on the targeted modes more reliably. As explained to the team, without the modal shape information it is difficult to correlate the experimental and numerical results especially when there is a mismatch between them. To enable a reliable correlation, more information at more modes is required being a similar situation as defining a very coarse mesh for the modeled structure. Twelve accelerometers were used to perform this test.

Finite Element Model

Before sending the structure to NRC, the numerical model was updated and a convergence analysis performed.

One of the characteristics changed was the density of the aluminum 6061 since the mass of the numerical model was 404.971 g and the mass of the real model was 415.2 g. As NRC was planning to use 12 accelerometers, these would affect the final mass of the system as well. Knowing that the accelerometers used were PCB 356A01 with 1 g each [62], the real model would weight 427.2 g. Regarding the cables attached to the accelerometers, their weight was off-loaded by the wire responsible for supporting the structure during the test. The initial density was changed from 2711 kg/m^3 to 2859.81 kg/m^3 being the mass of the accelerometers dissipated by the whole model which could increase the error between the theoretical and experimental tests.

The finite element model is equivalent to the non-idealized FEM 1 with all the surfaces glued. The modal frequencies (Table 4.12) and convergence study (Fig. 4.23) obtained from mode 7 to 15 are presented.

Table 4.12: Modal frequencies in the numerical model

Number of Nodes	723 010	400 167	262 288	192 583	149 843	123 501
Mode 1	470.8	471.5	472.1	472.5	473.6	474.4
Mode 2	567.5	568.7	569.9	570.9	572.6	576.1
Mode 3	722.1	724	726.1	727.3	729.9	737.7
Mode 4	813.2	813.9	814.8	815.2	816.1	816.5
Mode 5	905.4	906.2	907.5	908.6	910.4	912.6
Mode 6	1025	1026	1027	1028	1030	1033
Mode 7	1201	1204	1207	1211	1216	1220
Mode 8	1225	1227	1229	1231	1234	1239
Mode 9	1273	1275	1277	1279	1282	1284
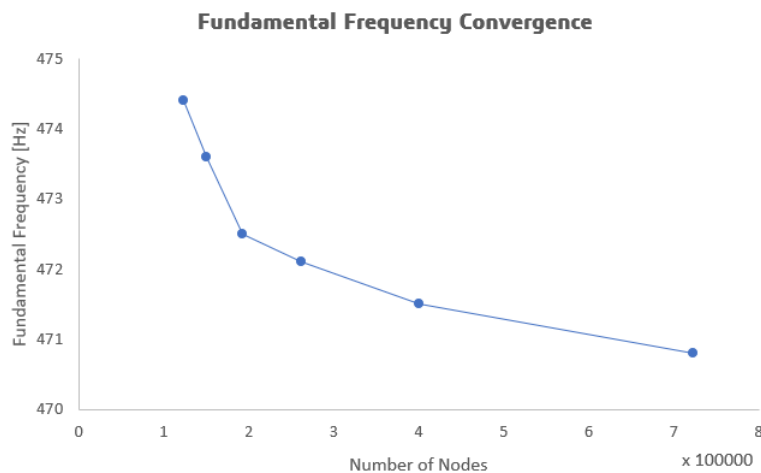
Figure 4.23: Fundamental frequency convergence study

Experimental Test: Procedure

The structure was sent to NRC, the free-free vibration test was performed and the required structural modes were successfully extracted. Procedures included:

- The system was suspended using four thin wires attached to the four corners of the frame (**1**) and a bungee cord which was connected to a firm supporting structure (**2**) (Fig. 4.24);

51
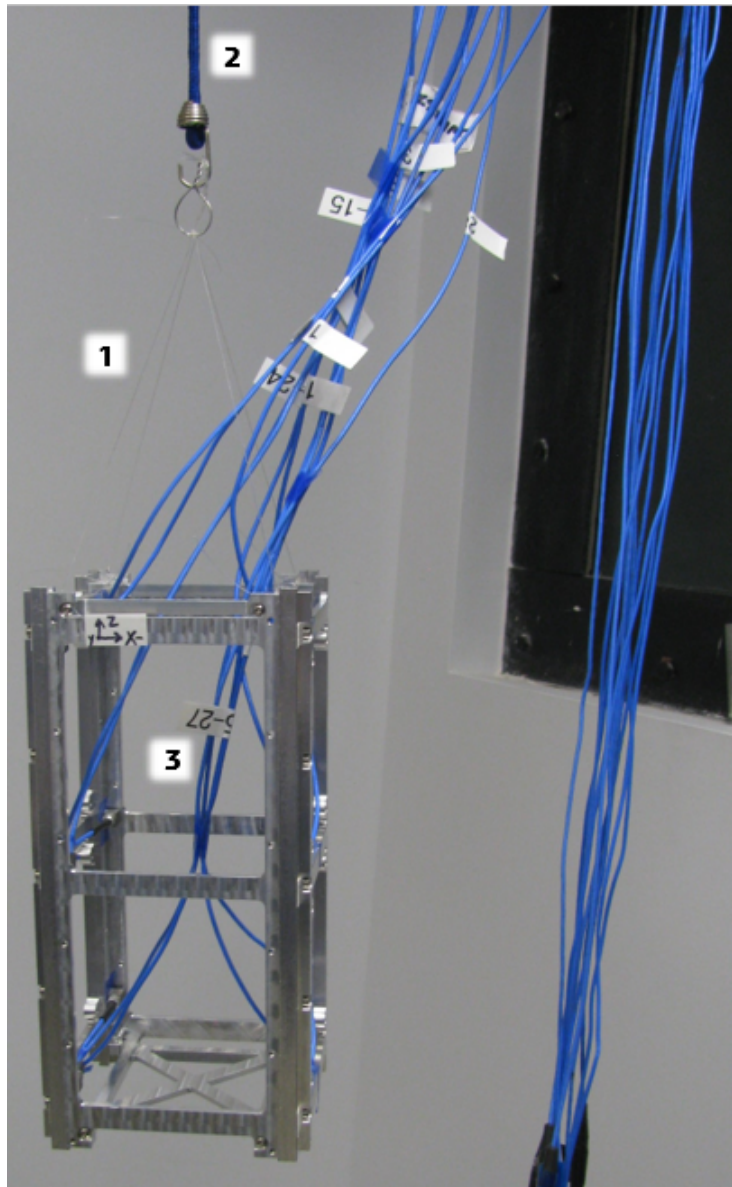
Figure 4.24: Setup

- 12 tri-axial accelerometers were attached to the top, mid and bottom of the structure (**3**);

- An impact hammer with embedded load cell was used to excite the structure (Fig. 4.25). The energy was analysed and confirmed to cover the target frequency range up to above 2 kHz. Two datasets were measured, one with the hammer at the top corner (**left**) and the other with the hammer at the bottom corner (**right**);

- POLYMAX Modal Analysis method was performed, and the frequency range was focused between 10 and 1600 Hz for each dataset. All target modes were identified clearly in each dataset;

- Comparing the modal data results from both datasets, all the major modes were identified with consistency, and correlated well;

- Operational modal analysis was also performed on one dataset and also confirmed the consistency in the identified modes;
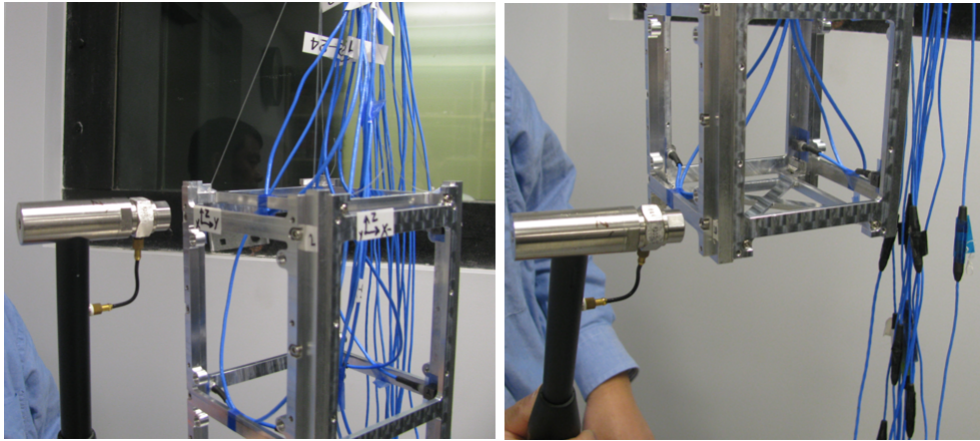
Figure 4.25: Impact hammer

Besides this information, NRC sent more documents including Auto MAC and MAC validation between two separate datasets, FRF quality check and modal synthesis. Animations of the modal shapes were also sent.

Experimental Test: Results

The modal frequencies obtained by NRC are shown (Table 4.13).

Table 4.13: Error between the modal frequencies obtained numerically via *NX Nastran* and experimentally by NRC

Mode	NX Nastran Results [Hz]	NRC Results [Hz]	Error [%]
1	470.8	459	2.57
2	567.5	527	7.68
3	722.1	672	7.46
4	813.2	799	1.78
5	905.4	861	5.16
6	1025	990	3.54
7	1201	1155	3.98
8	1225	1222	0.24
9	1273	1347	5.49

The Modal Assurance Criterion Analysis (MAC) is used to determine the similarity of two mode shapes. If the mode shapes are identical i.e. all points move the same or if a linear relation exists between the two complex vectors, the MAC will have a value of one or 100%. If the mode shapes are very different or linearly independent, the MAC value will be small, close to zero. If a mode shape is compared to itself, the Modal Assurance Criterion value should be one or 100%, observed in the Fig. 4.26, extracted from the AUTO MAC results.

Although the provided table was cut, it is noticeable that the diagonal of the matrix is 100% and the other elements are always below 1% except in the case of the mode 1 and 3 where, approximately, 3% was obtained.

Regarding the MAC results (Fig. 4.27) where the values differ on the hammer's impact location (top or bottom) it is observed that the matrix diagonal is not exactly 100% but is always around 99% except for

Auto Modal Assurance Criterion (%)								List Options	Table
	Mode No	Frequenc	Mode 1 459.346	Mode 2 527.040	Mode 3 672.177	Mode 4 798.837	Mode 5 861.080	Mode 6 990.352	
1	Mode 1	459.346	100.000	0.138	3.027	0.010	0.006	0.006	
2	Mode 2	527.040	0.138	100.000	0.167	0.001	0.052	0.009	
3	Mode 3	672.177	3.027	0.167	100.000	0.020	0.001	0.055	
4	Mode 4	798.837	0.010	0.001	0.020	100.000	0.012	0.068	
5	Mode 5	861.080	0.006	0.052	0.001	0.012	100.000	0.066	
6	Mode 6	990.352	0.006	0.009	0.055	0.068	0.066	100.000	
7	Mode 7	1154.574	0.022	0.030	0.131	0.003	0.110	0.025	
8	Mode 8	1222.032	0.014	0.341	0.008	0.174	0.038	0.006	
9	Mode 9	1347.201	0.383	0.183	0.653	0.345	0.950	0.415	

Figure 4.26: AUTO MAC results matrix

mode 1 where the value was, approximately, 96%. All the other elements of the matrix present a value below 1% except for the mode 1 and 3 that, as in the AUTO MAC, have a value of, approximately, 3%. It can be concluded that the location of the hammer will not affect the obtained data. Theoretically, the extracted modes should not be affected by the location of the hammer's impact however, the direction of the impact load can cause variation in the results.

Modal Assurance Criterion (%) between processings A and B								List Options	Table
	Mode No	Frequency	Mode (A) 1 459.346 Hz	Mode (A) 2 527.040 Hz	Mode (A) 3 672.177 Hz	Mode (A) 4 798.837 Hz	Mode (A) 5 861.080 Hz	Mode (A) 6 990.352 Hz	
1	Mode (B) 1	458.401 Hz	95.949	0.001	0.017	0.001	0.015	0.004	
2	Mode (B) 2	526.840 Hz	0.354	99.369	0.084	0.001	0.073	0.008	
3	Mode (B) 3	664.587 Hz	3.723	0.075	99.149	0.047	0.037	0.020	
4	Mode (B) 4	798.216 Hz	0.134	0.123	0.092	99.393	0.081	0.082	
5	Mode (B) 5	859.974 Hz	0.051	0.029	0.076	0.032	99.664	0.125	
6	Mode (B) 6	990.564 Hz	0.026	0.005	0.097	0.051	0.117	99.905	
7	Mode (B) 7	1155.967 Hz	0.022	0.017	0.232	0.000	0.184	0.041	
8	Mode (B) 8	1219.748 Hz	0.344	0.795	0.062	0.239	0.081	0.506	
9	Mode (B) 9	1343.096 Hz	0.117	0.018	0.655	0.374	1.084	1.628	

Figure 4.27: MAC results matrix

Modal Synthesis serves to compare the measured FRF's with the synthesized FRF's using the extracted modes within the frequency of interest. If no error exists, an 100% match should be obtained for all directions and locations. The results on figures 4.28, 4.29 and 4.30 are for a specific selected location. NRC stated that similar correlations for other locations were obtained.

PCA stands for Principal Component Analysis. FRF-Coherence and PCA were provided to show the quality check of the obtained FRFs in the experiments. By visualizing the FRF-Coherence results, it is possible to detect the modal frequencies easily as they are well defined and are given by the peaks presented on the FRF. As the author was told by NRC, unexpectedly, the outer structure was a "simple and clean" system which facilitated the distinction of modal frequencies as they were presented as quite out of phase peaks and well damped. Usually, in more complex systems, the different peaks can be very close making the detection and distinction of the modal frequencies a complicated process.

Regarding the coherence diagram, it helps to evaluate if the amplitude of the FRF is close of being correct. According to [63], coherence is a function versus frequency that indicates how much of the output is due to the input in the FRF. It can be an indicator of the quality of the FRF. The value of a coherence function ranges between 0 and 1. A value of 1 at a particular frequency indicates that the FRF amplitude and phase are repeatable from measurement to measurement. A value of 0 indicates the opposite, which means that possibly there is an error in the measurement setup. If only one mea-
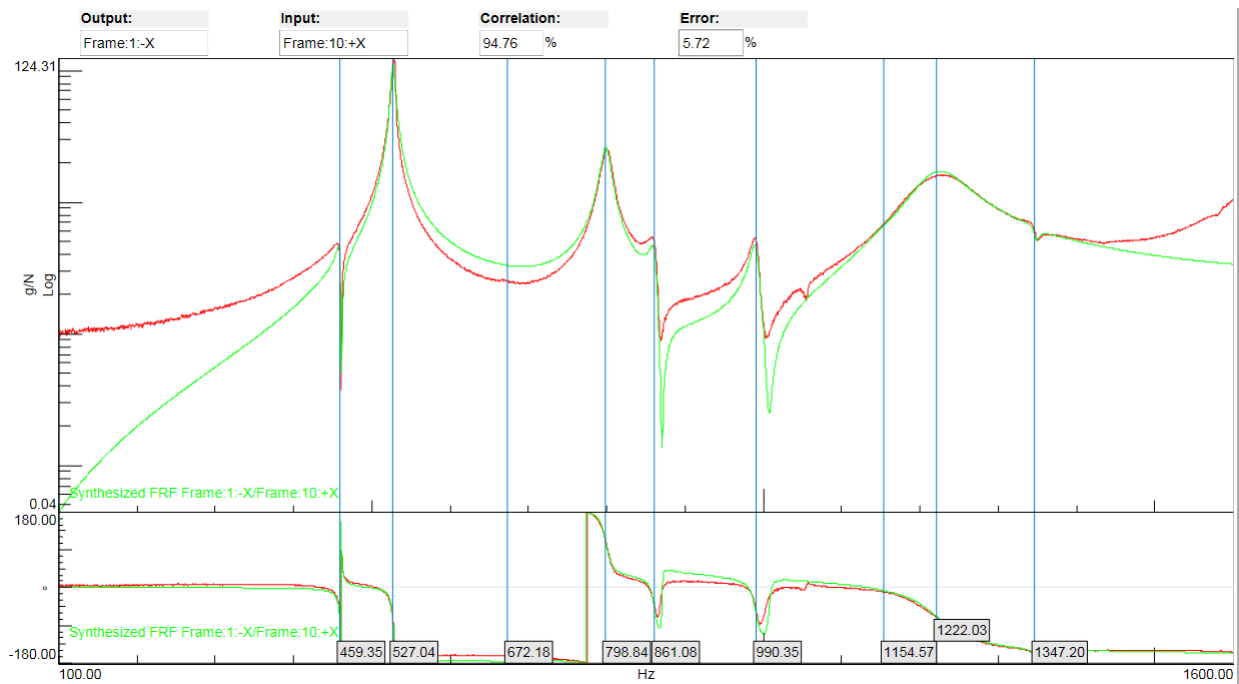
Figure 4.28: Modal synthesis (X direction)
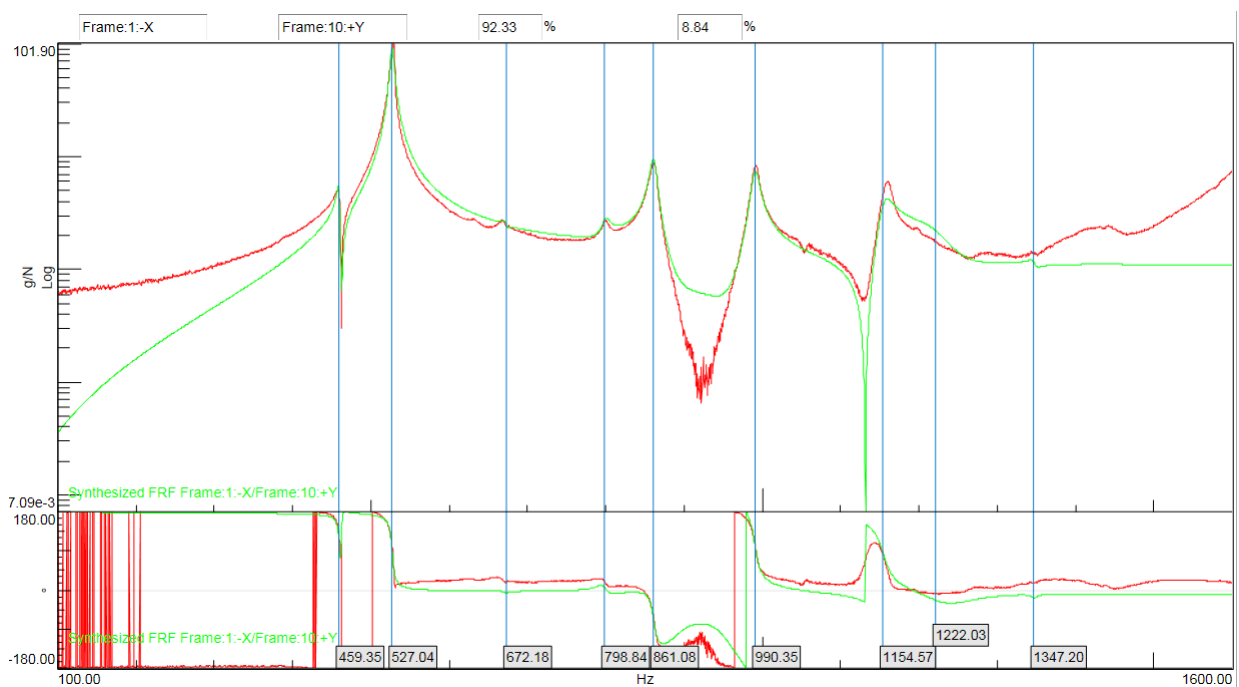
Figure 4.29: Modal synthesis (Y direction)

surement is performed, the value will be 1 across the entire frequency range giving the appearance of a perfect measurement. At least two FRF measurements need to be taken and compared to compute a meaningful coherence function [64].

It is possible to observe the location of the modal frequencies as well as the coherence obtained for that Frequency Response Function in Fig. 4.35.
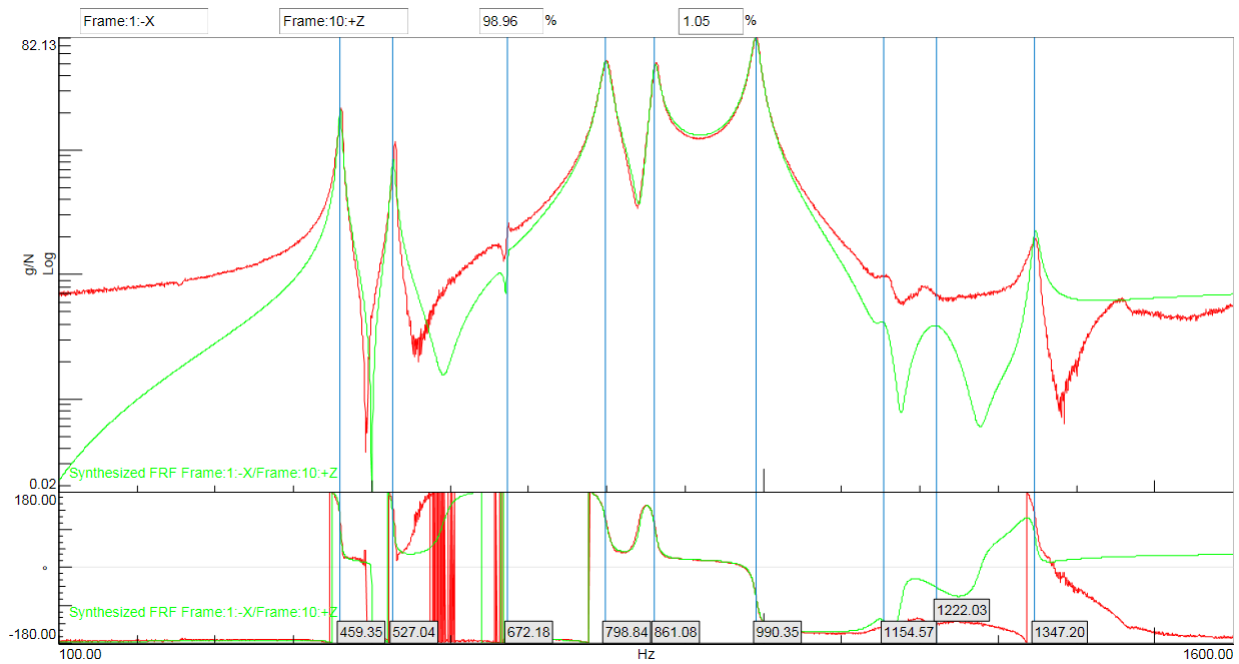
Figure 4.30: Modal synthesis (Z direction)

Conclusions

In addition to the error induced by the inconsistent excitation, another limitation to obtain correct data are the sensors locations. Since the outer surfaces of the structure are not flat, NRC attached the accelerometers on the interior surfaces. Due to the limited space and cross beams, the sensors locations were not perfectly aligned to the intended node locations, which would affect the results to some extent. The sensor orientation during the setup is another common source for errors during the test [63].

Despite all the approximations and induced errors that could appear during the real and simulated tests, by comparing the first nine modal frequencies (Table 4.13), the error is always below 8%. In fact, for the fundamental frequency, the error is, approximately, 2.6% which validates the numerical model for future analysis.

By having this validation, the characteristics applied to the outer structure in the numerical model should be added in the following more complex models as well. As this experimental test was the final step of this thesis and the last data being received, this structure was not applied to the second or third finite element models described in the beginning of this chapter. However, for the succeeding studies related to vibration analysis done by the ORCASat team, this should be the starting point for a good model and good results.

Regarding the optimization, considering the parameters that needed to be changed, the number of elements present in the model and the simulation time, a complex optimization would take, at least, one month to be completed. The team was advised to do an improvement where the mass of the model or

56

the Young modulus could be changed in order to decrease the error. As the mass of the numerical model had already been changed before sending the structure to the NRC, no modifications were applied.

4.2.3   Vibration Test Performed at NRC (Homathko)

This section is simply for comparison between the results regarding the third finite element model and the experimental ones obtained for the satellite Homathko at the National Research Council on July, 2018. This experimental test is explained in [10] so, only a brief discussion is presented. It is relevant because it is the only experimental test covering a complete model.

Homathko is a 3U CubeSat, born in the Canadian Satellite Design Challenge (CSDC) competition with a payload similar to ORCASat. In fact, the integrating sphere used on FEM 2 and FEM 3 is the same as the one used in this experimental test.

The experimental test consisted in three different phases - a sine sweep test from 5 Hz to 2200 Hz to identify the resonance frequency; a random vibration test to simulate the launch conditions and; another sine sweep to verify any resonance frequency changes. If these changes are detected, it means that a failure in a component occurred or a satellite's connection was broken. During the Homathko's vibration test, there were some changes in the resonance frequency decreasing in the second sine sweep. This happened because some screws and connectors were lost, which reduced the stiffness of the structure, increased the damping and, that way, the frequency was decreased.

The accelerometers were placed in specific points on the satellite and the fundamental frequency was detected with a value of 130.1 Hz. Comparing with the fundamental frequency obtained for the third FEM model (246.8 Hz), it was expected that the ORCASat's frequency would be higher than the Homathko's since the latter is heavier. Homathko (3U) satisfies the requirement regarding the minimum frequency. It is reasonable to predict that a complete ORCASat (2U) will also satisfy it since both were built with the same requirements and similar features on the structural level.

4.3   Preliminary Design Review - Finite Element Analysis

During the development of this thesis, the CAD model was undergoing changes by the *Mech & Thermals* team. The model presented during the Preliminary Design Review presentation, in the end of October, had some different features from the CAD model used during the numerical vibration analysis.

Since the thermal analysis (chapter 5) was completed and the author was waiting for the NRC experimental results, a vibration analysis was performed for the PDR model as well. The main purpose was to verify if the ORCASat's fundamental frequency remained above 90 Hz. This time, no component was removed from the model and the idealization process was considered due to its complexity.

4.3.1 PDR CAD model

The PDR model is an update from FEM 3, some components were added and features changed. These are described (Fig. 4.31 and 4.32).

- Solar cells considered as 3D surfaces;

- Inclusion of four solar sensors (**1**) on the $\pm$Y and $\pm$X faces;

- Inclusion of the Remove Before Flight pin (**2**);

- Inclusion of an electrical ground support equipment (EGSE) (**3**) connector on the $-$X face;

- Inclusion of an antenna deployer mechanism (**4**) attached to the TT&C PCB;

- The magnetorquer supports were kept as is. No dimension was changed and screws represented as cylinders (same adaptation for the PCB stack) (**5**) were used to attach them to the ADCS PCB;

- The boards are divided in three main electrical components being the main backplane PCB (**6**) and two connectors (**7**);

- Inclusion of a second payload PCB (**8**) with two aluminum parts attached to it (**9**). This PCB is connected to the ALTAIR payload by four screws represented as cylinders (**10**);

- The integrating sphere possesses two bulky components designated by heatsinks (**11**);

- The photodiode cap (**12**) and photodiode case (**13**) were not removed;

- All the small PCB's connected to the integrating sphere and antenna deployer were maintained (**14**).
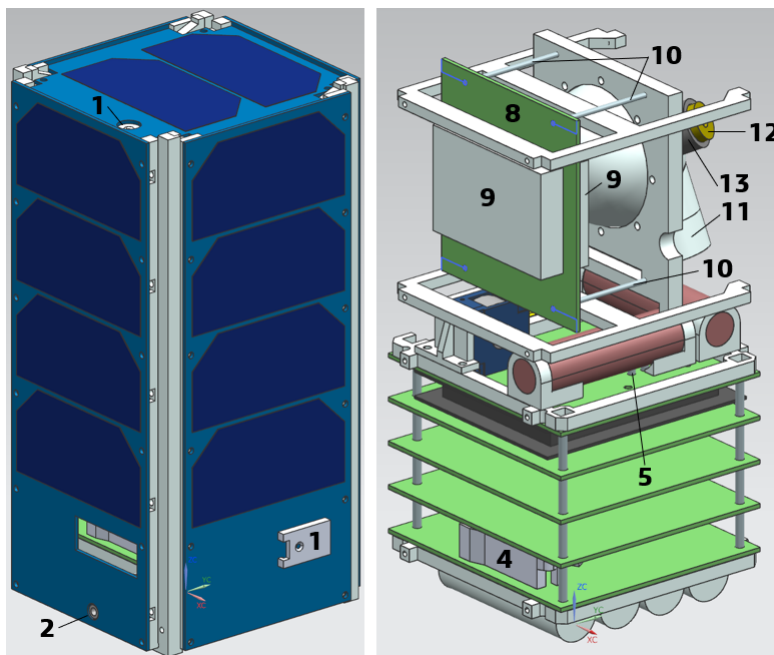
Figure 4.31: PDR CAD model description
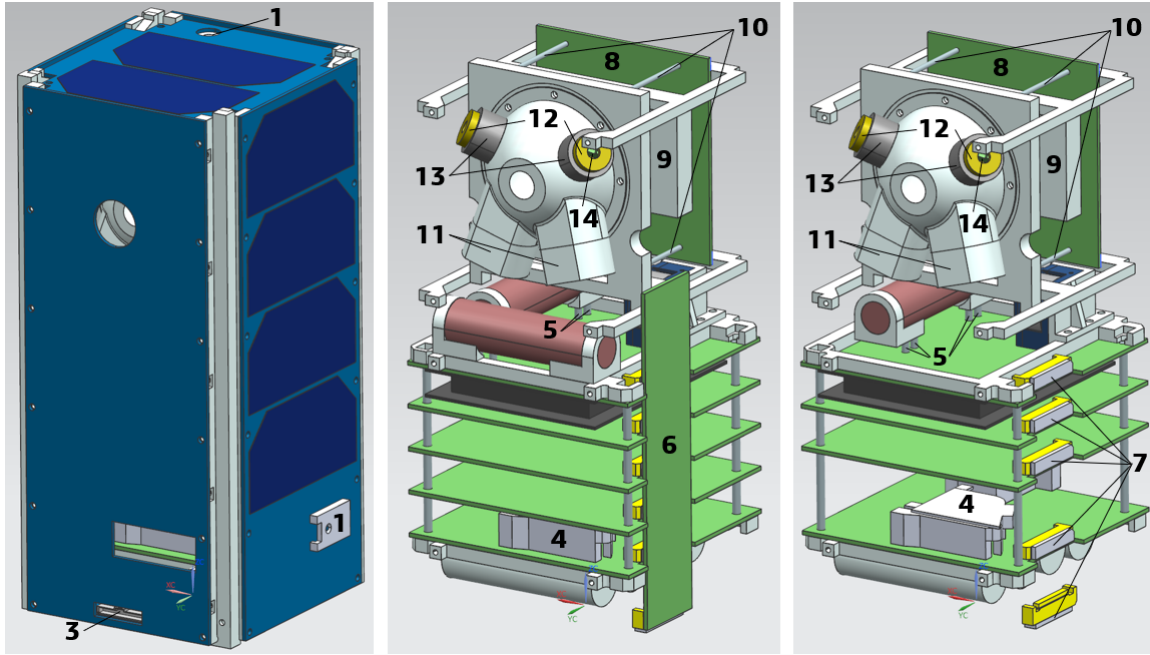
Figure 4.32: PDR CAD model description (another view)

4.3.2 PDR finite element model

Using the same procedure explained in the last sections, the mesh characteristics are presented (Table 4.14 and Fig. 4.33).
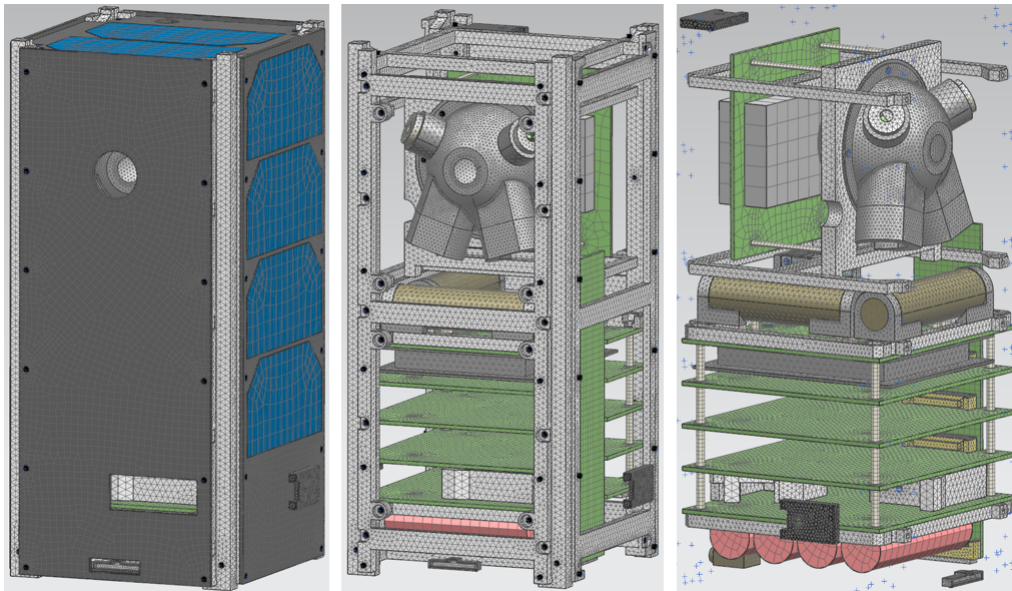
Figure 4.33: FEM PDR model

4.3.3 Analysis and Solution Development

In the *.sim* file, both *surface-to-surface contact* and *surface-to-surface gluing* were added automatically. Due to time limitation, the PDR model was analysed for the case where the bases are fixed,

Table 4.14: FEM PDR model mesh information

Component	Element Type	Material
side-panel / rail-panel / top-cap / bottom-cap / 1U brackets	CTETRA(10)	aluminum 6061
solar panels	CHEXA(8)	FR4
solar cells	CHEXA(8)	*defined previously*
solar sensors	CTETRA(10)	ABS
RBF pin	CTETRA(10)	aluminum 6061
EGSE connector	CTETRA(10)	ABS
batteries	CHEXA(8)	steel*
PCB stack	CHEXA(8)	FR4
multiple connected bolt segment [PCB / integrating sphere]	CHEXA(8)	steel
back PCB	CHEXA(8)	FR4
back PCB connectors	CTETRA(10)	ABS
antenna PCB	CHEXA(8)	FR4
antenna structure	CTETRA(10)	delrin
air-core	CTETRA(10)	delrin
magnetorquer brackets	CTETRA(10)	aluminum 6061
magnetorquers	CTETRA(10)	copper
magnetorquer screws	CHEXA(8)	steel
momentum wheel bracket	CTETRA(10)	aluminum 6061
momentum wheel [board]	CHEXA(8)	aluminum 6061
momentum wheel [front / back]	CTETRA(10)	aluminum 6061
momentum wheel [wheel]	CTETRA(10)	brass
integrating sphere [gasket / front / back]	CTETRA(10)	aluminum 6061
integrating sphere [photodiode case]	CTETRA(10)	delrin
integrating sphere [photodiode cap]	CTETRA(10)	brass
integrating sphere [all PCBs]	CHEXA(8)	FR4
integrating sphere [PCB metal boxes]	CHEXA(8)	aluminum 6061
integrating sphere [heatsink internal component]	CTETRA(10)	brass
screws	CBAR	steel
connections	RBE2	*not defined*

being the other boundary condition discarded. The obtained data for the first three modal frequencies is presented (table 4.15).

Table 4.15: Modal frequencies of the PDR model before and after applying the proposed solution

	Before	After
Number of Nodes	660	179
Mode 1 [Hz]	89.66	192.2
Mode 2 [Hz]	140.6	276.7
Mode 3 [Hz]	192.3	289.5

The ORCASat did not fill the requirement of having the fundamental frequency above 90 Hz. This was unexpected since the FEM 3 revealed a fundamental frequency above 200 Hz. Initially it was thought that the cause of this frequency could be in the mass of the model which was higher than the mass of the third finite element model however, the difference would not be enough to change the satellite's dynamic behaviour at this level. As the biggest difference between both models relies on the ALTAIR payload, by analysing the mode shapes, it was concluded that the vertical payload PCB should be attached to the respective 1U brackets.

After applying this constraint, new results were obtained revealing this solution as a success. It is observed that the fundamental frequency is now above 90 Hz being the requirement fulfilled. As the

structure became more stiffed, the first frequency was no longer characterized by a deformation on the vertical payload PCB (Fig. 4.34).

The conclusions stated in the section *Vibration Test Performed at NRC (Homathko)* are still valid for this model.
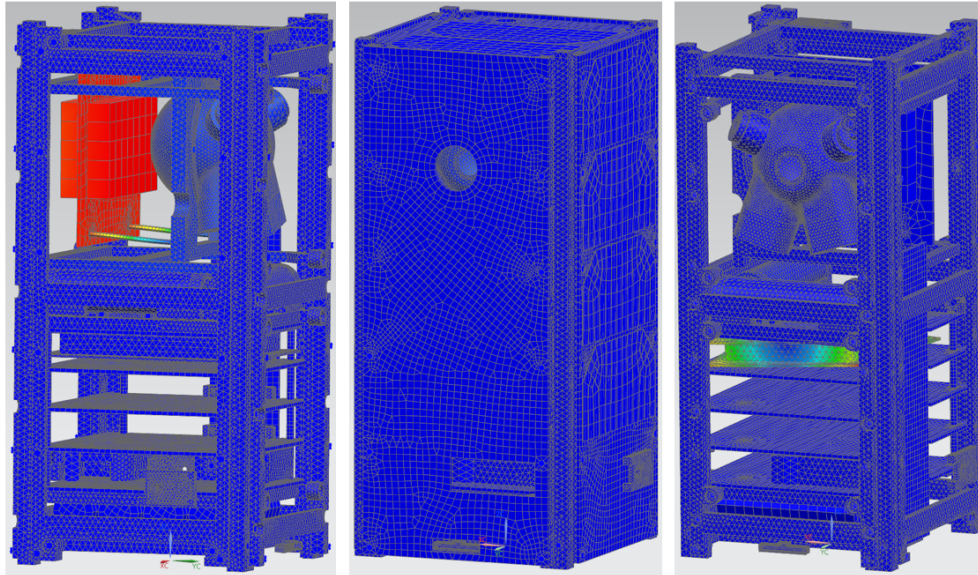
Figure 4.34: Mode shapes of the PDR model. First case (left), second case (right)
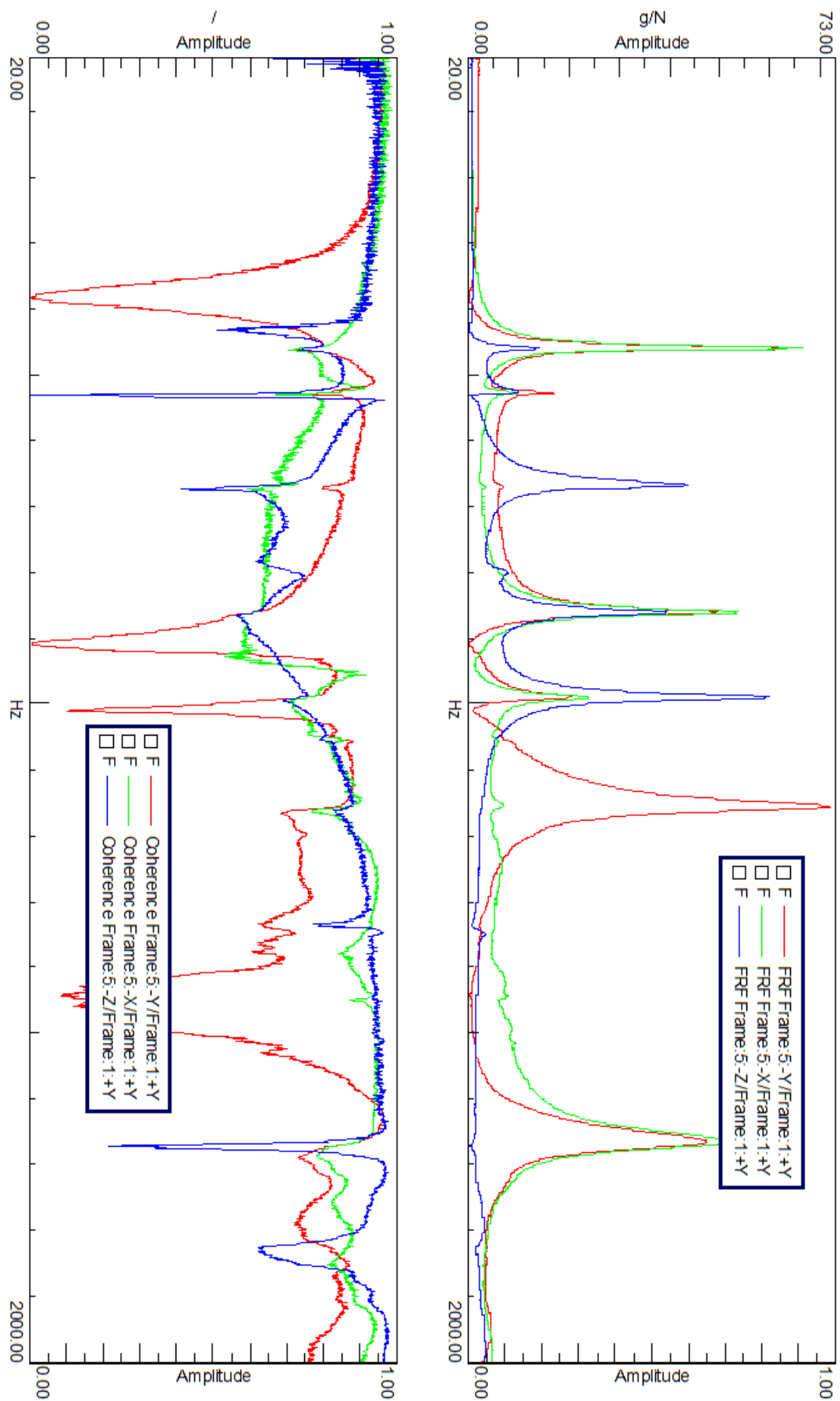
Figure 4.35: FRF and respective coherence results

Chapter 5

Thermal Analysis

CubeSats usually possess a low thermal inertia and poor heat dissipation. This can be a consequence of weight limitations that prevent the use of certain materials with better thermal properties [10]. As the power budget for these small satellites is usually very restrictive, a problem is created since, if it is necessary to apply a thermal control system, one needs to be able to monitor and regulate component temperatures for the spacecraft over the life of the mission without the use of too much power. The decision of applying a thermal control system needs to be taken seriously as it can affect all the satellite subsystems.

Thermal stresses can also be experienced if the satellite is made of different materials with different coefficients of thermal expansion. If these stresses reach values higher enough that make the components to start buckling or if it is subjected to many cycles that causes components to fail due to fatigue, the whole structure can be compromised [65] or lead to a quicker degradation of the spacecraft attitude and pointing errors.

To know the satellite's behaviour in the space environment at a specific orbit, and if its components stay between their operational range, a thermal analysis must be performed. If the results obtained reveal that the temperatures reached by the satellite's components are outside their operating temperature range or the temperature peaks and deltas need further improvement, a thermal control system should be designed or some changes should be done to the structure, respectively.

The thermal analysis was performed using the program *Siemens NX* with the solver *Space Systems Thermal*. The procedure described in the chapter 4 is the same used for this study - three documents are needed (*.prt*, *.fem* and *.sim*) and each one have its specific function.

In this study, only one model was used, identical to the third finite element model in the structural analysis.

5.1 Finite Element Analysis (FEA)

5.1.1 Idealization Process

The thermal model suffered the same idealization process as FEM 3 from the previous chapter however, all the contacts between its surfaces were assumed as perfect to reduce the complexity of the model. With the screws removed, the respective holes were also deleted to decrease the number of elements needed to define these small features.

5.1.2 Finite Element Method Model

In the *.fem* file, the different mesh types, materials and thermo-optical properties of the different surfaces are assigned to the model.

The mesh of the thermal model is constituted by 2D and 3D elements (Table 5.1). Using the knowledge acquired during the structural analysis it was possible to define this FEM in order to avoid possible errors when running the solution. 2D elements were used to model the solar cells which were represented as shell surfaces. 3D elements were used in the rest of the satellite's components.

The mesh characteristics are presented (Fig. 5.1).

Table 5.1: Mesh characteristics of the thermal model

Component	Element Type	Material	Thickness [*mm*]
side-panel / rail-panel / top-cap / bottom-cap / 1U brackets	TET4	aluminum 6061	-
batteries	HEXA8	steel*	-
PCB	TET4	FR4	-
air-core	TET4	delrin	-
magnetorquer brackets	TET4	aluminum 6061	-
magnetorquers	TET4	copper	-
momentum wheel [bracket]	TET4	aluminum 6061	-
integrating sphere [gasket / front / back]	TET4	aluminum 6061	-
solar cells	QUAD8 thin shell	*defined previously*	0.28
solar panels	HEXA8	FR4	-
boards	HEXA8	ABS	-
multiple connected bolt segment	HEXA8	steel	-

The PCB material (composed by FR-4 and copper) must be correctly modelled as its thermal properties differ in the longitudinal and transversal directions. The thermal conductivity is one of the parameters that needs to be established. According to [66], one simple way of modeling this behavior is by directly calculating the values instead of modeling the whole laminate structure, which reduces the computational time. The expressions used to obtain the planar (in plane) and normal (through-plane) thermal conductivities are given (Eq. 5.1).

$$k_{planar} = 385\frac{h_{Cu}}{h} + 0.87 \tag{5.1a}$$

$$k_{normal} = [3.23(1 - \frac{h_{Cu}}{h}) + 0.0026\frac{h_{Cu}}{h}]^{-1} \tag{5.1b}$$

The total thickness of the copper layers is represented by h_{Cu} and h is the thickness of the PCB. Knowing that all the PCBs on the ORCASat have the same thickness of 1.6 mm and are composed by
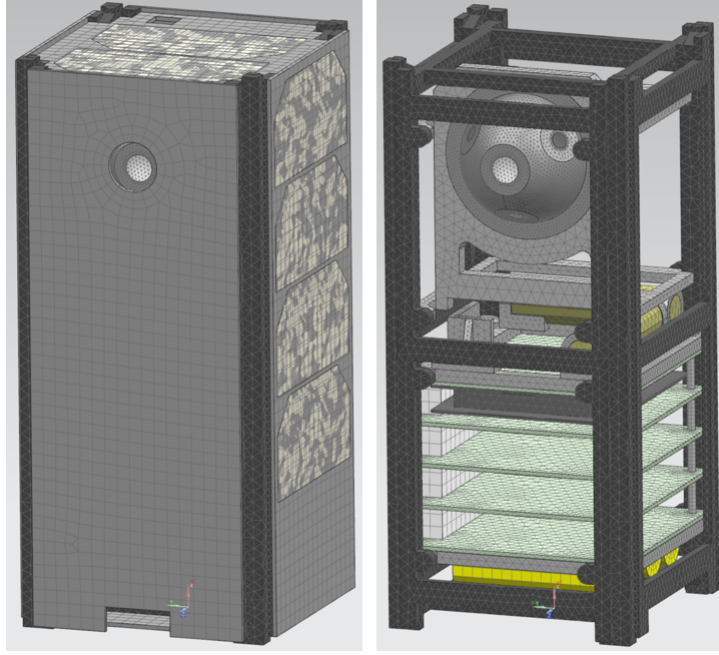
Figure 5.1: Mesh thermal model

four copper layers with a thickness of 35 μm each (140 μm, in total) it is possible to compute the thermal conductivities (Eq. 5.2).

$$k_{planar} = 34.5575 \ Wm^{-1}K^{-1} \tag{5.2a}$$

$$k_{normal} = 0.3393 \ Wm^{-1}K^{-1} \tag{5.2b}$$

The thermo-optical properties must be defined on the *.fem* file as well. Since different experimental methods to calculate parameters such as emissivity or absorptivity are used, and because these properties not only depend on the material but also on its surface, it was difficult to find coherent values from source to source. An average number was computed (Table 5.2). Initially, no passive or active thermal control was considered.

Table 5.2: Optical Properties applied in the model [67] [68] [**?**] [69] [70] [71] [72]

Material	Absorptivity α	Emissivity ε
Polished Aluminum 6061	0.15	0.05
Anodized Aluminum 6061	0.15	0.85
Brass	0.4	0.1
Copper	0.3	0.03
Steel	0.47	0.14
FR4-370HR	0.72	0.89
ABS	0.93	0.92
Black Delrin	0.96	0.87
GaInP / GaAs / Ge on Ge substrate	0.91	0.85

To apply optical properties, one must open the respective mesh collector and, on *Thermo-Optical Properties* choose the command *Open Manager*. Then, on *Type, Thermo-Optical Properties - Advanced* should be the option chosen and the user can apply the desired optical properties of the material.

The commands *mesh mating free coincident* or *glue coincident* were not used to avoid errors once the simulation is running. Every mesh is independent from another, although thermal contacts are still established on the *.sim* file.

A convergence study is presented on appendix B1.

5.1.3   Boundary Conditions and Loading

Two opposite cases were analyzed to obtain the spacecraft's behavior in space - hot case and cold case. The hot case happens when the satellite's orbit is closer to the Sun (December Solstice) and the cold case when the satellite's orbit is further away from it (June Solstice). Due to the orbit's beta angle, the ORCASat spends more time in the sunlight during the hot case and less time during the cold case (Fig. 5.2). This happens because the ORCASat's orbit is not stationary, shifting along the year. The values chosen were meant to create the worst cold case and best hot case scenario, it does not mean that the spacecraft will necessarily have those orbital characteristics at that time of the year.
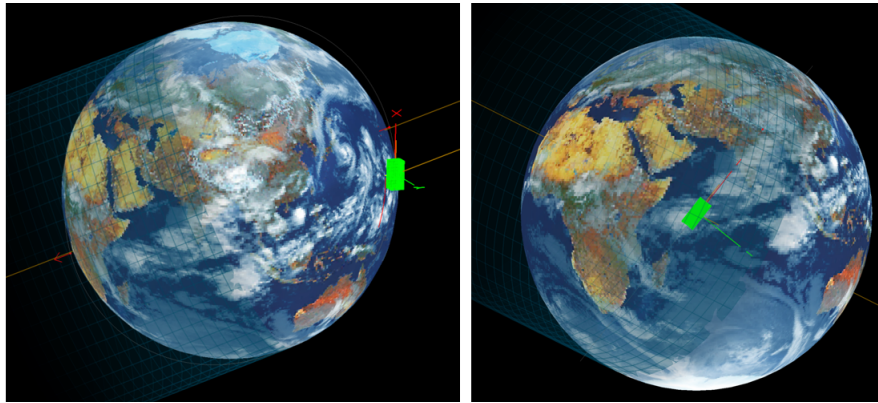
Figure 5.2: Cold case (left) and hot case (right) orbits

As the position of the Earth to the Sun is different during the whole year, the solar flux presents a different value for the hot and cold cases which changes the components heat dissipation. The values presented (Table 5.3 and 5.4) were obtained considering the power consumption requirement for each component, assuming that the power needed would be the power dissipated. The solar flux is computed automatically by *Siemens NX*.

Table 5.3: Power specifications for Hot Case [mW] and solar flux [W/m^2]

Hot Case	
Solar Flux	1411.426
ADCS PCB	750
ADCS Magnetorquers (each)	3.3
TT&C PCB	25
OBC PCB	145
Payload PCB	10
EPS PCB	920
EPS Battery (each)	35
X Solar Panel (each)	135
Y Solar Panel (each)	135
Z Solar Panel	170

Table 5.4: Power specifications for Cold Case [mW] and solar flux [W/m^2]

Cold Case	
Solar Flux	1323.682
ADCS PCB	750
ADCS Magnetorquers (each)	3.3
OBC PCB	145
EPS PCB	410
EPS Battery (each)	25

There are some parameters that should be defined on the solver *NX Space Systems Thermal* in order to reduce the simulation time. These are described.

Solution details

The solution time must be changed from *steady state* to *transient* as the satellite should be analyzed considering that its position changes over time while orbiting the Earth. Also, *NX Space Systems Thermal* allows the user of parallel processing which accelerates the simulations. The *enable multithreading* option must be selected and the *number of execution threads* defined. For instance, the author's computer had 6 cores and 12 logical processors so, the *number of execution threads* is 6.

The *maximum temperature change* in the *convergence criteria* was set to 0.1ºC and the iteration limit was changed to 1000 in the solver parameters.

Ambient condition

In this section, the *fluid temperature* and *radiative environment temperature* must be defined. The first one is related with the initial temperature the satellite starts orbiting the Earth i.e. the initial temperature at which the simulation starts. This value does not compromise the final results but it can modify the temperatures reached by the satellite during its first orbit. It can also influence the simulation time because of the number of iterations needed to reach a final value. In order to decrease this time, a value of 15ºC was defined for the hot case and a value of 8ºC was defined for the cold case. For the *radiative environment temperature*, according to [73], 4K was defined.

Transient Setup

Although some standard values are predefined in this section, the *solution time interval* was changed, having the *start time* at 0 and the *end* altered to *based on orbit period*. The *maximum number of orbits* has a standard value of 12 but this value was changed to 5 because it was observed that, after the first orbit, there was no difference on the range of temperatures. On the *results sampling*, the *number per orbit* chosen was 10 initially however, the plot of the temperatures evolution was not well defined. This value was altered to 15 which increased the time needed for the simulations but provided better data.

Other sections do not need any improvement or update unless the user pretends to do so.

By having the solution well defined it is necessary to apply the boundary conditions. The *simulation object type* command should be used and the *orbital heating*, *radiation* and *surface-to-surface contact* are the conditions applied.

Orbital Heating

This command is responsible for defining the orbit, solar and spacecraft parameters. It was assumed that the solar cells, solar panels, rail-panels, side-panels, top-cap, bottom-cap and front part of the integrating sphere were the only components that exchange radiation with the space environment. The internal components radiate to each other. When selecting the surfaces, the *selection filter* should be defined as *polygon face*, otherwise all the features of the selected parts (such as *curves*, *points*, *elements*, *polygon edge*, etc. . .) will automatically be selected as well.

On *orbit selection*, a new *orbit and attitude parameters* must be defined. The nadir vector is Z and the velocity vector is X. On *Sun Planet Characteristics*, two GMT dates were established for the hot and cold cases. In the hot case the date was 21st December 2021 (at 04:00:00) and in the cold case was 22rd June 2022 (at 10:00:00). These dates were computed using an excel provided by Space Systems/Loral (SSL), where the exact solstice dates for 2021 and 2022 were established and the moment with the maximum and minimum beta angle detected for the hot and cold case, respectively.

In the subsection *calculation positions* the *number of intervals* chosen was, initially, 2. In order to refine the calculation and obtain better data, this value was changed to 6.

Finally, on *orbit parameters*, the values are shown (Table 5.5).

Table 5.5: Orbit parameters

	Cold Case	Hot Case
Orbit Period [s]	5549.087	
Minimum Altitude [km]	400	
Eccentricity (e)	0.0005	
Orbit Inclination (i) [deg]	51.64	
Argument of Periapsis [deg]	34.8042	
Satellite Position - Local Time at Ascending Node (Ω)	10:00:00	04:00:00

The *calculation method* is *Monte Carlo* and, in the *Monte Carlo Settings* it is also advised to select *calculate view factor only* and the *number of rays* remained as 2000.

Radiation

For the thermo-optical properties to be considered by the program when the satellite is exposed to the space environment, two commands can be applied. One can use *radiation simulation object type* or *simple radiation to environment constraint type*, being the latter added after *NX 9.0* version. On the *Siemens NX Space Systems Thermal* documentation it is possible to verify that the *simple radiation to environment constraint* is used to model thermal radiation between one or more surfaces with known emissivity and an environment at specified temperature [**?**]. When this constraint is applied, the program requires an emissivity value input although it is already defined in the *.fem* file and the initial

temperature defined on the solution definitions influences not only the first orbit but the following as well. Then, if the satellite started at 10ºC or 30ºC, the temperatures reached on the first case would be much lower than the temperatures reached on the second even taking the 15º orbit as example. There is a note on the documents stating that - *to model radiation when view factors are unknown or when the radiation environment has a complex geometry, use the Radiation simulation object instead*. As the satellite presents a complex geometry, after performing several simulations where these two cases were considered and compared and after realising that the initial temperature would influence the results when the radiation constraint is applied, it was concluded that the *radiation simulation object type* should be the one chosen.

To apply the *radiation simulation object* the selection's method should be the same as described for the *orbital heating*. The *calculation method* remains the same (Monte Carlo) and the *include radiative environment* option should be selected as well as the *elements not part of this enclosure can shadow* restriction, in order to simplify the model.

Surface-to-Surface contacts

This boundary condition applies conductive and radiative conductances between surfaces. On the thermal model, the surface-to-surface contacts were automatically created and the *magnitude type* of the contact was considered as *perfect* which is an adopted simplification to also reduce the simulation time. It can be considered as a good approximation knowing that the components will be epoxied before launching the satellite.

Heat loads

Last but not least, it is necessary to apply heat loads to the components, that differ from the hot and cold cases. By using the values of the tables 5.3 and 5.4, the respective components should be selected (or respective face by setting up the filter to *polygon face*), and the *magnitude heat load* defined.

Regarding the PCBs, the circuits were not added to the model since they were not determined yet so, a strategy was adopted where, based on [1] [10], the thermal load correspondent to each circuit was applied to the whole lower area of the corresponding PCB where they should be mounted. This simplification can result in a loss of accuracy, leading to lower temperature peaks since the same thermal load is being spread over a wider area than the area of the circuit itself. However, the PCBs operational temperature go from -40 to +80ºC so it is not expected that, at Low-Earth-Orbit, the results would show such low/high values for these components. It is also a way of verifying the worst case scenario as the thermal load would be lower so, if they "survive" to this case, their reliability is ensured for the real case.

After applying all the conditions described above, it is possible to solve the thermal model and obtain the results. Initially, a single simulation would take 5 days to be completed. After the simplifications, the simulation would take between 22 to 35 hours. The data shown can be coarse however, due to time limitations, these simplifications are crucial. The *Mech & Thermals* team is advised to run these simulations again with more calculations and more results per orbit and a more refined mesh.
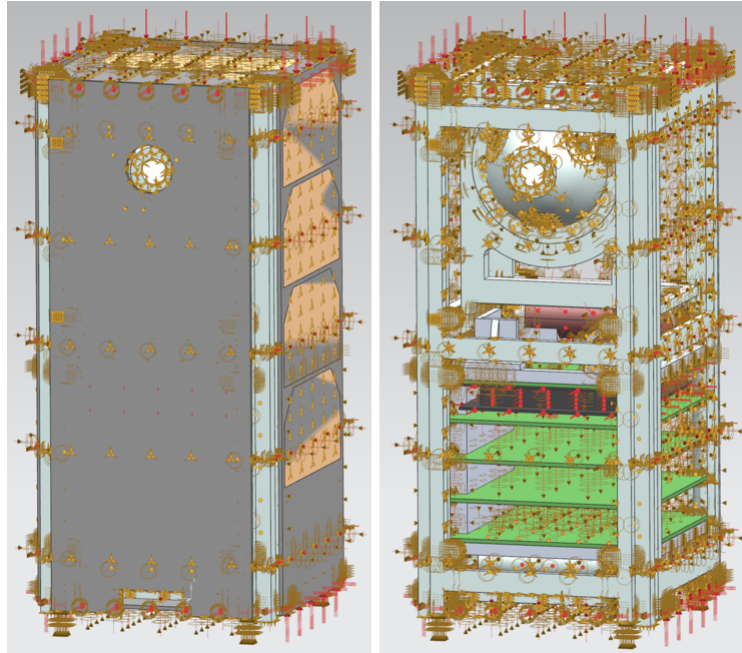
Figure 5.3: Contraints applied to the model (hot case)

5.1.4 Summary results and conclusions

On the thermal analysis it is necessary to treat the obtained data to know the satellite's thermal cycle. One can have access to the temperatures, albedo, IR and heat fluxes values per increment of time directly in the results section. In the final increment it is possible to observe the maximum and minimum temperatures as well as the time instants at which they occurred. However, as previously mentioned, the *fluid temperature* values can influence the satellite temperatures on its first orbit so, the hottest and coldest temperatures can occur on that orbit. Having this considered, the maximum and minimum values were selected from the second orbit on.

To obtain the temperature evolution, the operator should use the *post view* command to select the desired components, a random increment (not the last one) should be selected and the *temperature – nodal* are the results of most interest. Then, by choosing the *create a graph* option, defining the *start iteration* and *end iteration* and enabling *box (all)* (for 3D elements) or *feature face* (for 2D elements) a graphic with the evolution of the temperature is obtained. The values of each graphic can be extracted to an excel file by selecting the option *list*.

The maximum and minimum temperatures obtained for both hot and cold cases are presented (table 5.7) as well as the operating temperatures of each component (table 5.6). Initially, no thermal control system was applied. The solar panels had the same thermo-optical properties as the PCBs being considered as simple fiberglass epoxy materials.

The only components considered as critical are the integrating sphere, momentum wheel and batteries. For the integrating sphere and momentum wheel, the operational temperatures are between -25 to +60°C not because of the aluminum 6061/brass but due to small electrical components like laser diodes that restrict the range of this part, although removed from the model. In the case of the batteries these

Table 5.6: Operational temperatures on the thermal model [74] [47] [75] [76] [77] [49] [78]

Operational Temperatures [ºC]	
solar cells	<+150
solar panels	<+180
outer structure	<+200
integrating sphere	-25 to +60
inside structure (payload)	<+200
inside structure (PCB)	<+200
ADCS PCB	-40 to +80
OBC PCB	-40 to +80
TT&C PCB	-40 to +80
payload PCB	-40 to +80
EPS PCB	-40 to +80
PCB screws	<+500
magnetorquers	-40 to +85
magnetorquer supports	<+200
momentum wheel (bracket)	-25 to +60
air core	-40 to +120
batteries	0 to +45
boards	<+150

Table 5.7: Thermal results without TCS

	Cold Case		Hot Case		
	Min. [ºC]	Max. [ºC]	Min. [ºC]	Max. [ºC]	
+X solar cells	-26.648	0.581	-15.198	8.882	OK
-X solar cells	-29.976	12.928	-15.407	15.403	OK
+Y solar cells	-29.007	2.125	-14.958	18.000	OK
-Y solar cells	-29.652	1.099	-14.937	9.625	OK
-Z solar cells	-30.156	5.449	-15.430	10.940	OK
+X solar panel	-26.382	1.154	-14.841	9.654	OK
-X solar panel	-29.035	6.369	-14.249	13.059	OK
+Y solar panel	-28.792	2.553	-14.261	15.086	OK
-Y solar panel	-29.543	1.295	-14.826	9.882	OK
+Z solar panel	-26.568	3.497	-13.839	13.634	OK
-Z solar panel	-29.268	3.547	-14.467	11.080	OK
outer structure	-28.458	2.953	-13.621	12.180	OK
integrating sphere	-27.688	2.196	-12.366	11.354	NOT OK
inside structure (payload)	-27.999	2.430	-12.776	11.705	OK
inside structure (PCB)	-28.465	2.966	-13.499	12.217	OK
ADCS PCB	-27.850	3.239	-12.657	12.586	OK
OBC PCB	-21.860	2.080	-5.300	12.598	OK
TT&C PCB	-21.609	0.668	-5.085	11.636	OK
payload PCB	-22.819	0.926	-6.129	11.567	OK
EPS PCB	-28.321	2.868	-13.131	12.243	OK
PCB screws	-23.428	1.497	-6.841	12.041	OK
magnetorquers	-28.364	2.905	-13.057	12.185	OK
magnetorquer supports	-28.361	2.908	-13.086	12.187	OK
momentum wheel (bracket)	-28.441	2.964	-13.417	12.219	NOT OK
air core	-23.394	1.834	-7.251	12.266	OK
batteries	-28.488	2.961	-13.441	12.226	NOT OK
boards	-22.506	1.384	-5.932	11.977	OK

cannot charge below 0ºC so, the value is way below the recommended. A thermal control system will be needed.

5.2 Thermal Control System (TCS)

The ORCASat is a small satellite that receives energy from the Sun through a limited and small number of solar cells making power one of the main concerns for this mission. Instead of applying a thermal control system, the team could modify the structure or the satellite's configuration however, by the time these results are being studied, the mission is in the final phase of the Preliminary Design Review (PDR), which means that major changes to the ORCASat's configuration must be avoided at all costs.

A thermal control system is classified into passive or active.

A **passive thermal control system** does not require a power source to maintain the satellite between the desired temperatures. The most known technique is based on applying paints or coatings to the satellite's surface changing its emissivity and absorptivity. By having a surface where the emissivity is lower than the absorptivity, it is possible to heat the satellite or keep it warm during colder cases (hot cases should also be analysed after applying black coats/paints as the temperatures reached by the satellite can increase at a higher rate). Other techniques, as mentioned in [10], involve multi layer insulation surfaces to minimize the temperature gradients by absorbing or reflecting external radiation and heat dissipation by on-board components via specific radiator surfaces coated with selective thermal coatings or heat spreaders which conduct the heat from a small spot to larger heat sinks.

An **active thermal control system** requires a power source. The most common techniques are heaters and heat pipes triggered by sensors. The first one is based on a device that applies heat loads when attached to a component in order to maintain its temperature on the desired operational range. Heaters are, usually, electrical resistances that generate heat through the Joule effect (Eq. 2.35). The second one is based on fluids that move through sealed tubes. According to [79], the fluid is such that its boiling point matches the controlled unit temperature range. In the hot end of the tube, the fluid boils. The vapor expands into the pipe, carrying the heat, and when reaches the cold end, it condenses, releasing the heat and returns to the initial point, the hot end, to initiate the cycle again (Fig. 5.4).
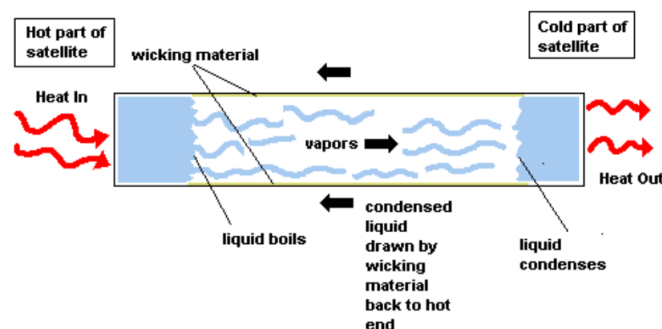
Figure 5.4: Heat pipe cycle [80]

Passive thermal control systems are more reliable, lighter, cheaper, easy to integrate and don't require any kind of power from the satellite so, these were the first being implemented. If the solutions

adopted are not enough to maintain the integrating sphere, momentum wheel and batteries between their operational range and no other option exists, an active thermal control system shall be implemented.

The solar panels were considered as black surfaces instead of the usual fiberglass epoxy material and the anodized aluminum was treated with a black paint as well changing the emissivity value to 0.90 and the absorptivity to 0.95 [71].

To have a better understanding of the changes after applying each thermal control system, these were applied one at a time. If the temperatures are still outside the operational range, both should be applied at the same time.

5.2.1 TCS - Black anodized aluminum

The data obtained (Table B.1) shows that the minimum temperature reached during the cold case for the critical components was raised, approximately, 2°C. Although the momentum wheel and the integrating sphere were almost between their operational range, the batteries were still way below the desired value of 0°C. The outer structure is not in contact with a lot of direct radiation as most of its surface area is under the solar panels which can explain why the temperatures were still very similar.

It is expected that, after applying the black solar panels, the satellite's average temperature will be higher comparing to this option.

5.2.2 TCS - Black solar panels

As expected, the temperature of the critical components raised, approximately, 5°C (Table B.2). As most of the satellite's outer area is occupied by the solar panels, by having the absorptivity changed in a higher rate than the emissivity it was possible to maintain the integrating sphere and the momentum wheel between their operational temperature. The batteries also increased their values however, these were still below the recommended. Next, both thermal control systems are applied.

5.2.3 TCS - Black anodized aluminum and black solar panels

By applying both TCS, higher values for the minimum temperature through the cold case were obtained (Table 5.8). The thermal cycle of the payload PCB is presented (Fig. 5.5) as an example. Other components have their thermal cycles presented on appendix B3. The batteries continued outside the desired temperatures but applying an active thermal control system is a decision that should be avoided at all costs.

After discussing with both *Management*, *Mech & Thermals* and *Payload* teams and studying other possible solutions, a new type of batteries with the capability of recharging under -35°C was considered.

Table 5.8: Thermal results with both TCS

	Cold Case		Hot Case		
	Min. [ºC]	Max. [ºC]	Min. [ºC]	Max. [ºC]	
+X solar cells	-18.957	15.916	-4.813	27.444	**OK**
-X solar cells	-23.045	29.497	-5.101	35.049	**OK**
+Y solar cells	-21.827	17.993	-2.184	31.957	**OK**
-Y solar cells	-22.674	16.662	-4.518	28.431	**OK**
-Z solar cells	-23.167	22.599	-5.002	30.780	**OK**
+X solar panel	-18.642	16.685	-4.387	28.471	**OK**
-X solar panel	-21.916	22.282	-3.663	32.871	**OK**
+Y solar panel	-21.605	18.568	-3.674	35.547	**OK**
-Y solar panel	-22.541	16.917	-4.382	28.780	**OK**
+Z solar panel	-18.990	18.864	-3.411	33.313	**OK**
-Z solar panel	-22.149	19.934	-3.869	30.918	**OK**
outer structure	-21.221	19.109	-2.885	31.943	**OK**
integrating sphere	-20.325	18.033	-1.211	30.855	**OK**
inside structure (payload)	-20.683	18.445	-1.705	31.284	**OK**
inside structure (PCB)	-21.238	19.125	-2.151	31.954	**OK**
ADCS PCB	-20.585	19.353	-1.746	32.351	**OK**
OBC PCB	-13.201	16.817	8.058	32.106	**OK**
TT&C PCB	-12.605	15.228	8.719	31.018	**OK**
payload PCB	-14.125	15.641	7.280	31.060	**OK**
EPS PCB	-21.072	18.985	-2.258	32.009	**OK**
PCB screws	-14.978	16.222	6.046	31.620	**OK**
magnetorquers	-21.140	19.065	-2.151	31.954	**OK**
magnetorquer supports	-21.133	19.067	-2.184	31.957	**OK**
momentum wheel (bracket)	-21.216	19.120	-2.625	31.990	**OK**
air core	-15.038	16.539	-2.644	31.997	**OK**
batteries	-21.274	19.120	-2.644	31.997	**NOT OK**
boards	-13.802	16.083	7.510	31.484	**OK**

5.3 New batteries

The old batteries were lithium-ion from *Panasonic* charging between 0 and +45ºC. The new batteries are lithium-titanate (Li4Ti5O12). These batteries use lithium-titanate nanocrystals instead of carbon and are able to recharge at -40ºC which is an impressive advancement.

These batteries have a longer life cycle compared to lithium-ion of 3000 to 7000 charge cycles. They also present higher security, stability and charge faster. One disadvantage is that LTO batteries have a lower inherent voltage of 2.4V/cell leading to a lower energy density than the conventional lithium-ion batteries [81].

The values for the recharge efficiency and capacity are presented (Table 5.10) as well as the conditions of the experimental test performed by Hunan Huahui New Energy Co. (Table 5.9).

Table 5.9: Experimental test conditions on lithium-titanate battery cells [82]

	Test Conditions
Items	Descriptions
Sample models	LTO cell 18650 1.3Ah 2.4V
Room temperature [ºC]	25 ± 2
Humidity [%]	35-75
Test methods	After the cells are discharged, charge with constant current and constant voltage at 25ºC / -20ºC / -30ºC / -35ºC / -40ºC

It is observed that the LTO batteries can recharge at -40ºC but the efficiencies are low. Nevertheless,

Table 5.10: Experimental test results on lithium-titanate battery cells [82]

Record capacity datas		
Test temperature [°C]	Recharge efficiency [%]	Capacity compared with 25°C [%]
25	100	100
-20	97	88.5
-30	83.6	66.7
-35	62.6	35.7
-40	49.5	15.1

the peaks of temperature with both TCS applied show that the worst cold case happens above -25°C with an efficiency of, approximately, 97% and a capacity, compare with 25°C, of 88.5%. Thus, this is a viable solution that must be implemented to the ORCASat, solving the problem related to low battery temperatures.

This type of batteries is being analyzed and evaluated by NanoRacks to verify if their composition presents any hazard to the space environment as they were never tested in space and can be toxic to astronauts on board the ISS. After the Preliminary Design Review presentation, NanoRacks did not provided any information or conclusions on this matter, being the batteries still under study.
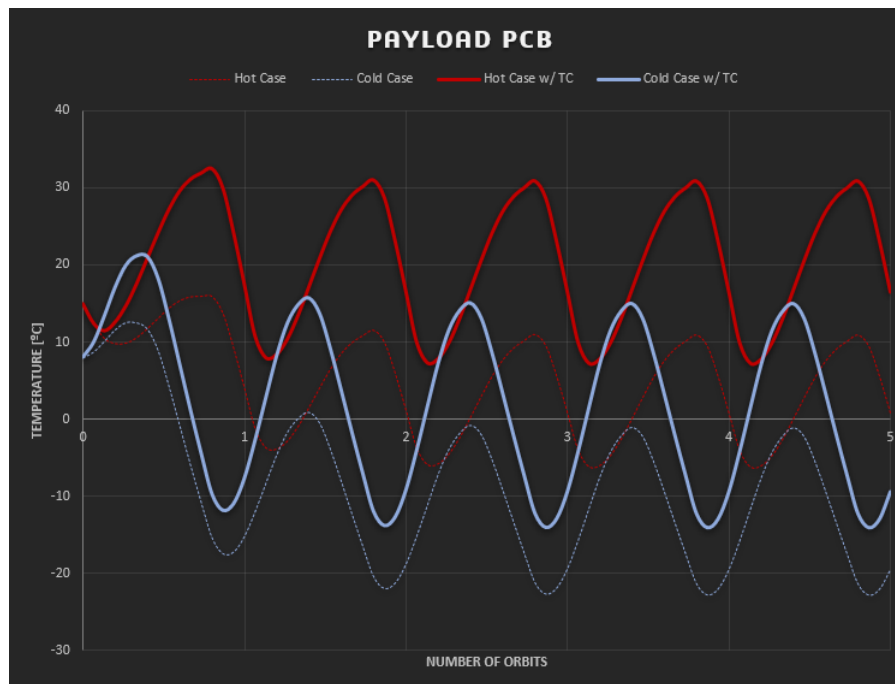
Figure 5.5: Payload PCB thermal cycle

Chapter 6

Conclusions

This thesis is defined by two main objectives. One, regarding the development of finite element models allowing the ORCASat's fundamental frequency calculation and its static behaviour as well as determining the temperatures reached by the spacecraft while in orbit. Two, regarding the structural analysis, obtain a validation of the numerical models by performing experimental vibration tests.

In the structural analysis, the satellite is represented by three models being one more complex than the other. The study was performed by using the program *Siemens NX* with the solver *NX Nastran* and two main boundary conditions were applied - the spacecraft was fixed on the $\pm$X bases or fixed along its rails - which represent the moment when the satellite is being launched. The three models showed that the ORCASat is able to maintain its physical integrity during launch being the fundamental frequency above 90 Hz on both applied situations. With the static study performed on the satellite's main structure, composed by the outer structure and 1U brackets with the integrating sphere, it was theoretically verified that the ORCASat can withstand a force of 1200 N along its length.

While the preparation of the Preliminary Design Review presentation the team was presenting a CAD model more complex and complete than the third finite element model. The study performed on the three FEM models was done on this PDR model as well. Initially it was observed that the fundamental frequency had dropped below 90 Hz however, after analyzing its modal frequencies, respective mode shapes and changing the constraints the fundamental frequency increased above this value, fulfilling the requirement.

This thesis is supported by three vibration experimental tests - one at the University of Victoria and two at the National Research Council. The experimental tests done while the development of this thesis were performed on the outer ORCASat structure represented by the first finite element model. These tests have the same purpose, determining the fundamental frequency of the structure, but the method used was different. The vibration test performed at UVic was done using a shaker as input (free vibration case) and the one performed at NRC was done using an hammer as input being the system hanged by wires (free-free vibration case). The first finite element model was adapted to the constraints of both tests and the validation of this numerical model was successfully obtained for the test performed at NRC. The UVic test allowed the team to be in touch with experimental instruments and to develop

the knowledge regarding experimental vibration tests but, unfortunately, the error between the real and numerical models was too large. Finally, the second experimental test performed at NRC was not done while the development of this work but is presented as a way of comparison with the third finite element model. No validation can be extracted from this test but it can be demonstrated that the ORCASat is likely to have a frequency above 90 Hz.

In the thermal analysis, the third finite element model is placed in orbit using the same program *Siemens NX* with the solver *NX Space Systems Thermal*. The satellite temperatures were obtained at two opposite cases, the cold case and hot case. Passive thermal control systems were applied and the spacecraft components temperatures were dragged into the operating range with the exception of the batteries. By avoiding the development of an active thermal control system due to power restrictions, the solution was to replace lithium-ion batteries by lithium-titanate. These batteries are still being analyzed by NanoRacks and the Canadian Space Agency.

To finish, on a structural level, either by numerical or experimental methods, ORCASat has a fundamental frequency above 90 Hz and can contain a force of 1200 N, proving that the spacecraft will survive during and after launch. On a thermal level, although these conditions were only observed from the numerical method, with many simplifications and adoptions, it is likely that ORCASat will survive the space environment under the stipulated orbital conditions over the expected lifetime.

All the objectives initially proposed were accomplished.

6.1   Limitations & Assumptions

During the development of this project there were some limitations and assumptions that can be synthesized and described.

Limitations:

- The processing capacity of the computer available at CfAR was better when compared to a domestic one, however, this was not enough to have a total convergence of the results for FEM models with a number of nodes above 1 million as the time required for the simulations increased exponentially;

- There is a lack of documentation and tutorials available for analysis performed using *Siemens NX*. Previous studies performed at CfAR related to other satellites such as the ECOSat-III and Homathko were used as a guide for this project;

- The CAD model provided was not complete;

- The mass of some modelled components could not be compared to the mass of the real ones as this information was not provided by the suppliers;

- *Siemens NX* requires several properties to fully characterize the materials implemented on the FEM model when these are not available in the software. Some properties were not put as the information was not found;

- On both vibration tests performed at UVic and NRC, the only components available and machined were the top-cap, bottom-cap, side-panels and rail-panels. The validation of the numerical study was

limited to the simplest model;

- The team did not have the chance to perform a thermal experimental test to validate the numerical results obtained using *Siemens NX Space Systems Thermal*;

- Due to the lack of time, it was not possible to perform a complex optimization to the FEM model.

Assumptions:

- The surface-to-surface contacts were considered as perfect with zero friction. This could affect the linear static analysis as well as the vibration analysis results;

- The density of the materials is changed to achieve an equal mass between the numerical and real model which is a procedure that can influence the results;

- In the thermal analysis, a convergence study is performed however, the model used during this study is the one with the smallest number of nodes and it is assumed to be correct because of computational limitations;

- To apply the heat loads it is considered that the power needed for the instruments is the power dissipated;

- An average value for the optical properties of the different components was computed.

6.2 Recommendations for Future work

After having more components ready, machined and assembled, the first recommendation is to build a bill of materials with all the standard mechanical, thermal and optical properties of the ORCASat. This way, the mass between the numerical and the real models can be correctly compared and; the time needed while the preparation of the *.fem* files, when assigning the materials, is decreased. Also, this makes sub-teams use the same values when using different programs like *SolidWorks*, *Siemens NX* or *Abaqus*. During the development of this thesis, only a few components had their comparison done. Also, there were some adaptations in the assigned materials because some properties were unknown or their values varied from source to source.

Structurally:

- Perform an experimental vibration test to a more complete model;

- The experimental test should apply the launch conditions to the model, if possible;

- Perform a complex optimization to the model, if necessary. This thesis only shows an update to the model in terms of mass, however, an optimization where more parameters are evaluated, such as Young Modulus and structural dimensions, are important as they approximate the real and numerical models;

- If the team is not willing to perform an optimization, it is advised to apply the mass changes presented in this thesis to the next finite element models.

Thermally:

- Perform a thermal analysis on the PDR or an up-to-date CAD model;

- Improve the model's resolution by increasing the number of calculations per orbit and the number of elements in the mesh;

- Increase the computational resources for a better convergence of the results;

- After modelling the electrical components, one is able to apply the thermal loads locally instead of doing it in the lower PCB area while the preparation of the finite element model;

- Although the satellite can survive the space environment, if the LTO batteries are applied, simulate the thermal model with an active battery heater to raise the minimum cold case temperature above 0°C and to study the impact of this active thermal control system in the power budget;

- Besides the black paint, the team can investigate other options to raise the minimum temperatures, such as reducing the conduction in the structural joints or using some sort of insulation, if time allows it;

- Perform an experimental thermal test on the complete model or, at least, on the critical components such as the payload, batteries and antenna in order to validate the thermal numerical model.

To conclude, besides these recommendations, the team is advised to read this thesis carefully and use it as a guide for future structural and thermal analysis.

Bibliography

[1] S. C. Aboobakar. Dynamic and thermal models for ecosat-iii, November 2016. Master's Thesis, Instituto Superior Técnico, University of Lisbon.

[2] B. Lal and T. Zurbuchen. *Achieving Science with CubeSats: Thinking Inside the Box*. National Academy of Sciences, 2016.

[3] M. N. Sweeting. *Smaller Satellites: Bigger Business?*, volume 6, chapter Micro/Nanosatellites - The New World, pages 1–19. Springer, 2002. ISBN:978-1402001994.

[4] Figures. From Nanosats Database, . URL `https://www.nanosats.eu/`. Accessed 15/11/2019.

[5] A. Moore, H. Heidt, J. Puig-Suari, S. Nakasuka, and R. Twiggs. Cubesat: A new generation of picosatellite for education and industry low-cost space experimentation. 2000. URL `https://digitalcommons.usu.edu/smallsat/2000/All2000/32/`.

[6] S. Lee, A. Hutputanasin, A. Toorian, W. Lan, R. Munakata, J. Carnahan, D. Pignatelli, and A. Mehrparvar. Cubesat Design Specification REV. 13. 2014. URL `https://www.academia.edu/11525487/CubeSat_Design_Specification_Rev._13_The_CubeSat_Program_Cal_Poly_SLO_CubeSat_Design_Specification_CDS_REV_13_Document_Classification_X_Public_Domain_ITAR_Controlled_Internal_Only`.

[7] A basic guide to nanosatellites. From Alén, . URL `https://alen.space/basic-guide-nanosatellites/`. Accessed 15/11/2019.

[8] W. Lan, R. Munakata, R. Nugent, and D. Pignatelli. Poly Picosatellite Orbital Deployer Mk. III Rev. E, User Guide. 2014. URL `https://static1.squarespace.com/static/5418c831e4b0fa4ecac1bacd/t/5806854d6b8f5b8eb57b83bd/1476822350599/P-POD_MkIIIRevE_UserGuide_CP-PPODUG-1.0-1_Rev1.pdf`.

[9] D. Selva and D. Krejci. A survey and assessment of the capabilities of Cubesats for Earth observation. 2011. URL `https://www.academia.edu/6856555/A_survey_and_assessment_of_the_capabilities_of_Cubesats_for_Earth_observation`.

[10] L. R. Simões. Study of low earth orbit impact on orca2sat subsystems, January 2019. Master's Thesis, University of Beira Interior.

[11] C. Satter and S. E. Matousek. *Smaller Satellites: Bigger Business?*, volume 6, chapter The Promisses of Nanotechnology: Will They be Kept?, pages 33–42. Springer, 2002. ISBN:978-1402001994.

[12] B. Lobo-Fernandes. Design and analysis of an attitude determination and control system for the orcasat nanosatellite, June 2019. Master's Thesis, Insituto Superior Técnico, University of Lisbon.

[13] A. Doknjas, B. Edwards, B. Lobo-Fernandes, P. Ogilvie, R. Arthurs, and A. Zoltan. Mission Concept Review Document. January 2019.

[14] Photometric calibration and the monitor telescope, . URL `https://www.astro.princeton.edu/PBOOK/photcal/photcal.htm`. Accessed 10/08/2019.

[15] J. Albert. Satellite-Mounted Light Sources as Photometric Calibration Standards for Ground-Based Telescopes. January 2012. URL `https://iopscience.iop.org/article/10.1088/0004-6256/143/1/8/pdf`.

[16] J. Archer. Natural Vibration Modal Analysis. September 1968. URL `https://ntrs.nasa.gov/archive/nasa/casi.ntrs.nasa.gov/19690013408.pdf`.

[17] S. S. Rao. *Mechanical Vibrations, Fifth Edition*. Prentice Hall Upper Saddle River, 2011. ISBN:978-0132128193.

[18] Siemens NX: Basic Dynamic Analysis User's Guide, 2014. URL `https://docs.plm.automation.siemens.com/data_services/resources/nxnastran/10/help/en_US/tdocExt/pdf/basic_dynamics.pdf`. Siemens Product Lifecycle Management Software Inc.

[19] N. Larbi and J. Lardies. *Experimental Modal Analysis of a Structure Excited by a Random Force*, volume 14, pages 181–192. Mechanical Systems and Signal Processing, 2000.

[20] P. Avitabile. *Experimental Modal Analysis: A Simple Non-Mathematical Presentation*, volume 35, pages 20–31. Sound and Vibration, 2001.

[21] T. L. Bergman, F. P. Incropera, D. P. DeWitt, and A. S. Lavine. *Fundamentals of Heat and Mass Transfer, Seventh Edition*. John Wiley & Sons, 2011. ISBN:978-0470501979.

[22] Extraterrestial radiation, . URL `https://www.sciencedirect.com/topics/engineering/extraterrestrial-radiation`. Accessed 14/11/2019.

[23] Apsis, . URL `https://www.wikiwand.com/simple/Apsis`. Accessed 14/11/2019.

[24] W. J. Larson and J. R. Wertz. *Space Mission Analysis and Design, Third Edition*. The Space Technology Library, 1999.

[25] J. E. Oliver. *Encyclopedia of World Climatology*, pages 32–35. Springer Science & Business Media, 2008.

[26] T. Markvart and L. Castalzer. *Practical Handbook of Photovoltaics: Fundamentals and Applications*. Elsevier, 2003. ISBN:978-1856173902.

[27] Thermodynamics: Albedo From National Snow and Ice Data Center, . URL `https://nsidc.org/cryosphere/seaice/processes/albedo.html`. Accessed 15/11/2019.

[28] The climate system From Manchester Metropolitan University, . URL `https://web.archive.org/web/20030301133707/http://www.ace.mmu.ac.uk/Resources/gcc/1-3-3.html`. Accessed 15/11/2019.

[29] G. Tetzlaff. *Albedo of the Sahara. Cologne University Satellite Measurement of Radiation Budget Parameters*, pages 60–63. 1983.

[30] Albedo From Climate Data Information, . URL `http://www.climatedata.info/forcing/albedo/`. Accessed 15/11/2019.

[31] Earth fact sheet, . URL `https://nssdc.gsfc.nasa.gov/planetary/factsheet/earthfact.html`. Accessed 15/11/2019.

[32] A. D. Luca. *Architectural Design Criteria for Spacecraft Solar Arrays*. Intech, November 2011. URL `http://cdn.intechopen.com/pdfs/22805/InTech-Architectural_design_criteria_for_spacecraft_solar_arrays.pdf`.

[33] G. L. Matloff. *Deep space probes: To the outer solar system and beyond*. Springer, 2006. ISBN:978-3540273400.

[34] Pinclipart, . URL `https://www.pinclipart.com/pindetail/TwiJx_convection-science-clipart-convection-heat-transfer-convection-current/`. Accessed 16/11/2019.

[35] Siemens NX: Thermal Analysis User's Guide, 2017. URL `https://docs.plm.automation.siemens.com/data_services/resources/nxnastran/12/help/tdoc/en_US/pdf/thermal.pdf`. Siemens Product Lifecycle Management Software Inc.

[36] G. T. Georgiev and J. J. Butler. Long-term calibration monitoring of Spectralon diffuser BRDF in the air-ultraviolet. November 2007.

[37] A. E. Stiegman, C. J. Bruegge, and A. W. Springsteen. Ultraviolet stability and contamination analysis of Spectralon diffuse reflectance material. April 1993.

[38] K. J. Voss and H. Zhang. Bidirectional reflectance of dry and submerged Labsphere Spectralon plaque. 2006.

[39] G. Sterling, A. Cheng, M. Caverley, D. Stood, and D. Came. *Earth and Space 2012: Enginneering, Science, Construction and Operations in Challenging Environments*, chapter Design of radio telescope calibration payload for a nano-satellite, pages 355–364. 2012.

[40] T. Prejean, H. Martin, C. Brown, T. Guy, T. Freund, and M. Lewis. NanoRacks CubeSat Deployer (NRCSD) - Interface Definition Document (IDD). May 2018.

[41] A. Ng. Canadian CubeSat Project - Design Specification. September 2018.

[42] J. Albert, A. Suleman, D. Michelson, P. Driessen, A. Doknjas, B. Edwards, B. Lobo-Fernandes, P. Ogilvie, T. Tarnowski, J. Duarte, L. Romeiro, B. Sabino, B. Mazerolle, M. Azeem, K. Desai, B. Sommerfield, S. Bichlmaier, L. Buzas, R. Arthurs, and A. Zoltan. ORCASat Preliminary Design Review. October 2019.

[43] Aluminum 7075-T6; 7075-T651 From MatWeb, . URL `http://www.matweb.com/search/DataSheet.aspx?MatGUID=4f19a42be94546b686bbf43f79c51b7d`. Accessed 05/06/2019.

[44] Aluminum 6061-T6; 6061-T651 From MatWeb, . URL `http://matweb.com/search/DataSheet.aspx?MatGUID=b8d536e0b9b54bd7b69e4124d8f1d20a&ckck=1`. Accessed 05/06/2019.

[45] Properties provided by Siemens NX.

[46] Backplane PCBs From Saturn Flex Systems, . URL `https://www.saturnflex.com/products/backplane_pcb.php`. Accessed 10/09/2019.

[47] Isola FR4-370HR High Performance Laminate and Prepreg, . URL `https://www.isola-group.com/wp-content/uploads/data-sheets/370hr.pdf`. Accessed 05/06/2019 (some properties were provided by email).

[48] L. A. A. Beex. Warpage of Printed Circuit Boards - Bachelor Final Project, May 2005.

[49] Panasonic Lithium Ion NCR18650B, . URL `https://www.batteryspace.com/prod-specs/NCR18650B.pdf`. Accessed 05/06/2019.

[50] Panasonic Lithium Ion NCR18650B (From NKON), . URL `https://ru.nkon.nl/rechargeable/li-ion/18650-size/panasonic-ncr18650b-made-in-japan.html`. Accessed 16/11/2019.

[51] Receivers OEM719, . URL `https://www.novatel.com/assets/Documents/Papers/OEM719-Product-Sheet.pdf`. Accessed 05/06/2019.

[52] SS200 Sun Sensor From Hyperion Technologies, . URL `https://hyperiontechnologies.nl/wp-content/uploads/2015/07/HT-SS-200-V1.2_Flyer.pdf`. Accessed 05/06/2019.

[53] RW210 Series Reaction Wheel From Hyperion Technologies, . URL `https://hyperiontechnologies.nl/wp-content/uploads/2018/07/HT-RW210_V1.02_Flyer.pdf`. Accessed 05/06/2019.

[54] Delrin Homopolymer Material Specifications From Technical Products, Inc., . URL `https://www.technicalproductsinc.com/pdf/Specs/Delrin%20Specs.pdf`. Accessed 06/06/2019.

[55] Delrin (Acetal Homopolymer) From Ensinger-Hyde, . URL `http://www.sdplastics.com/delrin/delrin%5b1%5d.pdf`. Accessed 06/06/2019.

[56] 30% Triple Junction GaAs Solar Cell Assembly - Type: TJ Solar Cell Assembly 3G30A From AZURSPACE Solar Power GMBH, . URL `http://www.azurspace.com/images/products/0003401-01-01_DB_3G30A.pdf`. Accessed 06/06/2019.

[57] GaAs - Gallium Arsenide - Mechanical properties, elastic constants, lattice vibrations, . URL `http://www.ioffe.ru/SVA/NSM/Semicond/GaAs/mechanic.html`. Accessed 06/06/2019.

[58] A. Israr. Vibration and Modal Analysis of Low Earth Orbit Satellite. August 2014. URL `https://www.hindawi.com/journals/sv/2014/740102/`.

[59] C. Liu, X. Jing, S. Daley, and F. Li. *Mechanical Systems and Signal Processing*, volume 56-57, chapter Recent advances in micro-vibration isolation, pages 55–80. May 2015.

[60] G. S. Aglietti, Z. Zhang, G. Richardson, B. L. Page, and A. Haslehurstl. Disturbance Sources Modeling for Analysis of Structure-Borne Micro-Vibration. May 2011. URL `http://congress.cimne.com/eccomas/proceedings/compdyn2011/compdyn2011_full/286.pdf`.

[61] M. Privat. On ground and in orbit microvibrations measurement comparison. 1999. URL `http://esmats.eu/esmatspapers/pastpapers/pdfs/1999/privat.pdf`.

[62] Model 356A01 From PCB Piezotronics, . URL `https://www.pcb.com/products?model=356A01`.

[63] What is a Frequency Response Function (FRF)? From Siemens, . URL `https://community.sw.siemens.com/s/article/what-is-a-frequency-response-function-frf`. Accessed 24/10/2019.

[64] P. Nuiji and D. Rijlaarsdam. From Signal Analysis to System Analysis From Introduction to Frequency Response Function Measurements. 2014.

[65] G. F. Abdelal, N. Abuelfoutouth, and A. H. Gad. *Finite Element Analysis for Satellite Structures: Applications to their Design, Manufacture and Testing*. Springer, 2012.

[66] J. E. Graebner. *Thermal conductivity of printed wiring boards*. Electronics Cooling Magazine, 1995.

[67] D. G. Gilmore. *Spacecraft Thermal Control Handbook, Volume I: Fundamental Technologies*. 2002.

[68] Emissivity Table From ThermoWorks, . URL `https://www.thermoworks.com/emissivity-table`. Accessed 8/07/2019.

[69] Absorptivity & Emissivity table, . URL `http://www.solarmirror.com/fom/fom-serve/cache/43.html`. Accessed 8/07/2019.

[70] I. Martínez. Thermo-Optical Properties. 1995-2019. URL `http://webserver.dmt.upm.es/~isidoro/dat1/Thermooptical.pdf`.

[71] J. H. Henninger. Solar Absorptance and Thermal Emittance of Some Common Spacecraft Thermal-Control Coatings From NASA Reference Publication. April 1984. URL `https://ntrs.nasa.gov/archive/nasa/casi.ntrs.nasa.gov/19840015630.pdf`.

[72] L. Kauder. Spacecraft Thermal Control Coatings References From NASA. 2005. URL `https://ntrs.nasa.gov/archive/nasa/casi.ntrs.nasa.gov/20070014757.pdf`.

[73] A. Tewari. *Atmospheric and Space Flight Dynamics*. Springer, 2007.
)]website:simple Simple Radiation to Environment, . URL `azurspace.com`. Accessed 1/08/2019.

[74] Handling of semiconductor products, . URL `http://www.azurspace.com`.

[75] Aluminium / Aluminum 6061 Alloy From AZO Materials. URL `https://www.azom.com/article.aspx?ArticleID=6636`. Accessed 06/10/2019.

[76] The Stainless Steel Information Center - Specially Steel Industry of North America. URL `http://www.ssina.com/composition/temperature.html`. Accessed 06/10/2019.

[77] Delrin - The High-Performance Acetal Resin From Dupont Transportation & Industrial. URL `https://www.dupont.com/products/delrin.html`. Accessed 06/10/2019.

[78] Polybutylene terephthalate From Encyclopedia Britannica. URL `https://www.britannica.com/science/polybutylene-terephthalate`. Accessed 06/10/2019.

[79] V. Agrawal and A. K. Maini. *Satellite Technology: Principles and Applications, Second Edition*. Wiley, 2011.

[80] Satellites. URL `https://www.courses.psu.edu/aersp/aersp055_r81/satellites/satellites.html`.

[81] AA Portable Power Corp, Category: LTO Batteries. URL `https://www.batteryspace.com/Lithium-Titanate-Battery.aspx`.

[82] LTO18650 1.3Ah 2.4V - Capacity Vs Temperature test. Document provided by the ORCASat manager Alex Doknjas.

[83] Solution dialog box — Restart From Siemens. URL `https://docs.plm.automation.siemens.com/tdoc/nx/12/nx_help/#uid:xid1128419:index_advanced:id1121662:id629556:id629236`.

Appendix A

Dynamic and Static Analysis (Graphics and Tables)

A.1 Idealization Process

Table A.1: Idealization process on the air-core

	air-core						
Modes	Real Freq. [Hz]	Idealized Freq. (1) [Hz]	Idealized Freq. (2) [Hz]	Idealized Freq. (3) [Hz]	Error (1) [%]	Error (2) [%]	Error (3) [%]
7	158.3	156	144.1	144.7	1.453	8.970	8.591
8	544.6	548.4	505.1	499.7	0.698	7.253	8.245
9	614	616.6	642.1	639.7	0.423	4.577	4.186
10	901.8	916.5	915.2	900.5	1.630	1.486	0.144
11	1037	1037	1007	999.3	0.000	2.893	3.635
12	1178	1179	1192	1186	0.085	1.188	0.679
13	1559	1572	1506	1479	0.834	3.400	5.131
14	1737	1687	1647	1614	2.879	5.181	7.081
15	1886	1799	1857	1817	4.613	1.538	3.659
16	1894	1814	1922	1887	4.224	1.478	0.370
17	1911	1857	1976	1977	2.826	3.401	3.454
18	1934	1889	2057	1986	2.327	6.360	2.689
19	1936	1892	2060	2013	2.273	6.405	3.977
20	2044	1893	2192	2183	7.387	7.241	6.800

Table A.2: Idealization process on batteries

	battery		
Modes	Real Freq. [Hz]	Idealized Freq. [Hz]	Error [%]
7	27140	27020	0.442
8	27140	27020	0.442
9	40190	40130	0.149
10	61460	61230	0.374
11	61460	61230	0.374
12	64390	64210	0.280
13	80380	80260	0.149
14	100000	99750	0.250
15	100000	99750	0.250
16	120600	120400	0.166
17	127000	126600	0.315
18	137300	137000	0.218
19	137300	137000	0.218
20	160700	160500	0.124

Table A.3: Idealization process on magnetorquer brackets

	magnetorquer brackets				
Modes	Real Freq. [Hz]	Idealized Freq. (1) [Hz]	Idealized Freq. (2) [Hz]	Error (1) [%]	Error (2) [%]
7	9203	9178	10100	0.272	9.747
8	9541	9361	11920	1.887	24.934
9	15670	15560	16490	0.702	5.233
10	18590	19450	21970	4.626	18.182
11	26480	27260	27650	2.946	4.418
12	26700	28040	30440	5.019	14.007
13	29620	29930	32920	1.047	11.141
14	31400	33810	39890	7.675	27.038
15	33180	35620	39900	7.354	20.253
16	42080	42530	49970	1.069	18.750
17	47280	47890	52450	1.290	10.935
18	52630	54610	66830	3.762	26.981
19	65800	67100	72760	1.976	10.578
20	67170	70250	74900	4.585	11.508

Table A.4: Idealization process on PCB brackets

		PCB bracket			
Modes	Real Freq. [Hz]	Idealized Freq. (1) [Hz]	Idealized Freq. (2) [Hz]	Error (1) [%]	Error (2) [%]
7	702.1	690.3	685.4	1.681	2.379
8	1009	971.4	969.6	3.726	3.905
9	1662	1656	1655	0.361	0.421
10	1672	1671	1668	0.060	0.239
11	2253	2247	2238	0.266	0.666
12	2780	2771	2750	0.324	1.079
13	3140	3055	3055	2.707	2.707
14	3192	3193	3170	0.031	0.689
15	3498	3437	3427	1.744	2.030
16	4678	4459	4472	4.681	4.404
17	6021	5991	5988	0.498	0.548
18	6360	6296	6298	1.006	0.975
19	6558	6524	6494	0.518	0.976
20	6746	6732	6718	0.208	0.415

Table A.5: Idealization process on the momentum wheel back part

	momentum wheel (back)		
Modes	Real Freq. [Hz]	Idealized Freq. [Hz]	Error [%]
7	1600	1534	4.125
8	4466	4327	3.112
9	5163	4979	3.564
10	5163	5003	3.099
11	5370	5571	3.743
12	11640	11240	3.436
13	11830	11550	2.367
14	15260	14480	5.111
15	15610	14970	4.100
16	15620	15050	3.649
17	16160	15150	6.250
18	16160	15470	4.270
19	16320	15510	4.963
20	17730	17090	3.610

Table A.6: Idealization process on the momentum wheel front part

	momentum wheel (front)		
Modes	Real Freq. [Hz]	Idealized Freq. [Hz]	Error [%]
7	6116	6077	0.638
8	9242	9231	0.119
9	11180	11160	0.179
10	16270	16230	0.246
11	16270	16230	0.246
12	27970	27840	0.465
13	27970	27850	0.429
14	32380	32180	0.618
15	33080	33000	0.242
16	33130	33080	0.151
17	45380	45300	0.176
18	45380	45310	0.154
19	48600	48560	0.082
20	52720	52660	0.114

Table A.7: Idealization process on the momentum wheel octogonal part

	momentum wheel (octogonal)		
Modes	Real Freq. [Hz]	Idealized Freq. [Hz]	Error [%]
7	5743	5799	0.975
8	5773	5834	1.057
9	9888	10030	1.436
10	13150	13320	1.293
11	13380	13550	1.271
12	21520	21900	1.766
13	22100	22390	1.312
14	22160	22630	2.121
15	24740	25130	1.576
16	34720	35100	1.094
17	35040	35560	1.484
18	37490	37970	1.280
19	37500	38280	2.080
20	40970	42070	2.685

Table A.8: Idealization process on the momentum wheel bracket

	momentum wheel (bracket)				
Modes	Real Freq. [Hz]	Idealized Freq. (1) [Hz]	Idealized Freq. (2) [Hz]	Error (1) [%]	Error (2) [%]
7	7192	9216	9287	28.142	29.130
8	8895	9947	10290	11.827	15.683
9	13420	15850	15870	18.107	18.256
10	21970	24290	24550	10.560	11.743
11	24630	31360	31300	27.324	27.081
12	29020	33260	33990	14.611	17.126
13	31230	35710	35720	14.345	14.377
14	33650	36410	38150	8.202	13.373
15	35230	44830	44900	27.250	27.448
16	40450	48330	48310	19.481	19.431
17	44190	49150	49660	11.224	12.378
18	45410	51230	52240	12.817	15.041
19	49860	53140	53590	6.578	7.481
20	51150	58150	58420	13.685	14.213

Table A.9: Idealization process on the payload bracket

	payload bracket		
Modes	Real Freq. [Hz]	Idealized Freq. [Hz]	Error [%]
7	729	714.8	1.948
8	1171	1145	2.220
9	1215	1146	5.679
10	1587	1499	5.545
11	2122	2086	1.697
12	2163	2166	0.139
13	2940	2664	9.388
14	3316	3295	0.633
15	3746	3686	1.602
16	5141	5108	0.642
17	5234	5200	0.650
18	5989	5752	3.957
19	6259	6251	0.128
20	7875	7761	1.448

Table A.10: Idealization process on the side-panel

	side-panel		
Modes	Real Freq. [Hz]	Idealized Freq. [Hz]	Error [%]
7	311.8	310.1	0.545
8	368.5	369.9	0.380
9	673.8	669.8	0.594
10	875.6	836.2	4.500
11	879.8	841.9	4.308
12	1150	1151	0.087
13	1154	1156	0.173
14	1460	1460	0.000
15	1793	1780	0.725
16	1839	1825	0.761
17	2006	1995	0.548
18	2357	2314	1.824
19	2516	2510	0.238
20	2662	2575	3.268

Table A.11: Idealization process on the front part of the integrating sphere

	integrating sphere (front)		
Modes	Real Freq. [Hz]	Idealized Freq. [Hz]	Error [%]
7	3685	3303	10.366
8	3686	3304	10.364
9	10080	8833	12.371
10	10240	8946	12.637
11	15660	14990	4.278
12	15690	15790	0.637
13	17930	18070	0.781
14	18440	18640	1.085
15	20170	18720	7.189
16	20980	19390	7.579
17	21350	20080	5.948
18	21660	20120	7.110
19	22940	20400	11.072
20	23030	20820	9.596

Table A.12: Idealization process on the integrating sphere bracket

	integrating sphere (bracket)				
Modes	Real Freq. [Hz]	Idealized Freq. (1) [Hz]	Idealized Freq. (2) [Hz]	Error (1) [%]	Error (2) [%]
7	1611	1613	1609	0.124	0.124
8	2286	2293	2287	0.306	0.044
9	3929	3922	3918	0.178	0.280
10	4142	4161	4142	0.459	0.000
11	5247	5402	5236	2.954	0.210
12	5460	5469	5457	0.165	0.055
13	6393	6636	6391	3.801	0.031
14	6755	6772	6732	0.252	0.340
15	8492	8470	8423	0.259	0.813
16	9250	9186	9151	0.692	1.070
17	9665	9295	9295	3.828	3.828
18	9881	9778	9773	1.042	1.093
19	11510	11490	11500	0.174	0.087
20	12780	12730	12750	0.391	0.235

A.2 Static Analysis

Table A.13: Static analysis convergence study for force applied on top

Force applied on Top										
outer structure [mm]	3.5	3	2.5	2.4	2.3	2.2	2.1	2	1.9	1.8
1U brackets [mm]	3.5	3	2.5	2.4	2.3	2.2	2.1	2	1.9	1.8
integrating-sphere [mm]	3.5	3	2.5	2.4	2.3	2.2	2.1	2	1.9	1.8
number of nodes	213 277	280 775	382 834	409 598	446 983	498 012	526 916	587 807	636 055	726 456
mass [kg]	0.613057	0.612657	0.612536	-	-	-	-	0.612324	-	-
stress-elemental [MPa]	10.946	12.27	11.661	11.431	11.276	11.676	11.627	11.88	12.03	11.901
stress-elemental-nodal [MPa]	15.66	15.04	17.33	22.6	24.05	22.87	22.71	22.73	21.8	22.56

Table A.14: Static analysis convergence study for force applied at the bottom

Force applied at the Bottom							
outer structure [mm]	3.5	3	2.5	2.4	2.3	2.2	2.1
1U brackets [mm]	3.5	3	2.5	2.4	2.3	2.2	2.1
integrating-sphere [mm]	3.5	3	2.5	2.4	2.3	2.2	2.1
number of nodes	213 277	280 775	382 834	409 598	446 983	498 012	526 916
mass [kg]	0.613057	0.612657	0.612536	-	-	-	-
stress-elemental [MPa]	10.967	12.3	11.716	11.486	11.336	11.74	11.696
stress-elemental-nodal [MPa]	18.6	20.94	23.84	26.01	27.57	26	27.52

A.3   Experimental tests

Table A.15: Convergence study on the model representing the experimental test performed at UVic

outer_structure [mm]	4	3.5	3	2.5	2	1.5
plate [mm]	4	3.5	3	2.5	2	1.5
mass [kg]	0.6002266	0.5999383	0.5996439	0.599526	0.599399	0.5994509
number of nodes	126 626	153 577	197 082	271 000	414 407	751 189
number of elements	60 621	74 573	97 207	139 043	221 667	421 608
mode 1 [Hz]	224.3	221.5	221.2	219.9	219.1	218.1
mode 2 [Hz]	244.3	243.6	243	242.4	241.7	240.7
mode 3 [Hz]	348	345.2	344.7	342.8	341.8	339.9
mode 4 [Hz]	725.9	723.8	721.9	720.5	719	717.7
mode 5 [Hz]	1063	1057	1056	1051	1049	1046
mode 6 [Hz]	1113	1110	1106	1105	1102	1098
mode 7 [Hz]	1260	1255	1251	1246	1243	1239
mode 8 [Hz]	1459	1453	1450	1445	1442	1437
mode 9 [Hz]	1626	1621	1616	1611	1607	1603
mode 10 [Hz]	1747	1742	1736	1732	1727	1723

Table A.16: Convergence study on the model representing the experimental test performed at NRC

outer_structure [mm]	4	3.5	3	2.5	2	1.5
mass [kg]	0.4279078	0.427635	0.4273659	0.4272617	0.427135	0.4271988
number of nodes	123 501	149 843	192 583	262 288	400 167	723 010
number of elements	58 585	72 123	94 273	132 756	211 355	399 517
mode 1 [Hz]	474.4	473.6	472.5	472.1	471.5	470.8
mode 2 [Hz]	576.1	572.6	570.9	569.9	568.7	567.5
mode 3 [Hz]	737.7	729.9	727.3	726.1	724	722.1
mode 4 [Hz]	816.5	816.1	815.2	814.8	813.9	813.2
mode 5 [Hz]	912.6	910.4	908.6	907.5	906.2	905.4
mode 6 [Hz]	1033	1030	1028	1027	1026	1025
mode 7 [Hz]	1220	1216	1211	1207	1204	1201
mode 8 [Hz]	1239	1234	1231	1229	1227	1225
mode 9 [Hz]	1284	1282	1279	1277	1275	1273

Appendix B

Thermal Analysis (Graphics and Tables)

B.1 Thermal Model Convergence

A convergence analysis should be done in order to verify that the mesh and number of calculations per orbit applied will result on reliable data. The difference between doing a convergence analysis in the vibration/static model and in the thermal model is that the time can go from 1 hour in the vibration analysis to 2 weeks in the thermal analysis. Not only the number of elements should be changed to know the adequacy of the mesh but it is important to evaluate if the number of orbital positions to compute the spacecraft's temperature is enough to obtain a converged solution [10]. Thus, both parameters should not be increased at the same time (otherwise the time needed to have a solution would be too long) but should be increased one at a time.

The first study was based on using a coarse mesh and increasing the number of orbital positions, evaluating the temperatures at the same time instant and same location in the model - top-cap, exit port of the integrating sphere and ADCS PCB. The same process was done by increasing the number of nodes but fixing the number of orbital positions at 6.

The solutions never fully converged but it can be seen that the difference between the values is small (Fig. B.1 and B.2). Considering this, the thermal analysis was done for a model with 63955 nodes and 6 calculations per orbit.
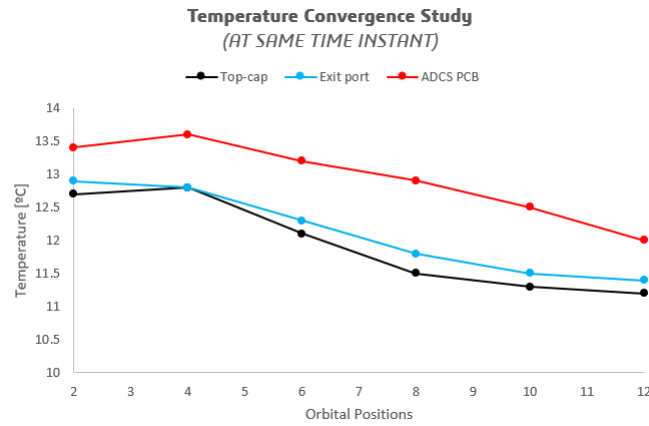
Figure B.1: Temperature convergence study fixing the number of nodes and varying the number of calculations per orbit
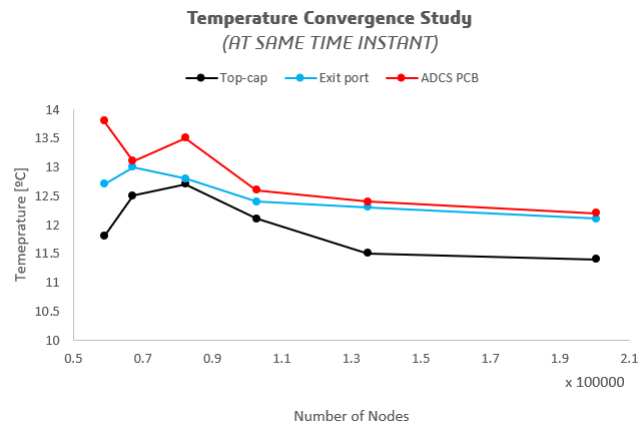

Figure B.2: Temperature convergence study fixing the number of calculations per orbit and varying the number of nodes

If different simulations are being performed but they share the same orbit and mesh, it is possible to reuse some of the results from one simulation to another by selecting the *restart* command on the solution definitions. The calculation of the view factors is the module that takes more time to be computed, however, if the *radiation simulation object*, *orbital heating*, *solar heating* and *radiative heating* remain the same, it is possible to reuse the view factor calculations done on a previous simulation. If at any chance the number of elements is changed, all the parameters should be calculated again.

The reader is advised to consult the *Siemens NX* documentation in [83].

B.2 Thermal Results with Thermal Control System

Table B.1: Thermal results with black anodized aluminum

	Cold Case		Hot Case		
	Min. [°C]	Max. [°C]	Min. [°C]	Max. [°C]	
+X solar cells	-24.334	5.314	-10.775	16.412	**OK**
-X solar cells	-27.986	17.265	-11.183	22.648	**OK**
+Y solar cells	-26.942	6.878	-10.578	25.472	**OK**
-Y solar cells	-27.614	5.811	-10.596	17.154	**OK**
-Z solar cells	-28.091	10.064	-11.062	18.169	**OK**
+X solar panel	-24.057	5.944	-10.410	17.258	**OK**
-X solar panel	-26.952	10.910	-9.858	20.675	**OK**
+Y solar panel	-26.692	7.405	-9.825	22.765	**OK**
-Y solar panel	-27.496	6.029	-10.474	17.445	**OK**
+Z solar panel	-24.511	7.800	-9.442	21.208	**OK**
-Z solar panel	-27.167	8.394	-10.035	18.651	**OK**
outer structure	-26.317	7.908	-9.138	20.088	**OK**
integrating sphere	-25.526	6.992	-7.705	19.172	**NOT OK**
inside structure (payload)	-25.858	7.361	-8.131	19.533	**OK**
inside structure (PCB)	-26.326	7.922	-9.004	20.128	**OK**
ADCS PCB	-25.703	8.180	-8.108	20.494	**OK**
OBC PCB	-19.312	6.523	0.187	20.332	**OK**
TT&C PCB	-18.977	5.060	0.581	19.296	**OK**
payload PCB	-20.259	5.362	-0.623	19.295	**OK**
EPS PCB	-26.179	7.810	-8.596	20.151	**OK**
PCB screws	-20.912	5.926	-1.541	19.827	**OK**
magnetorquers	-26.234	7.863	-8.511	20.096	**OK**
magnetorquer supports	-26.226	7.865	-8.539	20.098	**OK**
momentum wheel (bracket)	-26.304	7.919	-8.913	20.130	**NOT OK**
air core	-20.950	6.251	-1.833	20.027	**OK**
batteries	-26.355	7.917	-8.940	20.138	**NOT OK**
boards	-19.955	5.815	-0.399	19.713	**OK**

Table B.2: Thermal results with black solar panels

|	Cold Case		Hot Case		
	Min. [ºC]	Max. [ºC]	Min. [ºC]	Max. [ºC]	
+X solar cells	-21.181	11.215	-7.964	21.345	OK
-X solar cells	-25.147	25.025	-8.394	28.860	OK
+Y solar cells	-23.874	13.214	-7.763	33.095	OK
-Y solar cells	-24.756	11.815	-7.781	22.144	OK
-Z solar cells	-25.229	17.895	-8.247	24.755	OK
+X solar panel	-20.887	11.910	-7.576	22.264	OK
-X solar panel	-24.039	17.667	-6.985	26.455	OK
+Y solar panel	-23.696	13.662	-6.956	29.194	OK
-Y solar panel	-24.629	12.054	-7.650	22.465	OK
+Z solar panel	-21.048	14.232	-6.613	27.098	OK
-Z solar panel	-24.249	15.075	-7.164	24.600	OK
outer structure	-23.362	14.078	-6.218	25.344	OK
integrating sphere	-22.466	13.074	-4.676	24.365	OK
inside structure (payload)	-22.820	13.451	-5.134	24.750	OK
inside structure (PCB)	-23.377	14.091	-6.076	25.384	OK
ADCS PCB	-22.730	14.330	-5.142	25.749	OK
OBC PCB	-15.727	12.317	3.773	25.636	OK
TT&C PCB	-15.223	10.757	4.245	24.608	OK
payload PCB	-16.661	11.146	2.978	24.597	OK
EPS PCB	-23.214	13.962	-5.640	25.407	OK
PCB screws	-17.463	11.760	1.963	25.113	OK
magnetorquers	-23.270	14.025	-5.547	25.349	OK
magnetorquer supports	-23.264	14.028	-5.576	25.352	OK
momentum wheel (bracket)	-23.353	14.086	-5.979	25.386	OK
air core	-17.493	12.072	1.632	25.301	OK
batteries	-23.407	14.085	-6.008	25.393	NOT OK
boards	-16.334	11.599	3.198	25.012	OK

B.3 Thermal Cycles during 5 Orbits
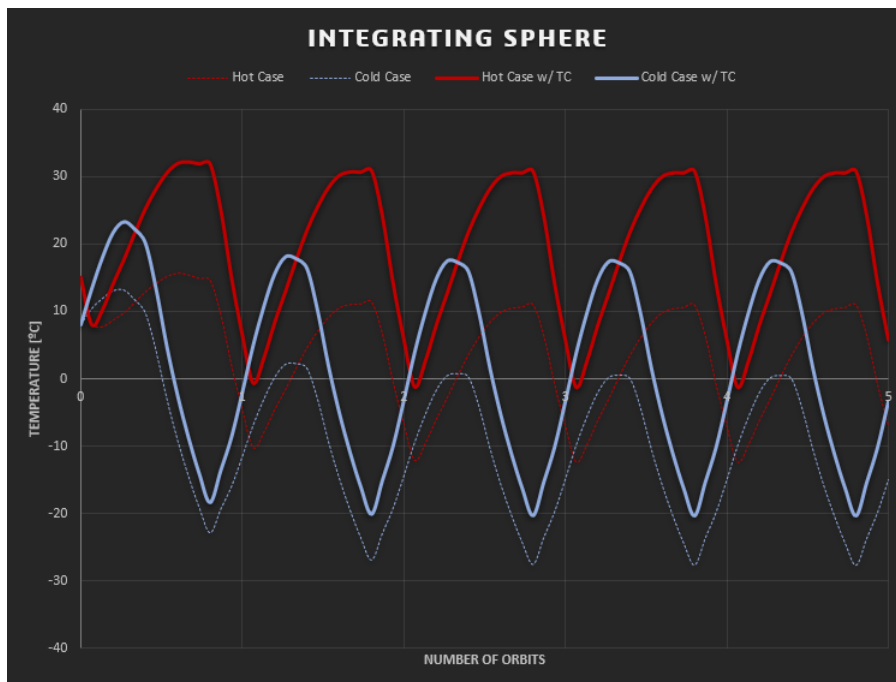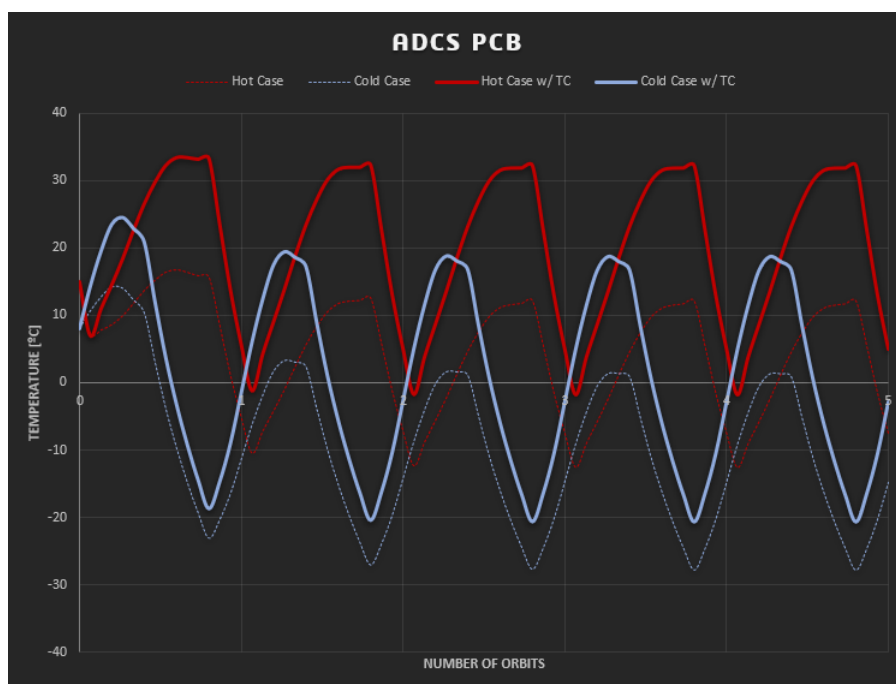

Figure B.3: Integrating Sphere thermal cycle
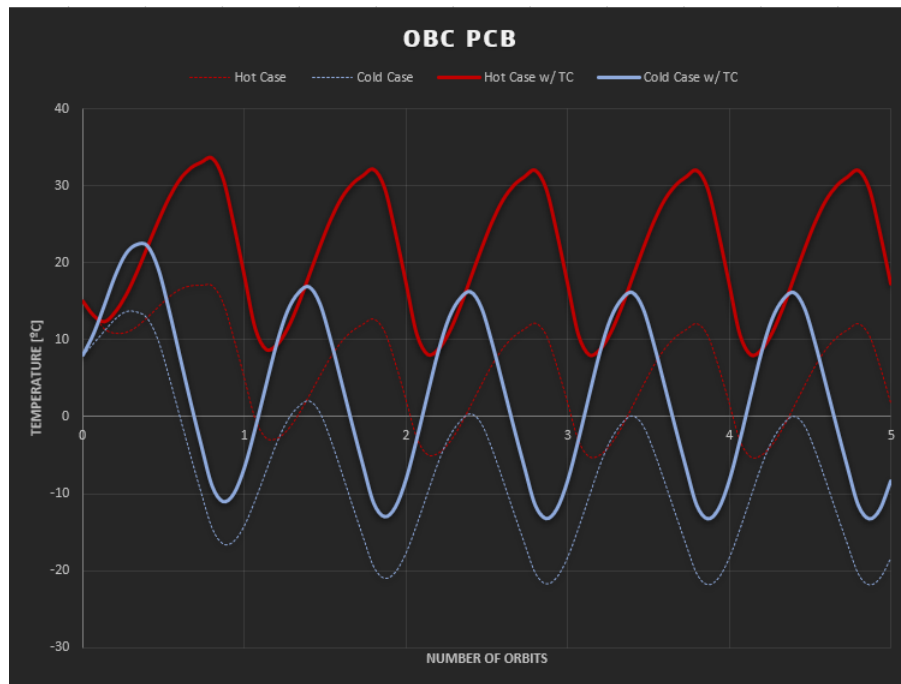

Figure B.4: ADCS PCB thermal cycle

100

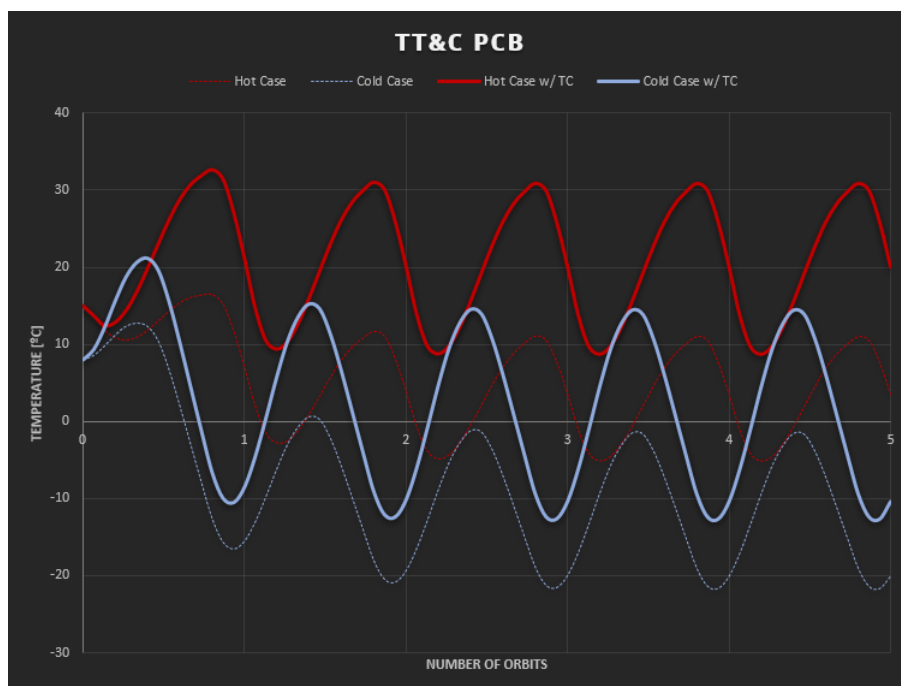Figure B.5: OBC PCB thermal cycle

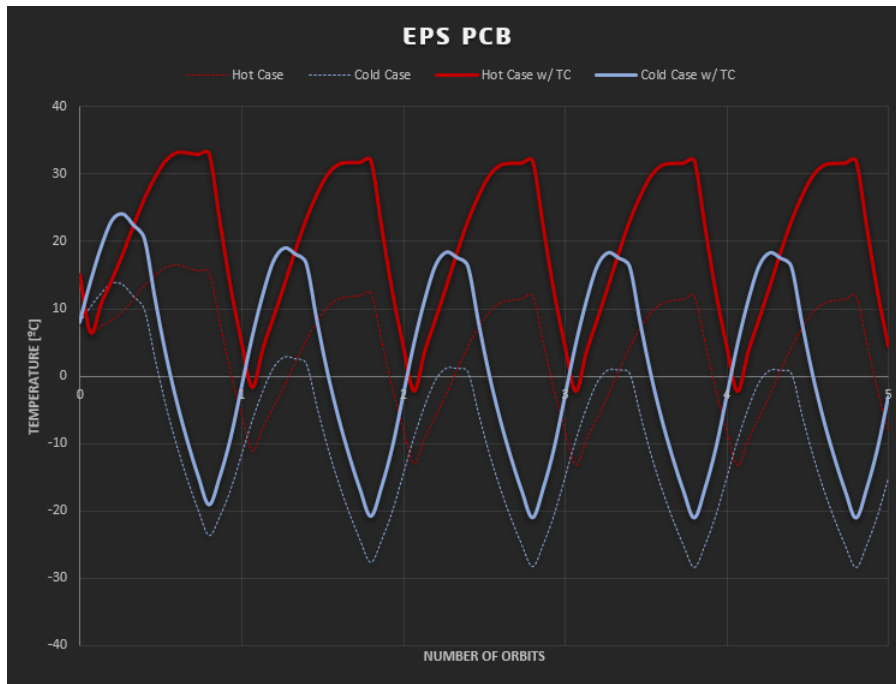Figure B.6: TT&C PCB thermal cycle
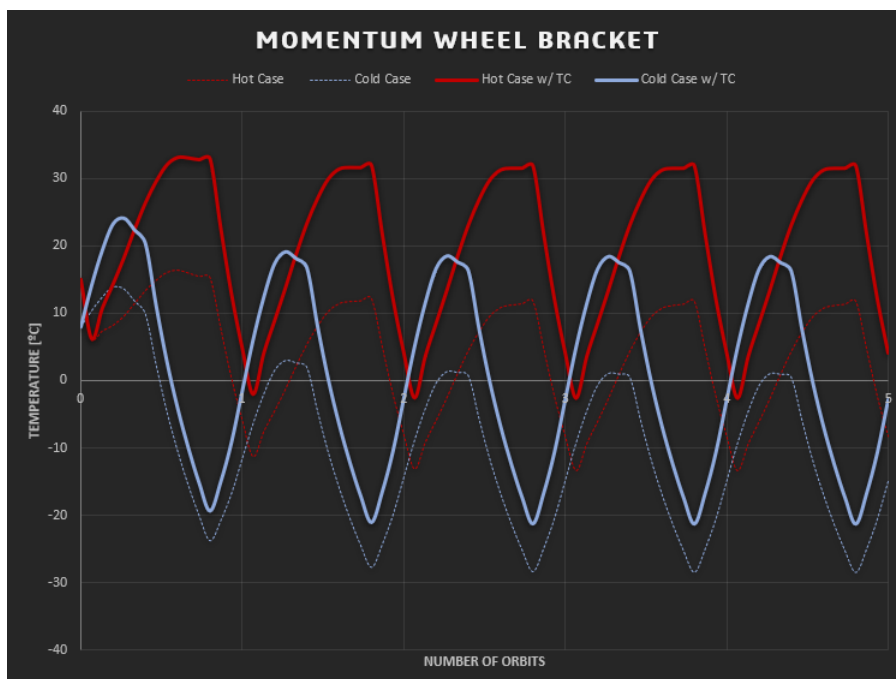
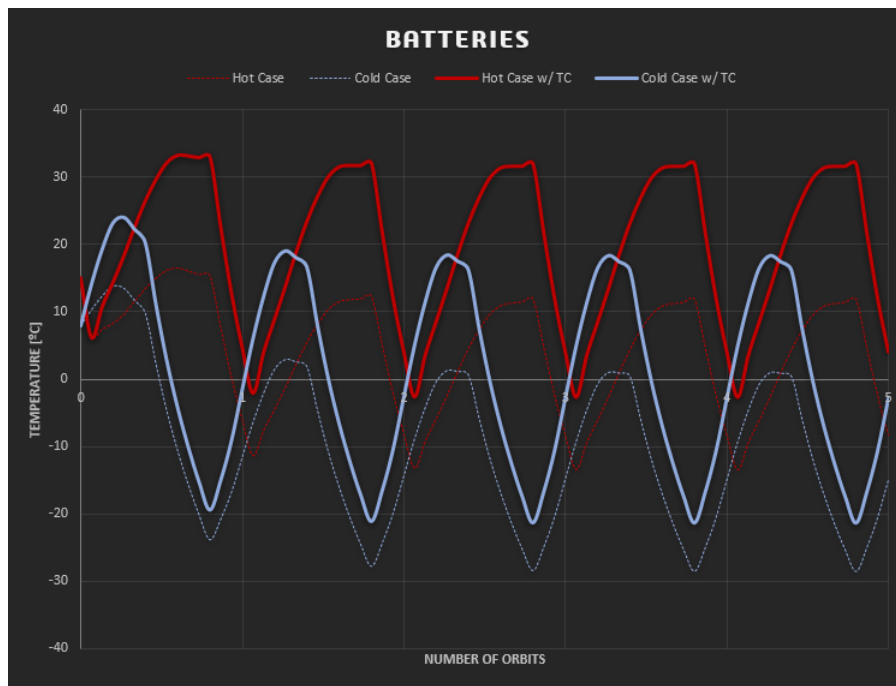Figure B.7: EPS PCB thermal cycle

Figure B.8: Momentum Wheel Bracket thermal cycle

Figure B.9: Batteries thermal cycle